A study of the Rayleigh-Taylor Instability during deceleration in inertial confinement fusion relevant conditions

Camille Clement Samulski

Dissertation submitted to the Faculty of the
Virginia Polytechnic Institute and State University
in partial fulfillment of the requirements for the degree of

Doctor of Philosophy
in
Aerospace Engineering

Bhuvana Srinivasan, Chair
Colin Adams
Stefano Brizzolara
Wayne Scales

April 24, 2024
Blacksburg, Virginia

Keywords: High Energy Density, Fusion, Plasma
Copyright 2024, Camille Clement Samulski

A study of the Rayleigh-Taylor Instability during deceleration in inertial confinement fusion relevant conditions

Camille Clement Samulski

(ABSTRACT)

The Rayleigh-Taylor instability (RTI) is one of the primary hydrodynamic instabilities that acts as a disputer to achieving high yield inertial confinement fusion (ICF). The potential for RTI to grow on the interior surface of ICF capsules, caused by deceleration during the implosion, further emphasises the need to better understand the seed mechanisms for RTI and possible mitigation methods for damping the instability growth. Reducing the growth of RTI during deceleration could preserve the spherical symmetry of ICF implosions and reduce the amount of mix between the solid capsule liner and fuel hot-spot. Additionally, it has been shown that magnetic fields do damp RTI growth, and the presence of a magnetic field lowers the threshold for achieving fusion and increases the yield.

Understanding the seed mechanisms of the RTI, especially on the interior surface of ICF capsules, further allows for better understanding of the morphology of the RTI growth during deceleration. Classically RTI has been studied using single or multi-mode sinusoidal perturbations, which result in bubble and spike morphology. However in addition to sinusoidal perturbations, single-feature perturbation, such as voids or divots, can seed RTI. This form of RTI is considered the thin-layer RTI, where the perturbation's wavelength is longer than the dense layer's thickness. This specific RTI evolution results in a morphology consisting of a single central spike and arms that extend horizontally away from the spike and eventually fall back towards the interface. Thin-layer RTI is important to explore during deceleration due to the presence of the fill-tubes in ICF capsules causing holes in the shell.

Creating experimental platforms for current laser configurations on Omega and the National Ignition Facility (NIF) is necessary to study deceleration-stage RTI experimentally and validate computational modeling. A comprehensive exploration of potential experimental designs on Omega, Omega-EP, and NIF are explored to identify a platform with which deceleration-stage RTI can be studied with and without the presence of an externally applied magnetic field. Additionally, the design of a novel experimental platform for Omega-EP to study thin-layer RTI during deceleration with and without an externally applied magnetic field is presented, along with data collected during the first experiments performed utilizing the platform. Lastly, a first of it's kind RTI platform for NIF is fielded and the results are presented, including an exploration of the possible impacts high-intensity-laser generated hot-electrons can have on experimental targets. The results of these experimental platforms are used to benchmark computational models, and demonstrate the potential for magnetized RTI to be studied comprehensively in future experiments.

A study of the Rayleigh-Taylor Instability during deceleration in inertial confinement fusion relevant conditions

Camille Clement Samulski

(GENERAL AUDIENCE ABSTRACT)

The potential of controlled sustained nuclear fusions as a viable energy source has rapidly become a reality in recent years. Monumental progress has been made in the pursuit of controlled fusion, including the repeated achievement of fusion ignition at the National Ignition Facility (NIF), meaning there was successful production of more energy from the fusion reaction than laser energy used to trigger the reaction. However, in order for fusion to become a truly viable energy source improvements in capsule design and the mitigation of disruptions, like hydrodynamic instabilities, must be explored to produce higher energy yields.

The Rayleigh-Taylor instability (RTI) is one of the most detrimental hydrodynamic instabilities in inertial confinement fusion (ICF). RTI occurs when a lighter fluid, like the fuel used in fusion reactions, supports a heavier fluid, the ICF capsule itself, under the influence of gravity. An ICF capsule is imploded, induced by the driving mechanism, such as a laser, but once the driver stops the capsule will begin to decelerate. During this deceleration stage, the interior surface of the ICF capsule in susceptible to RTI growth causing the cold capsule material to mix with the hot fusion fuel. This mixing reduces the fuel's ability to reach the necessary temperatures and densities need to achieve ignition and produce high energy yields. As a result, it is crucial to better understand the defects that cause RTI to grow and explore methods that could damp the RTI growth and preserve the integrity of the implosion and fusion fuel.

The work presented here focuses on exploring both the seed mechanisms for RTI and mitigation strategies. Specifically, using an externally applied magnetic field has been shown to damp RTI growth and in know to lower the threshold of the conditions needed to achieve ignition. A study of possible experimental setups at both the Omega laser and NIF is explored in order to identify a design with which the damping effects of an externally applied magnetic field on deceleration-stage RTI can be studied experimentally. From this design study platforms for the Omega-EP and NIF were conceptualized and ultimately fielded. The results from these novel experiments are presented, along with an exploration of possible effects on RTI unexpected preheating of the experimental targets. Additionally, an exploration of the seed mechanisms of RTI is presented with a look at the classic sinusoidal perturbation as well as using a divot to seeded thin-layer RTI, which evolves with a spike and arm morphology rather than the classical bubble and spike. The experimental results from Omega-EP using a divot as the perturbation are presented. Novel results of varying RTI platforms and their potential for further development provide crucial insight into the

possible presence of deceleration-stage RTI in ICF capsules and can be iterated on in the future to further explore RTI evolution and damping methods.

Dedication

To my husband Haiwen

Acknowledgments

First and foremost I would like to thank my PhD advisor Professor Bhuvana Srinivasan for her support throughout my graduate school career. With her guidance and wisdom I was able to pursue my own ideas and gain experience in areas I could only dream of. I would also like to thank Dr. Mario Manuel at General Atomics for his guidance in all things experimental and his continued support of my ideas. Without either Professor Srinivasan or Dr. Manuel I would not have been able to explore my interest in both the computational and experimental design sides of High Energy Density Physics. I also thank my committee members, Professor Colin Adams, Professor Stefano Brizzolara and Professor Wayne Scale for their time and feedback.

I would also like to thank the following collaborators: Dr. John Kline and Dr. Josh Sauppe at Los Alamos National Laboratory for their valuable feedback and guidance, Dr. Kumar Raman at Lawrence Livermore National Laboratory for his support with using Ares and always having time to answer my questions, and Dr. Philip Nilson and the Laboratory for Laser Energetics for his help understanding and using Fresnel Zone Plate on Omega-EP. I would also like the thank my fellow lab mates, especially Asher Beck and Matthew Carrier for their feedback on this dissertation, and the many others who have given me feedback and I bounced ideas off of during my time as a graduate student. I would also like to thank my family, my parents for their continuous support throughout my education, my aunts and uncles for their constant support and excitement for my research and successes. Lastly, I would like to thank my husband Haiwen, for his unwavering support, his devotion, and his willingness to move across the country for me. To him I owe the most gratitude.

This work is supported by Los Alamos National Laboratory under subcontract 463281 and US Department of Energy under Award No. DE-SC0020055 and US Department of Energy DE-SC0022319 by the Financial Assistance Program. I would like to also acknowledge Advanced Research Computing at Virginia Tech for providing computational resources and technical support, and the FLASH Center for Computational Science for there constant feedback and access to the FLASH code developed by the DOE NNSA-ASC OASCR Flash Center at the University of Rochester.

This document has been provided release under the identifier LA-UR-24-24023.

Contents

1 Introduction **1**

1.1 Rayleigh-Taylor Instability 4

1.2 Magnetohydrodynamics 7

1.3 Structure and Content 8

1.4 Attributions 9

Bibliography **11**

2 Deceleration-stage Rayleigh Taylor Growth in a Background Magnetic Field Studied in Cylindrical and Cartesian Geometries **15**

2.1 Introduction 16

2.2 Numerical Model 17

2.3 Cylindrical Configurations 18

2.3.1 Cylindrical Model Tuning 18

2.3.2 Cylindrical RT on Omega 19

2.3.3 Cylindrical RT on NIF 21

2.4 Planar Configurations 21

2.4.1 Planar RT on Omega 21

2.4.2 Planar RT on NIF 22

2.5 Conclusions 24

2.6 Bibliography 26

3 A Magnetized Experimental and Computational Study of Thin-Layer Rayleigh-Taylor Instability Development During Deceleration **28**

3.1 Experimental Design Process 29

3.2 An Experimental and Computational Study of Thin-Layer Rayleigh-Taylor Instability Development During Deceleration with and without an Externally Applied Magnetic Field . . . 34

3.2.1 Introduction . . . 35

3.2.2 Experimental Setup and Design . . . 36

3.2.3 Manufacturing Defects . . . 38

3.2.3.1 The Effect of a Vacuum Gap . . . 38

3.2.3.2 The Effect of a Tilt . . . 38

3.2.4 Experimental Results . . . 40

3.2.5 Predicted 3D Computational Results . . . 41

3.2.6 Conclusions . . . 42

3.2.7 Bibliography . . . 43

Bibliography **46**

4 Preheat effects in laser-driven shock-tube experiments at intensities greater than 10^{15} W/cm^2 at Omega-EP and the NIF **48**

4.1 Introduction . . . 49

4.2 Experimental Design and Results on NIF . . . 50

4.2.1 Experimental Design . . . 50

4.2.2 Results . . . 50

4.3 Experimental Design and Results at Omega-EP . . . 51

4.3.1 Experimental Design . . . 51

4.3.2 Results . . . 51

4.4 Estimated Preheat Effects on Targets at Omega-EP and NIF . . . 52

4.4.1 Preheat effects on Omega-EP . . . 52

4.4.2 Estimated preheat effects on NIF . . . 53

4.5 Conclusions . . . 55

4.6 Bibliography . . . 56

5 Conclusions and Future Work **58**

Bibliography **63**

Appendices **65**

Appendix A Synthetic x-ray radiograph generator for FLASH **66**

Chapter 1

Introduction

Controlled sustained nuclear fusion as the penultimate sustainable source of renewable energy has been pursued for almost a century. Recent advancements in both laser and magnetic driven fusion efforts have brought about the precipice of achievable nuclear fusion and made it a viable avenue for future generations energy needs [1, 2, 3, 4]. The root of successful nuclear fusion lies in combining two lighter nuclei into a single heavier nucleus releasing significant energy energy from the reaction due to the conservation of mass. In comparison, nuclear fission, used in current nuclear reactors, derives energy from the splitting of a heavier atom, like uranium-235, via radioactive decay. While a nuclear fission reaction produces large quantities of energy, $\sim$200 MeV, in comparison to the $\sim$17 MeV produced by a deuterium-tritium fusion reaction, the quantity of fissile material necessary for fission is significantly greater than that needed for fusion reactions. Thus, the amount of energy available per mass of fusion fuel is significantly greater than that of fissile material, not to mention the significantly increased risks of radioactive waste that come with fission reactions.

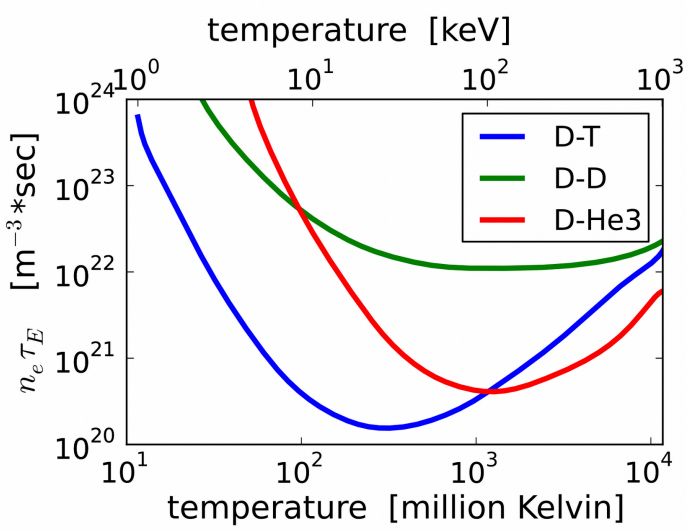

Figure 1.1: A demonstration of the Lawson criterion for reactions using deuterium-tritium (D-T), deuterium-deuterium (D-D), and deuterium ^{3}He (D-^{3}He). The x-axis represents the required temperature in either million Kelvin or kilo-electron volts (keV), while the y-axis represents the required density and confinement time. [5]

As a result of the attractiveness of nuclear fusion as an energy source, multiple avenues to achieve sustainable controlled nuclear fusion are being explored. The work presented here deals with inertial confinement fusion (ICF) as the primary method of achieving fusion, which has recently seen demonstrably improved gains in moving towards achieving sustained controlled fusion on the National Ignition Facility (NIF). Successful ICF reactions depend on pushing fusion fuel to exceptionally high energy density (HED) states for very short time-scales as per the Lawson criteria [6]. Figure 1.1 shows how the necessary conditions, temperature, density, n_e, and confinement time, τ_E, to achieve ignition, per the Lawson criteria, vary based on the fuel source, deuterium-tritium (D-T), deuterium-deuterium (D-D) or deuterium-^{3}He. Pushing the fuel to these HED state ensures that there will be high enough number density and the nuclei will be at high enough temperatures to have enough kinetic energy to overcome the Coulomb barrier and fuse. ICF aims to achieve these necessary fusion conditions by driving or imploding a pusher at exceptionally high velocities, allowing the inertia to compress the fusion fuel and increase its number density and temperature to a regime that is required to achieve a nuclear fusion reaction. In addition to the difficult task of reaching the necessary conditions for fusion, the ability to control and sustain such a reaction is required for ICF to produce a viable future energy source.

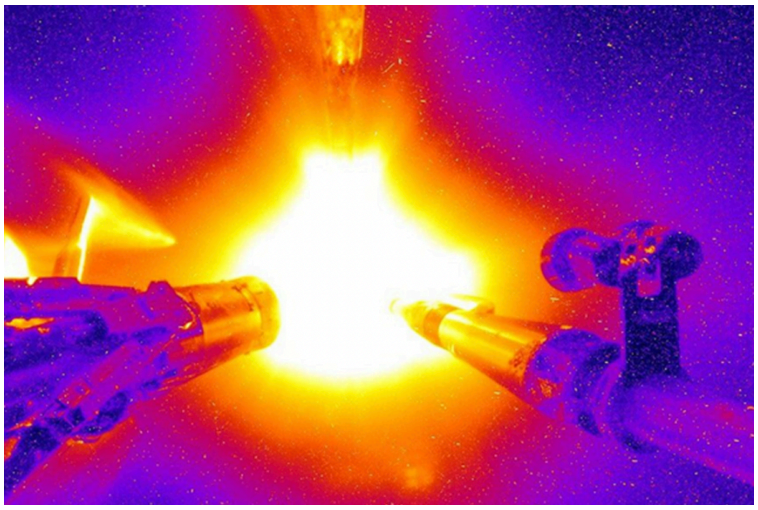

Figure 1.2: A colorized image form (LLNL link) of a 2016 "Big-Foot" D-T experiment on NIF using a diamond target capsule for the fuel demonstrating the HED conditions necessary for ICF.

Within ICF there are many different avenues through which controlled and sustained nuclear fusion is being pursued. These include magnetized liner inertial fusion (MagLIF) as performed on the Z-machine at Sandia National Laboratory, indirect-drive ICF, and direct-drive ICF as performed on the NIF at Lawrence Livermore National Laboratory (LLNL). The interior chamber of the NIF, where direct-drive and indirect-drive experiments occur, can be seen in figure 1.2. The primary method explored in this work is direct-drive ICF,

in which a spherical target is filled with fuel, commonly deuterium and tritium, and a large scale laser is incident directly on the surface of the target in a uniform manner to spherically implode the target and compress the fuel inside to the desired density and temperature, illustrated in figure 1.3.

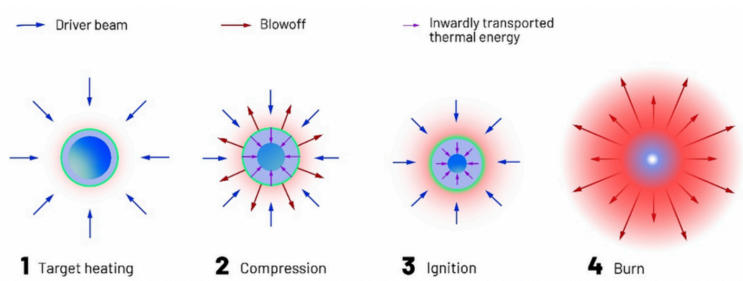

Figure 1.3: A recreation of the process and stage of direct-drive ICF from Ditmire et. al. [2023], showing the laser drive incident on the capsule, the compression of the capsule, ignition and final burn of the fuel to create more energy [7].

Current ICF platforms, like direct-drive ICF, do not have the precision control over targets and lasers necessary to successfully reach high areal densities, ρR, and ignite the capsule. High fuel areal density is needed for high gain or yield, which is determined by the ratio of energy out to energy in and the burn fraction, $\Phi = \frac{\rho R}{\rho R + H_b}$ [8, 9]. As can be seen in the equation for the burn fraction, the need for high areal density conditions is necessary for ICF platforms to be considered viable as energy sources. The presence of hydrodynamic instabilities limits the ability for ICF targets to achieve high compression, as can be seen in figure 1.4, showing plots of fuel compression verses yield and simulations showing the deterioration of the spherical implosion due to instability growth [10, 11]. Thus, a large point of interest and improved performance is evolving target designs in order to mitigate instabilities that disrupt the hot spot.

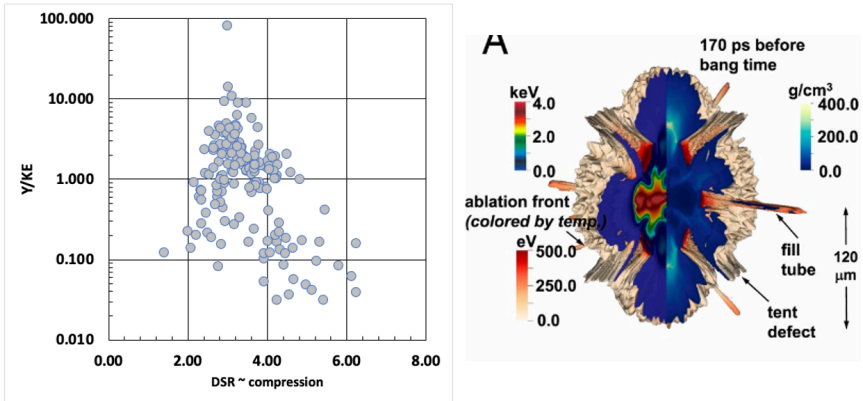

Figure 1.4: Recreations of figure from O.A. Hurricane et. al. [2023], left, and Clark. et al. [2016] , right, showing the relationship between compression and yield in fusion reactions and the disruption of compression from instability growth [10, 11].

The instabilities that occur on the interior of the target where the shell and the fuel meet are highly detrimental by causing the cold shell material to mix with the hot fuel. Mixing results in the reduction of the temperature and reduces the amount of fuel material available for a fusion reaction, while also causing asymmetric implosions to occur [10, 12, 13, 14, 15, 16]. Mitigating the mixing, which can be caused by capsule design flaws, is necessary for the direct-drive platform, and other ICF platforms, to successfully progress towards viable energy platforms.

1.1 Rayleigh-Taylor Instability

The Rayleigh-Taylor instability (RTI) has been identified as one of the primary disruptors of ICF efforts to reaching high-energy gain [17, 18]. RTI develops when there is an interface between a high density fluid and low density fluid, such as when water supported by oil in a glass [19, 20]. In the example of oil and water, the system is not in equilibrium and the force of gravity causes the lighter oil to rise up into the water and displace the water below it until the system has reached the stable equilibrium of the oil being on top and water on the bottom. This same phenomena occurs in fluid systems where an interface between a lighter fluid (ρ_1) and higher density fluid (ρ_2) is acted upon by a constant acceleration (g) parallel to the density gradient. An example of the evolution of the RTI spike and bubble growth and subsequent material mixing can be seen in figure 1.5.

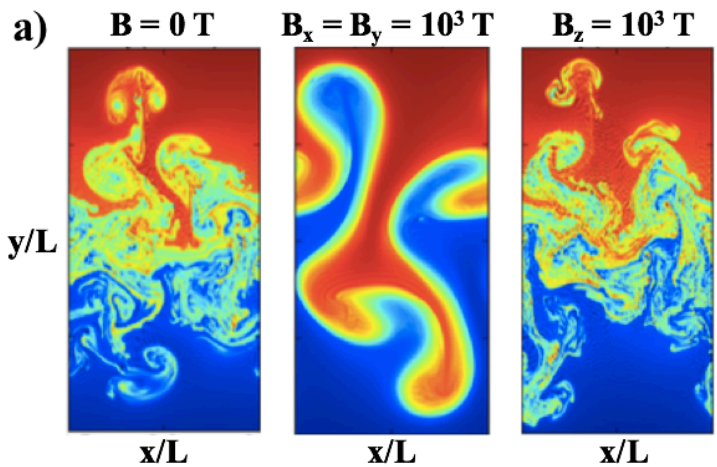

Figure 1.5: A recreation of a plot from Srinivasan and Tang [21] demonstrating the effects of a 10 T seed magnetic field and it's orientation on RTI.

Classical RTI is governed by a the growth rate equation,

$$\gamma^2 = gkA_t \tag{1.1}$$

where k is the wave number of the perturbation at the interface between fluid layers is $k = 2\pi/\lambda$ and λ is the wavelength. A_t is the Atwood number, defined as $A_t = (\rho_2 - \rho_1)/(\rho_2 + \rho_1)$ [22]. As the fluid layer's densities approach each other ($\rho_1 = \rho_2$) the Atwood number approaches zero and the growth of RTI is reduced. The growth of RTI is further impacted by the presence of a magnetic field (B). In such a case the growth rate equation becomes,

$$\gamma_B^2 = gkA_t - \frac{2B^2k^2cos^2\theta}{\mu_0(\rho_2 + \rho_1)} \tag{1.2}$$

where θ is the angle between the magnetic field and the wave vector $\mathbf{k}$. This dependence on the magnetic field is most immediately notable by the complete damping of perturbations with wavelengths equal to or less than the critical wavelength, (λ_c). The critical wavelength of the system is found with the following equation.

$$\lambda_c = \frac{4\pi B^2cos^2\theta}{\mu_0 g(\rho_2 - \rho_1)}. \tag{1.3}$$

The presence of RTI on the interior surface of ICF capsules occurs due to the sharp density difference between the low density fuel and the solid density shell, which is then accelerated inwards due to the implosion, consequently causing the interior surface to be RTI unstable. The implosion of the ICF capsule causes significant pressure to build within the hot spot,

thus the implosion will begin to decelerate causing deceleration-stage RTI growth on the interior surface of the ICF capsule. In this deceleration stage the lighter fluid displaces the high density shell material causing the comparatively cold and dense material from the shell to mix into the hot-spot, where ignition and burn are intended to occur, and disrupt the system's ability to reach the necessary temperatures, pressures and densities for fusion. The perturbations that seed the RTI on the interior of ICF capsules can range from manufactured sinusoidal modes producing classical RTI growth, to voids, divots, manufacturing imperfections, and the fill-tube hole used to inject the fusion fuel into the interior of capsules. The latter perturbations are single-feature perturbations that seed thin-layer RTI growth.

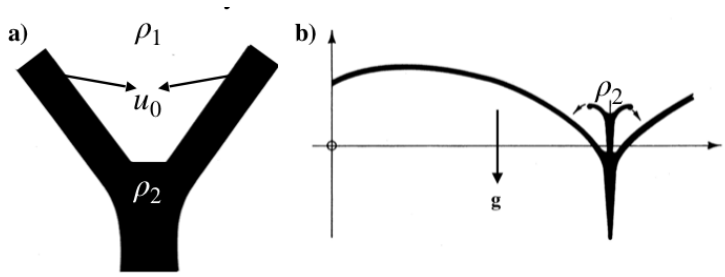

Figure 1.6: A recreation of a plot from Ott [23] replicating the difference in thin-layer RTI evolution, with the perturbation collapsing inwards and resulting in a spike or jet like feature with arms extending to the side.

Thin-layer RTI is a specific configuration that involves perturbations with wavelengths longer than the thickness of the dense layer. Consequently, it can be applied to a single-feature perturbation with the assumption that the perturbation would repeat if the capsule was large enough, and the wavelength would be significantly longer than the thickness of the ICF capsule shell. The evolution of thin-layer RTI occurs when the walls of the perturbation collapse inwards and causes a jet of high density material to grow, creating and RTI spike and arms. The arms extend to the sides and then fall back towards the interface propagating inwards. A schematic of this can be seen in figure 1.6, showing the jet and subsequent RT spike evolving from the single-feature perturbation. Due to the nature of this form of RTI's evolution, the growth becomes nonlinearity earlier in time, thus due to equation 1.2, a magnetic field could have a impact on the RTI earlier in time.

The presence of a magnetic field in an ICF implosion could have a number of effects on the system. Firstly, potential self-generated magnetic fields [21, 24, 25] and externally applied magnetic fields can be amplified due to the magnetic flux compression during the implosion. It has been theorized that the presence of a magnetic field reduces the amplitude of RTI spike and bubble growth [21, 24, 25] which would reduce the subsequent mixing between the fuel and the shell and maintain the integrity of the hot-spot. Additionally, it has been shown that the presence of a magnetic field lowers the criteria for ignition and increases the fusion yield [26, 27]. Thus, using a magnetic field to damp the RTI growth seeded by classical

sinusoidal perturbations or single-feature perturbations also could increase the chances of reaching high-yield fusion. The complexity of RTI and other hydrodynamic instabilities and their negative impact on ICF systems requires high fidelity modeling in order to design viable ICF platforms, so utilizing the appropriate equations and improving existing models to better replicate experimental conditions and data is crucial for such ICF design work.

1.2 Magnetohydrodynamics

Magnetohydrodynamics (MHD) as a model of describing electrically conducting fluids was first discussed by Hannes Alfven in the 1940s [28]. The MHD model has been long utilized in plasma physics to build accurate computational models for plasma interactions. The MHD equations can be extended to include a number of diffusive effects, specifically resistive-MHD, which will be the primary form of the MHD equations used in the work presented. Including resistivity in the MHD equations ensures higher fidelity modeling of systems like the magneto-Rayleigh-Taylor instability (MRT) for comparison for regimes where the effects of resistivity are not negligible.

The MHD equations are broken up into conservation of mass, momentum and energy, as well as an induction equation. The Ares [29] code solves these equations in conservative form as,

$$\frac{\partial \rho}{\partial t} + \nabla \cdot [\rho \mathbf{u}] = 0 \tag{1.4}$$

for conservation of mass,

$$\frac{\partial \rho \mathbf{u}}{\partial t} + \nabla \cdot \left[\rho \mathbf{u}\mathbf{u} + P\mathbb{I} - \frac{\mathbf{B}\mathbf{B}}{\mu_0} + \frac{|\mathbf{B}|^2}{2\mu_0}\mathbb{I} \right] = 0 \tag{1.5}$$

for conservation of momentum,

$$\frac{\partial \epsilon}{\partial t} + \nabla \cdot \left[\left(\epsilon + P + \frac{|\mathbf{B}|^2}{2\mu_0} \right) \mathbf{u} - \frac{\mathbf{B} \cdot \mathbf{u}}{\mu_0} \mathbf{B} \right] = S_\epsilon \tag{1.6}$$

for conservation of energy, and

$$\frac{\partial \mathbf{B}}{\partial t} = \nabla \times \mathbf{E} \tag{1.7}$$

as the induction equation [30]. In these equations $\mathbf{u}$ corresponds to the velocity vector, $\mathbf{B}$ to the magnetic field vector, ρ is the mass density, P is the total pressure, ϵ the total energy, and μ_0 the magnetic permeability of free space. S_ϵ is a source term, such as ohmic

heating, for equation 1.6 and $\mathbf{E}$ is the electric field in equation 1.7. The electric field used in resistive-MHD calculations is given as,

$$\mathbf{E} = -\mathbf{u} \times \mathbf{B} + \eta \mathbf{j}, \tag{1.8}$$

where $\mathbf{j}$ is the current density, and η is electrical resistivity. The MHD equations as presented are not closed, and required the use of an equation of state (EOS) to provide a pressure relation to density and temperature [31, 32]. The relation can be supplied by ideal gas EOS [33], however when studying HED and ICF such an EOS is not sufficient in capturing the range of material states, so EOS is supplied in a tabulated form for specific materials. These tabulated EOS can also supply transport coefficients, specifically the electrical resistivity for resistive-MHD [34] and thermal conductivity for thermal diffusion inclusion. The Ares code's MHD capabilities are primarily presented in the results found in chapters 3 and 4.

In chapter 2 the primary code used is the FLASH code from the University of Rochester [35, 36]. FLASH is a radiation hydrodynamic code with adaptive mesh refinement (AMR) capabilities. The FLASH code solves the Euler equations for unmagnetized HD simulations that are presented in chapter 2 and MHD equations for the resistive-MHD simulations. An in-depth discussion of the specific equations being solved can be found in chapter 2. Differences between the two codes are the high-fidelity tabulated EOS available with Ares and the implicit implementation of resistive-MHD which was not available at the time in FLASH, and the advanced AMR capabilities in FLASH which were not available in 3D at the time using Ares.

1.3 Structure and Content

This dissertation primarily follows the *Manuscript* format, with the following three chapters consisting of peer-reviewed journal publications. The content of these articles is summarized as:

Chapter 1: Provides a background exploration of ICF, specifically on direct-drive laser driven ICF. The limitations in ICF due to hydrodynamic instabilities is discussed, with an in-depth explanation of the RTI classically and in the thin-layer configuration. The MHD equations used to explore HED and RTI computationally are reviewed.

Chapter 2: Consists of a peer-reviewed paper titled *"Deceleration-stage Rayleigh Taylor Growth in a Background Magnetic Field Studied in Cylindrical and Cartesian Geometries"* [22] published in the special edition of Matter and Radiation at Extremes. This publication presents a computational study of experimental platforms on which deceleration-stage RTI could be feasibly studied in the presence of background mag-

netic fields. The limitations of current experimental platforms are explored along with the presentation of a viable design platform for the NIF.

Chapter 3: Consists of a in-detail introduction on the design process for experimental targets built to study thin-layer RTI, along with initial experimental data from Omega-EP, followed by the peer-reviewed paper titled *"A Magnetized Experimental and Computational Study of Thin-Layer Rayleigh-Taylor Instability Development During Deceleration"* in a completed state and to be submitted. The results from a deceleration-stage thin-layer RTI experimental platform on Omega-EP are presented, along with computational validation of Ares simulations using experimental data. The necessity of 3D simulations for high-fidelity target design work is also discussed.

Chapter 4: Presents a peer-reviewed paper titled *"An Study of High Intensity Laser Drive Generated Hot-Electron Induced Preheating of Experimental Targets at Omega-EP and NIF"* in a completed state and in preparation for submission. This manuscript discusses the presence of high-intensity laser generated hot-electron populations during experiments and their potential preheating effects on targets. Data from Omega-EP experiments, as well as NIF experiments, are presented, along with a computational study of varying preheat levels effects on the experimental target design.

Chapter 5: Concludes the work by reviewing the major findings in the aforementioned publications and discusses possible directions for future work.

1.4 Attributions

The work presented in this dissertation consist of three peer-reviewed journal papers, of which Camille Samulski is the primary contributor and first author. The collaborators listed as co-authors contributed as follows:

- *Dr. Bhuvana Srinivasan* is my Ph.D. advisor. She provided invaluable guidance and project-planning support during my Ph.D. work. She also reviewed and edited the papers presented.
- *Dr. Mario Manuel* is a collaborator from General Atomics. He provided experimental guidance and support in addition to reviewing and editing all writing.
- *Dr. John Kline* is a collaborator at Los Alamos National Laboratory. He provided edits and feedback on all manuscripts.
- *Dr. Josh Sauppe* is a collaborator at Los Alamos National Laboratory. He provided experimental data and feed back on manuscripts.

- *Dr. Kumar Raman* is a collaborator at Lawrence Livermore National Laboratory. He aided with the setup of Ares simulations and relevant support, in addition to guidance for simulation planing and interpretation. He reviewed and edited the relevant publication.
- *Dr. Philip Nilson* is a collaborator from the Laboratory for Laser Energetics at the University of Rochester. He provided support with using Fresnel Zone Plates as diagnostics at Omega-EP and reviewed the relevant publication.

Bibliography

[1] A. L. Kritcher, et. al., Design of an inertial fusion experiment exceeding the lawson criterion for ignition, Phys. Rev. E 106 (2022) 025201. URL: https://link.aps.org/doi/10.1103/PhysRevE.106.025201. doi:10.1103/PhysRevE.106.025201.

[2] A. B. Zylstra, et. al., Experimental achievement and signatures of ignition at the National Ignition Facility, Physical Review. E 106 (2022). URL: https://www.osti.gov/biblio/1959535. doi:10.1103/physreve.106.025202.

[3] H. Abu-Shawareb, et. al. (Indirect Drive ICF Collaboration), Lawson criterion for ignition exceeded in an inertial fusion experiment, Phys. Rev. Lett. 129 (2022) 075001. URL: https://link.aps.org/doi/10.1103/PhysRevLett.129.075001. doi:10.1103/PhysRevLett.129.075001.

[4] S. A. Slutz, R. A. Vesey, High-gain magnetized inertial fusion, Phys. Rev. Lett. 108 (2012) 025003. URL: https://link.aps.org/doi/10.1103/PhysRevLett.108.025003. doi:10.1103/PhysRevLett.108.025003.

[5] Leray, S., Nuclear energy basics, EPJ Web Conf. 268 (2022) 00008. URL: https://doi.org/10.1051/epjconf/202226800008. doi:10.1051/epjconf/202226800008.

[6] J. D. Lawson, Some criteria for a power producing thermonuclear reactor, Proceedings of the Physical Society. Section B 70 (1957) 6. URL: https://dx.doi.org/10.1088/0370-1301/70/1/303. doi:10.1088/0370-1301/70/1/303.

[7] T. Ditmire, M. Roth, P. Patel, D. Callahan, G. Cheriaux, P. Gibbon, D. Hammond, A. Hannasch, L. Jarrott, G. Schaumann, W. Theobald, C. Therrot, O. Turianska, X. Vaisseau, F. Wasser geb. Wagner, . Zähter, M. Zimmer, W. Goldstein, Focused energy, a new approach towards inertial fusion energy, Journal of Fusion Energy 42 (2023). doi:10.1007/s10894-023-00363-x.

[8] S. Atzeni, J. Meyer-ter Vehn, The Physics of inertial fusion, 2004. doi:10.1093/acprof:oso/9780198562641.001.0001.

[9] G. S. Fraley, E. J. Linnebur, R. J. Mason, R. L. Morse, Thermonuclear burn characteristics of compressed deuterium-tritium microspheres, The Physics of Fluids 17 (1974) 474–489. URL: https://doi.org/10.1063/1.1694739. doi:10.1063/1.1694739. arXiv:https://pubs.aip.org/aip/pfl/article-pdf/17/2/474/12785108/474_1_online.pdf.

[10] D. S. Clark, C. R. Weber, J. L. Milovich, J. D. Salmonson, A. L. Kritcher, S. W. Haan, B. A. Hammel, D. E. Hinkel, O. A. Hurricane, O. S. Jones, M. M. Marinak, P. K. Patel, H. F. Robey, S. M. Sepke, M. J. Edwards, Three-dimensional simulations of low foot and

high foot implosion experiments on the National Ignition Facility, Physics of Plasmas 23 (2016). URL: https://www.osti.gov/biblio/1438663. doi:10.1063/1.4943527.

[11] O. A. Hurricane, P. K. Patel, R. Betti, D. H. Froula, S. P. Regan, S. A. Slutz, M. R. Gomez, M. A. Sweeney, Physics principles of inertial confinement fusion and u.s. program overview, Rev. Mod. Phys. 95 (2023) 025005. URL: https://link.aps.org/doi/10.1103/RevModPhys.95.025005. doi:10.1103/RevModPhys.95.025005.

[12] D. Clark, et al., Radiation hydrodynamics modeling of the highest compression inertial confinement fusion ignition experiment from the Nation Ignition Campaign., Physics of Plasmas 22 (2015) 022703.

[13] C. Weber, et al., Mixing in ICF implosions on the Nation Ignition Facility caused by the fill-tube, Physics of Plasmas 27 (2020) 032703.

[14] D. S. Clark, C. R. Weber, J. L. Milovich, A. E. Pak, D. T. Casey, B. A. Hammel, D. D. Ho, O. S. Jones, J. M. Koning, A. L. Kritcher, M. M. Marinak, L. P. Masse, D. H. Munro, M. V. Patel, P. K. Patel, H. F. Robey, C. R. Schroeder, S. M. Sepke, M. J. Edwards, Three-dimensional modeling and hydrodynamic scaling of National Ignition Facility implosions, Physics of Plasmas 26 (2019) 050601. doi:10.1063/1.5091449.

[15] B. M. Haines, C. H. Aldrich, J. M. Campbell, R. M. Rauenzahn, C. A. Wingate, High-resolution modeling of indirectly driven high-convergence layered inertial confinement fusion capsule implosions, Physics of Plasmas 24 (2017) 052701. doi:10.1063/1.4981222.

[16] J. P. Sauppe, B. M. Haines, S. Palaniyappan, P. A. Bradley, S. H. Batha, E. N. Loomis, J. L. Kline, Modeling of direct-drive cylindrical implosion experiments with an Eulerian radiation-hydrodynamics code, Physics of Plasmas 26 (2019) 042701. doi:10.1063/1.5083851.

[17] R. S. Craxton, K. S. Anderson, T. R. Boehly, V. N. Goncharov, D. R. Harding, J. P. Knauer, R. L. McCrory, P. W. McKenty, D. D. Meyerhofer, J. F. Myatt, A. J. Schmitt, J. D. Sethian, R. W. Short, S. Skupsky, W. Theobald, W. L. Kruer, K. Tanaka, R. Betti, T. J. B. Collins, J. A. Delettrez, S. X. Hu, J. A. Marozas, A. V. Maximov, D. T. Michel, P. B. Radha, S. P. Regan, T. C. Sangster, W. Seka, A. A. Solodov, J. M. Soures, C. Stoeckl, J. D. Zuegel, Direct-drive inertial confinement fusion: A review, Physics of Plasmas 22 (2015) 110501. doi:10.1063/1.4934714.

[18] R. McCrory, et. al., OMEGA ICF experiments and preparation for direct drive ignition on NIF, Nuclear Fusion 41 (2001) 1413–1422. doi:10.1088/0029-5515/41/10/309.

[19] G. I. Taylor, The instability of liquid surfaces when accelerated in a direction perpendicular to their planes, Proceedings of the Royal Society of London. Series A. Mathematical and Physical Sciences 201 (1950) 192–196.

[20] T. Rayleigh, Investigation of the Character of the Equilibrium of an Incompressible Heavy Fluid of Variable Density, Proceedings of the London Mathematical Society s1-14 (1882) 170–177.

[21] B. Srinivasan, X.-Z. Tang, The mitigating effect of magnetic fields on Rayleigh-Taylor unstable inertial confinement fusion plasmas, Physics of Plasmas 20 (2013) 056307.

[22] C. Samulski, B. Srinivasan, M. J.-E. Manuel, R. Masti, J. P. Sauppe, J. Kline, Deceleration-stage Rayleigh-Taylor growth in a background magnetic field studied in cylindrical and Cartesian geometries, Matter and Radiation at Extremes 7 (2022) 026902. doi:10.1063/5.0062168.

[23] E. Ott, Nonlinear Evolution of the Rayleigh-Taylor Instability of a Thin Layer., Physical Review Letters 29 (1972) 1429–1432.

[24] B. Srinivasan, X.-Z. Tang, On the study of hydrodynamic instabilities in the presence of background magnetic fields in high-energy-density plasmas, EPL (Europhysics Letters) 107 (2014) 65001.

[25] M. J.-E. Manuel, B. Khiar, G. Rigon, B. Albertazzi, S. R. Klein, F. Kroll, F. E. Brack, T. Michel, P. Mabey, S. Pikuz, J. C. Williams, M. Koenig, A. Casner, C. C. Kuranz, On the study of hydrodynamic instabilities in the presence of background magnetic fields in high-energy-density plasmas, Matter and Radiation at Extremes 6 (2021) 026904. doi:10.1063/5.0025374.

[26] L. Perkins, D.-M. Ho, B. Logan, G. Zimmerman, M. Rhodes, D. Strozzi, D. Blackfield, S. Hawkins, The potential of imposed magnetic fields for enhancing ignition probability and fusion energy yield in indirect-drive inertial confinement fusion, Physics of Plasmas 24 (2017) 062708.

[27] J. P. Knauer, O. V. Gotchev, P. Y. Chang, D. D. Meyerhofer, O. Polomarov, R. Betti, J. A. Frenje, C. K. Li, M. J.-E. Manuel, R. D. Petrasso, J. R. Rygg, F. H. Seguin, Compressing magnetic fields with high-energy lasers, Physics of Plasmas 17 (2010) 056318. doi:10.1063/1.3416557.

[28] H. Alfvén, Existence of electromagnetic-hydrodynamic waves, Nature 150 (1942) 405–406.

[29] B. E. Morgan, J. A. Greenough, Large-eddy and unsteady RANS simulations of a shock-accelerated heavy gas cylinder, Shock Waves 26 (2016) 355–383. URL: https://doi.org/10.1007/s00193-015-0566-3. doi:10.1007/s00193-015-0566-3.

[30] R. Masti, C. Ellison, J. King, P. Stoltz, B. Srinivasan, Cross-code verification and sensitivity analysis to effectively model the electrothermal instability, High Energy Density Physics 38 (2021) 100925. URL: https://www.sciencedirect.com/

science/article/pii/S1574181821000045. doi:https://doi.org/10.1016/j.hedp.2021.100925.

[31] C. W. Cranfill, EOSPAC: a subroutine package for accessing the Los Alamos Sesame EOS data library (1983). URL: https://www.osti.gov/biblio/5719609.

[32] SESAME '83: report on the Los Alamos Equation-of-State Library (1983). URL: https://www.osti.gov/biblio/6349782.

[33] F. F. Chen, S. E. Von Goeler, Introduction to Plasma Physics and Controlled Fusion Volume 1: Plasma Physics, Second Edition, Physics Today 38 (1985) 87–88. URL: https://doi.org/10.1063/1.2814568. doi:10.1063/1.2814568.

[34] M. P. Desjarlais, J. D. Kress, L. A. Collins, Electrical conductivity for warm, dense aluminum plasmas and liquids, Phys. Rev. E 66 (2002) 025401. URL: https://link.aps.org/doi/10.1103/PhysRevE.66.025401. doi:10.1103/PhysRevE.66.025401.

[35] B. Fryxell, K. Olson, P. Ricker, F. X. Timmes, M. Zingale, D. Q. Lamb, P. MacNeice, R. Rosner, J. W. Truran, H. Tufo, FLASH: An Adaptive Mesh Hydrodynamics Code for Modeling Astrophysical Thermonuclear Flashes, The Astrophysical Journal Supplement Series 131 (2000) 273. URL: https://dx.doi.org/10.1086/317361. doi:10.1086/317361.

[36] FLASH User's Guide, 2021.

[37] C. Samulski, Deceleration Stage Rayleigh-Taylor Instability Growth in Inertial Confinement Fusion Relevant Configurations, Master's thesis, 2021.

[38] D. Clark, C. Weber, A. Kritcher, J. Milovich, P. Patel, S. Haan, B. Hammel, J. Koning, M. Marinak, M. Patel, C. Schroeder, S. Sepke, M. Edwards, Modeling and projecting implosion performance for the National Ignition Facility, Nuclear Fusion 59 (2018) 032008. URL: https://doi.org/10.1088/1741-4326/aabcf7. doi:10.1088/1741-4326/aabcf7.

Chapter 2

Deceleration-stage Rayleigh Taylor Growth in a Background Magnetic Field Studied in Cylindrical and Cartesian Geometries

Deceleration-stage Rayleigh Taylor Growth in a Background Magnetic Field Studied in Cylindrical and Cartesian Geometries

C. Samulski[a], B. Srinivasan[a], M. J.-E. Manuel[b], R. Masti[a], J. P. Sauppe[c], J. Kline[c]

[a] *Virginia Polytechnic Institute and State University, Blacksburg, VA 24060, USA*
[b] *General Atomics, San Diego, CA , USA*
[c] *Los Alamos National Laboratory, P.O. Box 1663, Los Alamos, New Mexico 87545, USA*

Abstract

Inertial confinement fusion experiments have identified the Rayleigh-Taylor (RT) instability as one of the largest inhibitors to achieving fusion. Consequently, mitigation strategies to reduce RT growth and mix in the hot-spot during the deceleration phase of the implosion are of great interest. In this work, the effect of seed magnetic fields on deceleration-phase RT growth are studied in planar and cylindrical geometries under conditions relevant to NIF and Omega experiments. FLASH's magnetohydrodynamic (MHD) and resistive-MHD capabilities are used to model the imploding cylinders and planar blast-wave driven targets. Realistic target and laser parameters are presented that suggest morphological differences in late-time RT evolution in the cylindrical National Ignition Facility (NIF) case and a measurable difference in the spike height of single-mode growth in the planar NIF case. This study predicts the need for target designs to utilize an RT-unstable foam-foam interface in order to achieve sufficient magnetic field amplification to alter the RT evolution. Benchmarked FLASH simulations are used to study these magnetic field effects in resistive and ideal MHD.

1. Introduction

Pre-magnetization of inertial confinement fusion (ICF) targets has been proposed as a means to achieving high-energy-gain due to the reduced ignition threshold and increased yield [1, 2]. One of the instabilities identified as a primary contributor to degradation of ICF implosions [3, 4], is the Rayleigh Taylor (RT) instability [5, 6]. The presence of the RT instability in an ICF capsule disrupts the convergence, which in turn can reduce the hotspot temperatures necessary for ignition. While RT spikes are predicted to generate magnetic fields in the hot-spot, they do not significantly alter the hydrodynamics or thermal conduction [7, 8, 9].

Mitigation of RT instability growth [10, 11, 12] and fuel-ablator mix [13, 14, 15, 16] in ICF implosions is pivotal to improving capsule performance; one such scheme is the use of strong pre-seeded magnetic fields [1, 17]. The RT instability has been well studied both computationally and experimentally in the ablative acceleration phase of ICF implosions, but deceleration-phase RT directly impacts the hot-spot. The deceleration phase occurs when the low-density, high-pressure interior begins pushing back on the higher density, lower pressure imploding liner. Some theoretical work [18, 19] has been performed, and experimental efforts [20, 21, 22, 23, 24] are beginning to probe cylindrical implosions in non-magnetized targets specifically to study deceleration-phase RT in a converging geometry. Additionally, a great deal of work has been done on planar blast-wave driven RT instability growth [25, 26, 27, 28, 29, 30] particularly in an astrophysical context, though most of the magnetization taken in to consideration is explored as self-generated magnetic fields [31, 32, 33, 34].

Magneto-Rayleigh-Taylor (MRT) instabilities are known to occur in the cylindrical geometry of imploding liners in pulsed-power magneto-inertial fusion experiments such as MagLIF (Magnetized Liner Inertial Fusion) [35, 36]. Experiments have measured MRT growth on the Z facility and have compared to MRT theory in cylindrical geometry [37]. The presence of seeded axial magnetic fields in combination with azimuthal magnetic fields that occur in the Z-pinch could significantly impact RT growth and development in MagLIF [38, 39]. Hence, investigating the effect of magnetic fields in RT instability development in cylindrical geometry can play a significant role in mitigating the growth of the instability in laser- and pulsed-power-driven concepts.

The standard evolution of the RT instability is commonly understood via the classical description of two fluids with differing densities (ρ_1 and ρ_2, where $\rho_2 > \rho_1$) subject to a constant acceleration (g) opposing the density gradient. A perturbation at the interface with wave number k ($k = 2\pi/\lambda$) results in a growth rate of $\gamma_c^2 = gkA_t$, where $A_t = (\rho_2 - \rho_1)/(\rho_2 + \rho_1)$ is the Atwood number. In

*Bhuvana Srinivasan
Email addresses: csamulski@vt.edu (C. Samulski), srinbhu@vt.edu (B. Srinivasan), manuelm@fusion.gat.com (M. J.-E. Manuel), rlm7819@vt.edu (R. Masti), jpsauppe@lanl.gov (J. P. Sauppe), jkline@lanl.gov (J. Kline)

the presence of a magnetic field, the growth rate becomes [40, 41]

$$\gamma_B^2 = gkA_t - \frac{2B^2k^2cos^2\theta}{\mu_0(\rho_2 - \rho_1)} \quad (1)$$

where θ is the angle between the magnetic field and the wave vector $\mathbf{k}$. The immediate impact of the magnetic field on RT is noted through a critical wavelength, $\lambda_c = \frac{4\pi B^2 cos^2\theta}{\mu_0 g(\rho_2-\rho_1)}$, such that perturbations with a wavelength smaller than λ_c are stabilized.

A magnetic field inside an an ICF implosion will amplify due to magnetic flux compression [1, 2]. Due to this amplification, magnetic fields are predicted to impact the RT spike morphology and subsequent Kelvin Helmholtz (KH) evolution [1, 10]. The level of field amplification is characterized by the magnetic Reynolds number, R_m, which is a measure of the ratio of fluid advection to magnetic diffusion. When $R_m >> 1$, the fluid is highly conducting, and a seeded magnetic field is approximately frozen in [1]. Plasma conditions in the hot-spot produce R_m approximately 10^4, suggesting amplification factors of several hundred [11]. Under these conditions, an appropriately applied seed magnetic field may help to reduce RT growth and mix in the hot-spot, producing a more efficient implosion.

Deceleration phase RT has the potential to truly disrupt convergence of ICF implosions by mixing the cold ablator with the hot fuel. Using appropriately-aligned seeded magnetic fields can produce conditions in which the RT instability could be mitigated with sufficient amplification ($R_m >> 1$). Additionally, the ratio of the dynamic pressure to magnetic pressure, β, ($\beta = 2\mu_0\rho u^2/\mathrm{B}^2$) characterizes the level to which the magnetic field can alter hydrodynamic evolution. Hydrodynamic systems with a low beta ($\beta \lesssim 1$) will be greatly affected by a B-field. Recent computational and experimental work [12] suggests morphological effects in deceleration-phase RT evolution begin to occur at $\beta \lesssim 100$.

The work presented here studies the impact of magnetic fields on the RT instability in planar and cylindrical geometries. Planar geometry is relatively simple to diagnose, while cylinders retain diagnostic access and incorporate the effects of geometric convergence. Cylinders have been used to study hydrodynamic instabilities for many years [42, 43, 44], and Los Alamos National Laboratory has recently revitalized such a platform [23, 22, 21]. Both the planar target and the cylinder consist of a high-density pusher layer that is accelerated into a lower density foam via laser direct-drive. This work considers targets designed for both the Omega [45] and the National Ignition Facility (NIF) [46]. With additional development seeded background magnetic fields of approximately 30 T may become accessible on NIF and Omega, so a solid density Omega-scale cylindrical configuration and a foam configuration for Omega-scale planar and NIF-scale cylindrical and planar targets are simulated.

Understanding the potential effects of a seed magnetic field on RT instability growth are the primary motivation for this work. Large magnetic Reynolds number is required to access the regimes where magnetic stabilization can occur, but this requires sufficiently high temperatures. This is evident in the standard Spitzer resistivity model, where the resistive diffusion of magnetic field scales inversely with temperature. The standard model of using resistivity for an ICF implosion requires that the resistivity be sufficiently small such that the diffusive effects are limited. The work presented here focuses on simulations performed using radiation hydrodynamics only (HD), ideal magnetohydrodynamics (MHD), or resistive MHD models in cylindrical and planar geometries.

This paper is structured as follows. Section 2 presents code descriptions for FLASH, and Section 3 presents simulation results using a cylindrical design at Omega and the NIF. Section 4 discusses simulation results of an experiment on Omega and the NIF using a planar platform.

The key contributions of this paper are as follows. First, this work compares the expected results for a magnetized solid density ICF target to those of a novel foam target design. Second, the work presented here also predicts relevant parameters necessary to achieve the desired temperatures and magnetic Reynolds numbers under which a magnetized ICF experiment will see mitigating impacts from an externally applied magnetic field.

2. Numerical Model

The models and numerical methods used are briefly outlined in this section. FLASH is an Eulerian multi-physics radiation-hydrodynamics code developed by the FLASH Center, now located at the University of Rochester, [47] with adaptive mesh refinement capabilities, which are used to solve hyperbolic and stiff parabolic systems. The ICF configurations presented are modeled with the Euler equations, the ideal-MHD equations, and the resistive-MHD equations from FLASH [48]. The specific Euler equations used in this study are given as [49],

$$\frac{\partial \rho}{\partial t} + \nabla \cdot [\rho \mathbf{u}] = 0, \quad (2)$$

$$\frac{\partial \mathbf{u}\rho}{\partial t} + \nabla \cdot [\rho \mathbf{u}\mathbf{u}] + \nabla P = \rho \mathbf{g} \quad (3)$$

$$\frac{\partial \rho E}{\partial t} + \nabla \cdot [(\rho E + P)\,\mathbf{u}] = \rho \mathbf{u} \cdot \mathbf{g} \quad (4)$$

where ρ, $\mathbf{u}$, and P are the fluid density, velocity, and pressure respectively, and E is the sum of the internal energy, $\mathbf{g}$ is acceleration, and lastly t is the time coordinate. For the MHD systems FLASH solves [49],

$$\frac{\partial \rho}{\partial t} + \nabla \cdot (\rho \mathbf{u}) = 0, \quad (5)$$

$$\frac{\partial \rho \mathbf{u}}{\partial t} + \nabla \cdot \big((\rho \mathbf{u})\mathbf{u} - \mathbf{B}\mathbf{B}\big) + \nabla p_* = \rho \mathbf{g} \quad (6)$$

$$\frac{\partial \rho E}{\partial t} + \nabla \cdot \big(\mathbf{u}\left(\rho E + p_*\right) - \mathbf{B}\left(\mathbf{u}\cdot\mathbf{B}\right)\big) = \rho \mathbf{g}\cdot\mathbf{u} + \nabla\cdot\left(\sigma\nabla T\right) + \nabla\cdot\big(\mathbf{B}\times\left(\eta\nabla\times\mathbf{B}\right)\big), \quad (7)$$

and

$$\frac{\partial \mathbf{B}}{\partial t} + \nabla\cdot\left(\mathbf{u}\mathbf{B} - \mathbf{B}\mathbf{u}\right) = -\nabla\times\left(\eta\nabla\times\mathbf{B}\right), \quad (8)$$

where,

$$p_* = p + \frac{B^2}{2}, \quad (9)$$

$$E = \frac{1}{2}\mathbf{u}^2 + \epsilon + \frac{1}{2}\frac{B^2}{\rho}, \quad (10)$$

and T is the temperature, the magnetic field is given by $\mathbf{B}$, $\mathbf{g}$ is the acceleration, p is the thermal pressure, σ is the heat conductivity, and η is the resistivity. FLASH uses a tabulated equation-of-state (EOS) to close the system [49]. For the ideal-MHD cases resistivity is neglected in equations 7 and 8. In all equations the internal energy, ϵ is calculated separately in FLASH using [49],

$$\frac{\partial \rho\epsilon}{\partial t} + \nabla\cdot\left(\left(\rho\epsilon + P\right)\mathbf{u}\right) - \mathbf{u}\cdot\nabla P = 0. \quad (11)$$

The resistive-MHD cases presented use a Spitzer form [50] of resistivity in the FLASH code given by [49],

$$\eta_\perp = \frac{m_{ele}}{e^2 n_{ele}\tau_{ele}} \quad (12)$$

$$\eta_\parallel = \frac{\eta_\perp}{1.96} \quad (13)$$

where m_{ele}, e, n_{ele}, and τ_{ele} are mass, charge, number density, and collision time of the electrons, respectively. $\eta_\perp$ and $\eta_\parallel$ represent the resistivity perpendicular and parallel to the magnetic field, of which $\eta_\parallel$ is used in the simulations because the Hall parameter is much less than 1. The magnetic Reynolds number is defined as,

$$R_m = \frac{UL}{D} \quad (14)$$

where U is the fluid velocity, L is the perturbation wavelength, and D is diffusivity. For the resistive-MHD cases D in equation 14 is equal to diffusivity, $\eta_\parallel/\mu_0$; however for the ideal-MHD cases D is estimated with,

$$\eta_{est} = 3.3\times10^{-9}\frac{Z_i ln\Lambda}{T_e^{\frac{3}{2}}}, \quad (15)$$

where $ln\Lambda$ is estimated to be 2 (in FLASH [49] the minimum value is set to 1), Z_i is the local average ionization, and T_e is the local temperature in eV.

3. Cylindrical Configurations

3.1. Cylindrical Model Tuning

The parameters used for the cylindrical simulations, performed by modeling targets in 2D in the radial and axial frame of reference (r-z), are derived from an experiment performed using the Omega laser facility. In particular, the configuration derived for the verification of FLASH can been seen in Figure 1 [21]. Using a laser drive of 18 kJ over 1 ns, 2D FLASH simulations are verified against existing experimental data from Omega shots whose configuration can be found in [23].

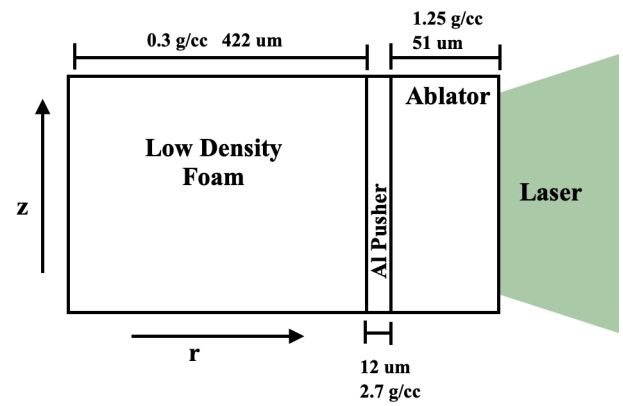

Figure 1: A schematic of the directly driven cylindrical Omega configuration used for the validation of FLASH and the HD, ideal-MHD, and resistive-MHD simulations. The configuration shows all relevant densities and length scales used [21].

FLASH calculations of the radial shock location are shown to compare well with experimental data collected over a series of 4 shots, see Figure 2. As can be seen in this comparison, FLASH shows very reasonable agreement with the shock trajectories extracted from the available experimental data. This agreement provides confidence in FLASH's ability to simulate the bulk hydrodynamic motion in an r-z geometry which dictates RT growth during the deceleration phase.

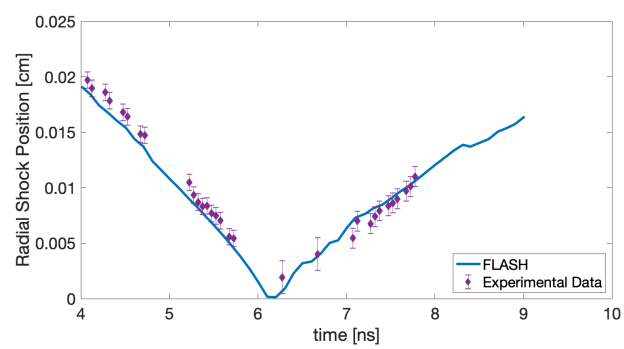

Figure 2: FLASH simulation benchmarked against experimental data for the described configuration. The FLASH data is represented by the solid blue line, and the purple markers are derived from experimental data analyzed by hand with the error bars representing the σ variation in shock position as a function of azimuthal angle [23].

3.2. Cylindrical RT on Omega

Simulations to address magnetic field effects on cylindrical RT are based on a recent design study [20] where the low-density foam is decreased to $0.06\,\mathrm{g\,cm^{-3}}$. A lower laser drive of 8 kJ is used in this work. A perturbation along the z direction of $\lambda = 40\,\mu\mathrm{m}$ and a sinusoidal amplitude of 5 µm is added to the interior Aluminum tracer surface. These simulations are performed using FLASH's HD, ideal-MHD, and resistive-MHD schemes. The seed background magnetic field for the MHD cases oriented parallel to the perturbation vector are 10 T, 25 T, and 50 T. The configuration was deliberately chosen such that the perturbation wavelength would be larger than the λ_c. The λ_c for the three cases presented are $0.03\mu m$, $0.17\mu m$, and $0.7\mu m$ corresponding to magnetic fields of 10 T, 25 T, and 50 T, respectively. Distinct RT instability growth is noted on the interior of shell during the deceleration phase of the implosion when modeled using HD, see Figure 3.

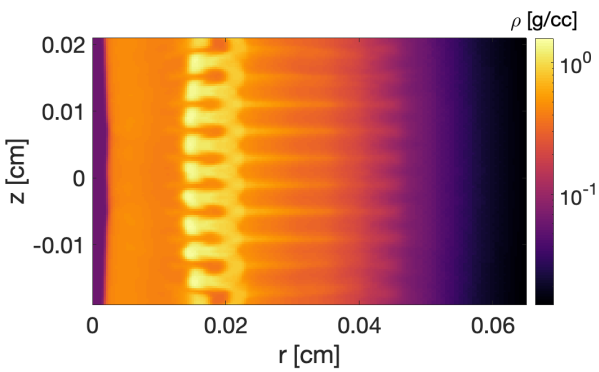

Figure 3: A density plot of cylindrical Omega-based experimental configuration simulated in HD, predicting deceleration stage RT instability growth after 5.4 ns.

Figure 4 illustrates this solid-density configuration modeled in ideal-MHD and resistive-MHD 5.4 ns into the implosion at 10 T, 25 T, and 50 T. The ideal-MHD density plots show that the nonlinear evolution modeled in these simulations produces stronger reduction in growth at higher seed magnetic field strengths. The ideal-MHD simulations at 10 T have little difference in morphology when compared to the HD case, while the 25 T case illustrates the RT bubble morphology being diminished when using ideal-MHD compared to HD. In the 50 T case, the overall morphology and growth of the RT spikes is more significantly impacted by the reduced growth when using ideal-MHD compared with HD. While the ideal-MHD results have progressively clear and notable reduction in RT spike growth and morphology, in the resistive-MHD simulations, the addition of the diffusive effects of resistivity to Equation 8, reduces the magnetic field amplification during the implosion. This in turn reduces the impact the magnetic fields have on RT spike growth.

The magnetic fields that are presently achievable and those that are expected to be achievable, in the next generation of coil designs, have little impact on the RT spike growth when using a resistive-MHD model. This can clearly be seen in Figure 5, showing the measurement over the course of the implosion of the RT spike growth from the top of the RT instability bubble, the peak, to the lowest point between RT spikes, the valley. As such, it predicts that the ideal-MHD regime provides an up to 40 µm measurable reduction in RT spike growth, while the HD and resistive-MHD schemes present an RT spike growth difference on the order of only a few microns. This suggests that in the case of solid density shells, with small seed background fields, the HD case would capture the expected RT instability growth and morphology that a resistive-MHD scheme would predict. This is notable given that in the resistive-MHD cases the magnetic field amplification is on the order of three times the seeded field in the surrounding plasma for 50 T, 25 T, and 10 T seed fields in comparison to 400 T, 300 T, and 200 T, respectively, for the ideal-MHD cases corresponding to the same seed fields. Figure 6 presents significant amplification of the magnetic field in the ideal-MHD and resistive-MHD cases, however the resistive-MHD amplification is located in the shock-front whereas the ideal-MHD amplification occurs in the region where the RT instability grows behind the shock. Additionally, the resistive-MHD magnetic field only supersedes the ideal-MHD when peak compression occurs, which is likely due to the peak magnetic field being located in the shock front of the resistive-MHD cases and reaching the central axis of the cylinder earlier in time than in the ideal-MHD cases. The large magnetic field amplification that is occurring supersedes other magnetic fields, such as the self generated Biermann battery magnetic field. The lower temperatures and magnetic Reynolds numbers associated with these solid density cylindrical implosions are responsible for the decreased impact of the magnetic fields on the RT instability growth.

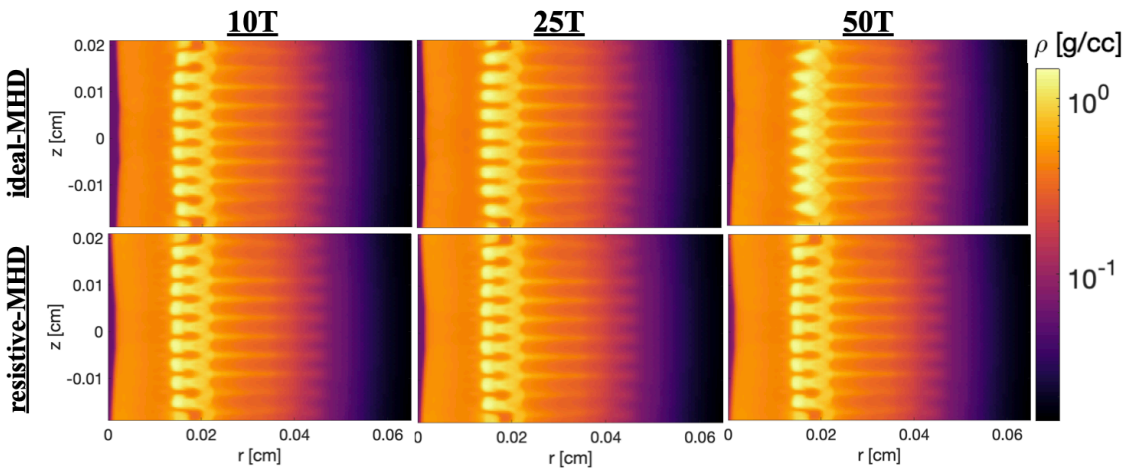

Figure 4: RT instability growth during deceleration using cylindrical Omega experimental parameters, modeled in ideal-MHD and resistive-MHD with 10 T, 25 T, and 50 T background fields.

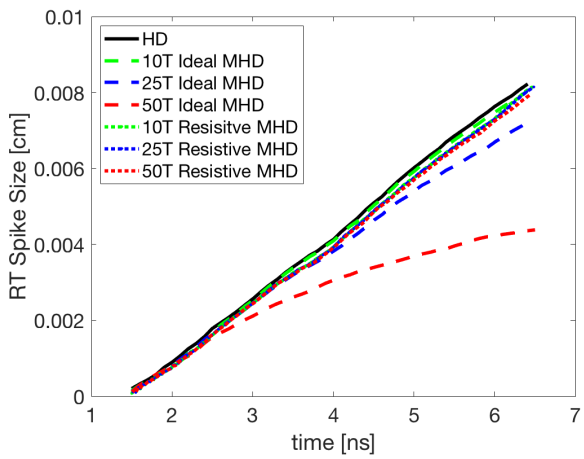

Figure 5: Measured growth of the RT instability in HD, ideal-MHD, and resistive-MHD for the cylindrical Omega configuration. These simulations indicate that the expected diffusion of the magnetic field in resistive-MHD precludes any mitigating effect on RT growth predicted by ideal-MHD.

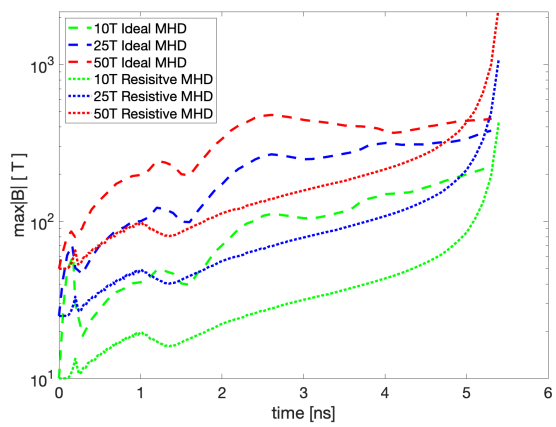

Figure 6: The maximum magnetic field in the simulation domain during the course of the implosion for the 10 T, 25 T, and 50 T ideal-MHD and resistive-MHD cases. The ideal-MHD cases have consistently higher peak magnetic fields until maximum compression.

The ideal-MHD cases produce temperatures in and around the unstable interface on the order of 25 eV and 16 eV within the RT bubbles and spikes, respectively. These low temperatures correspond to low estimated magnetic Reynolds numbers of approximately 3 near the interface. In comparison, the resistive MHD cases produce comparable plasma temperatures and magnetic Reynolds numbers of approximately 6, giving a clear indication that field amplification is insufficient to produce fields strong enough to alter RT evolution in a measurable way. To achieve higher magnetic Reynolds numbers, the laser drive should be increased and the pusher density reduced to increase the temperatures near the unstable interface.

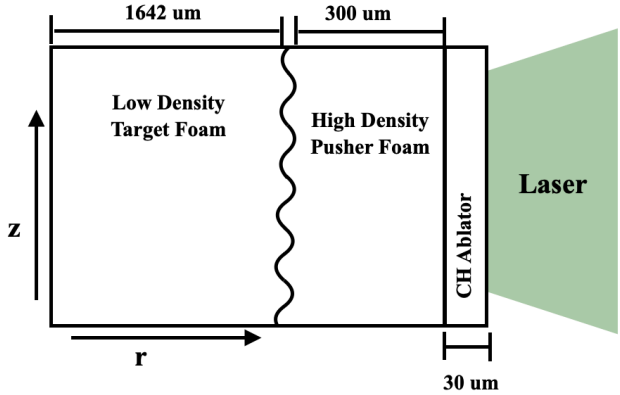

Figure 7: A schematic of the cylindrical NIF configuration developed for simulations in HD, ideal-MHD, and resistive-MHD models. The cylindrical target for NIF would consist of a 30 µm thick solid density CH ablator, a nickel-doped foam pusher of thickness 300 µm at a density of $0.215\,\mathrm{g\,cm^{-3}}$, and a low-density CH foam of $0.02\,\mathrm{g\,cm^{-3}}$ and a thickness of 1.6 mm, as seen in Figure 7. A perturbation with a $\lambda = 120\,\mu\mathrm{m}$ and an sinusoidal amplitude of 40 µm is added to the nickel-doped foam at the interface with the low density target foam.

3.3. Cylindrical RT on NIF

The cylindrical NIF configuration is based on a set of NIF scaled Omega parameters [22], which leads to a direct-drive NIF laser energy of 226 kJ. A modification is made to the cylindrical target that switches the solid density Al marker for a nickel-doped foam, motivated by planar target designs which will be discussed subsequently. The cylindrical target for NIF is described in Figure 7, where the pusher has been adjusted to be a high-density nickel-doped foam. A perturbation of $\lambda = 120\,\mu\mathrm{m}$ and an sinusoidal amplitude of 40 µm, chosen to be larger than the critical wavelength of $6\mu m$, is added to the nickel-doped foam at the interface with the low density target foam. This configuration is simulated with only a 30 T magnetic field, comparable to those previously achieved on the NIF.

The difference in RT spike size and morphology between HD and ideal-MHD is again notable, as seen from Figure 8. However, unlike in the previously discussed Omega configuration which uses a solid density Al marker, Figure 8 shows the resistive-MHD model also presenting a difference in the RT bubble compared to the HD case. The difference when using resistive-MHD is seen in RT morphology in the bubble and spike compared to HD and ideal-MHD. The overall spike growth, however, is not significantly different between the HD and resistive-MHD cases, as noted from Figure 11, until late-in-time when using resistive-MHD. All three models show the RT spikes developing well behind the shock front, which is the region where the highest temperatures are reached. Consequently, the plasma in and around the RT spikes reaches temperatures on the order of 60 eV.

The magnetic Reynolds numbers, seen in Figure 9, only reach approximately 5 in the bubble and approximately 10 in front of the RT spikes. These low magnetic Reynolds numbers are in part due to the temperature and decreasing velocities of the plasma during the deceleration. The low magnetic Reynolds numbers result in low magnetic field amplification. Figure 10 shows the plasma β values reaching several thousand at the center of the RT instability bubbles and dropping rapidly to approximately 50 at the front of the RT spike growth. At these β levels, the system is only beginning to approach the regime where the morphological magnetic field effects may be expected.

Despite the RT instability morphology being different in the resistive-MHD case, the resistive-MHD simulations with 30 T seed magnetic field present little reduction in the RT spike size, seen in Figure 11. Specifically, secondary features seen growing at the top of the RT instability bubbles in the HD case are damped in size, as shown in Figure 8. The late-time difference in spike size between the HD and resistive-MHD cases from Figure 11 reaches 50 µm when optimistically incorporating the secondary features growing on top of the spikes in the HD case, this may be measurable experimentally with axial radiographs. The detailed morphology of these small-scale secondary features would be significantly more difficult to measure in an experiment than a simple reduction in spike size.

Tables 1 and 2 provide approximate values for important plasma parameters for all the configurations at locations within the RT spikes where the material is 90% pusher and 90% low density foam, respectively. Note that for the Omega cylindrical configuration, the temperature, χ, and R_m are substantially smaller than the NIF cylindrical configuration, whereas the Re and Pe_L are larger in the Omega cases compared to the NIF cases. Additionally, the difference between the pusher-dominant region (Table 1) and the low density foam-dominant region (Table 2) of the RT instability lies primarily in the temperature and plasma β, with small differences in R_m between the regions and substantial differences in the Re and Pe_L between the regions. The planar configurations discussed in the following sections achieve notably higher temperatures and R_m, while maintaining small Hall parameter values along with large Reynolds numbers and Peclet numbers.

4. Planar Configurations

Given the solid densities used in the Omega cylindrical configuration and primarily morphological effects of the seed magnetic field in the NIF cylindrical configuration, an effort to explore planar foam targets on Omega and NIF-scale powers is under way.

4.1. Planar RT on Omega

Additional configurations are designed to study a blast-wave driven deceleration stage RT instability growth, utilizing a laser to drive an implosion of a planar target in which a high-density pusher foam is machined with a sinusoidal perturbation and is driven into a low-density foam, seen in Figure 12. A seed background magnetic field of

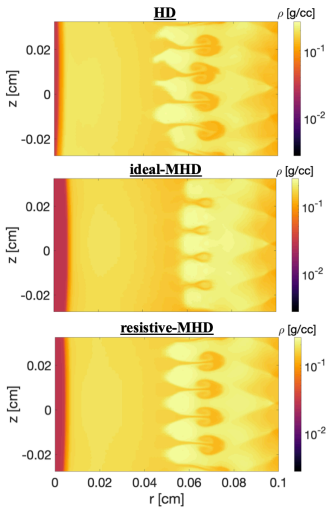

Figure 8: Density plots 14.6 ns into the implosion of the cylindrical NIF experimental parameters, modeled using HD, ideal-MHD, and resistive-MHD, the latter two with a 30 T background field. The difference in RT spike height and morphology is distinguishable between the different models, note the morphology difference in RT bubble shape in the HD and resistive-MHD cases.

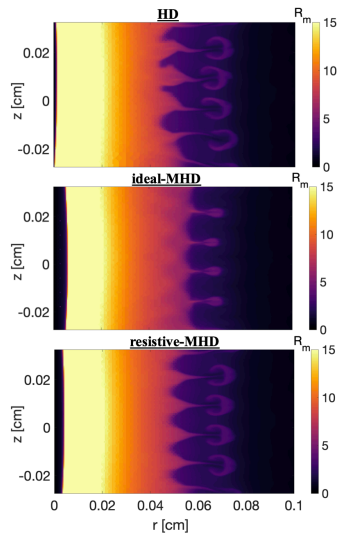

Figure 9: HD, 30 T ideal-MHD, and 30 T resistive-MHD plots of the magnetic Reynolds number at 14.6 ns using cylindrical NIF experimental parameters. The magnetic Reynolds numbers are comparable between HD and ideal-MHD with both close to 5 within the RT spikes and reaching 10 in the plasma in front of the RT instability bubbles.

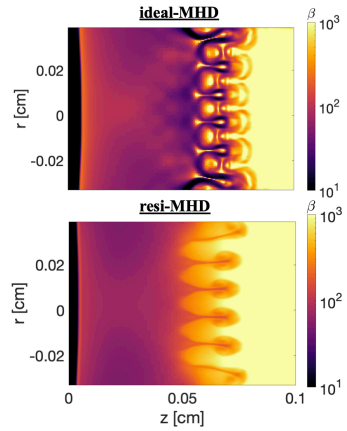

Figure 10: Plasma β for the 30 T ideal-MHD and resistive-MHD cases at 14.6 ns using cylindrical NIF experimental parameters. The plasma β is on the order of several hundred within the RT bubbles and on the order of 100 in front of the RT spikes in the resistive-MHD case. For ideal-MHD, the plasma β is on the order of tens in and around the RT spike growth and hundred within the RT spikes themselves.

Configuration	T (eV)	R_m	β	χ	Pe_L	Re
Omega Cylindrical resistive-MHD 25 T	18.7	1.0	2607	0.004	645	67035
Omega Cylindrical ideal-MHD 25 T	17.1	0.95	111	0.02	757	86392
Omega Cylindrical HD 0 T	18.5	0.99	-	-	720	71601
NIF Cylindrical resistive-MHD 30 T	53.1	7.5	328	0.06	130	6350
NIF Cylindrical ideal-MHD 30 T	52.9	6.1	38	0.15	107	5234
NIF Cylindrical HD 0 T	63.4	8.5	-	-	115	5628
NIF Planar resistive-MHD 30 T	81.2	42.6	434	0.28	110	8378
NIF Planar ideal-MHD 30 T	81.9	41.9	324	0.23	108	8109
NIF Planar HD 0 T	82	46.4	-	-	116	5933

Table 1: Plasma parameters of the RT instability at 90% pusher including, temperature, magnetic Reynolds number, plasma β, $ln\Lambda$, the Hall parameter, χ,the Peclet number, Pe_L, and the Reynolds number, Re.

12 T is applied to the ideal-MHD simulation. This target is then directly driven with a 2350 J laser drive for 2 ns, comparable to an Omega-EP experimental drive.

The RT instability growth is prominent during the deceleration stage, seen in density plots in Figure 13. Distinct small scale features are present in the HD cases and damped in the ideal-MHD along with the RT spike size being reduced overall as well. Additionally, the temperatures observed in these simulations are on the order of 40 to 45 eV in and around the RT instability, which is twice as hot as the previously discussed cylindrical Omega-scale target simulations. This increased temperature does result in a estimated magnetic Reynolds number that is higher in both the HD and ideal-MHD cases, seen in Figure 14; however, it is still only on the order of 5 to 8, thus is still too small for the impact of the 12 T seeded background magnetic field to be measurable in a resistive-MHD case. Consequently, shifting again to a NIF-like regime allows high laser drives which would result in higher temperatures and higher magnetic Reynolds numbers. This then increases the likelihood that a resistive-MHD simulation would lead to an RT spike growth that differs from the growth in HD simulations.

4.2. Planar RT on NIF

The planar configuration explored here is based on experimental parameters that are the point design for a direct-drive NIF campaign, and consist of a 30 µm thick CH ablator at a density of 1.0 g cm^{-3}, a 400 µm thick CH foam at a density of 0.215 g cm^{-3}, and a nickel-doped foam 400 µm thick and with a density of 0.235 g cm^{-3}. The target CH foam has a density of 0.02 g cm^{-3} and a thick-

Configuration	T (eV)	R_m	β	χ	Pe_L	Re
Omega Cylindrical resistive-MHD 25 T	35.9	1.9	613	0.016	96	5027
Omega Cylindrical ideal-MHD 25 T	33.6	1.8	165	0.03	114	6109
Omega Cylindrical HD 0 T	34.7	1.8	-	-	98	5171
NIF Cylindrical resistive-MHD 30 T	56.4	14.7	166	0.09	106	4265
NIF Cylindrical ideal-MHD 30 T	56.1	12.5	41	0.15	97	3942
NIF Cylindrical HD 0 T	59.8	15.7	-	-	94	3699
NIF Planar resistive-MHD 30 T	80.9	43	99	0.21	113	3995
NIF Planar ideal-MHD 30 T	81.1	42.6	52	0.39	105	3883
NIF Planar HD 0 T	82.1	45.1	-	-	121	4204

Table 2: Plasma parameters at the point of 90% low density foam in the RT instability growth including, temperature, magnetic Reynolds number, plasma β, the Hall parameter, Peclet number, and Reynolds number.

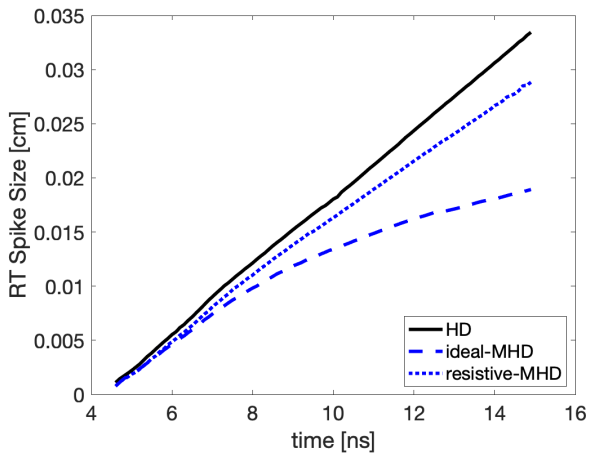

Figure 11: RT instability growth in HD, ideal-MHD, and resistive-MHD measured in the cylindrical NIF based configuration. The HD RT spike growth is seen in black, while the 30 T ideal-MHD growth is the blue dashed line, and the 30 T resistive-MHD spike growth can be seen in the blue dotted line. A difference in RT spikes is noted after 8 ns, thus the difference between the HD and resistive-MHD spike size could be experimentally measurable with axial radiographs.

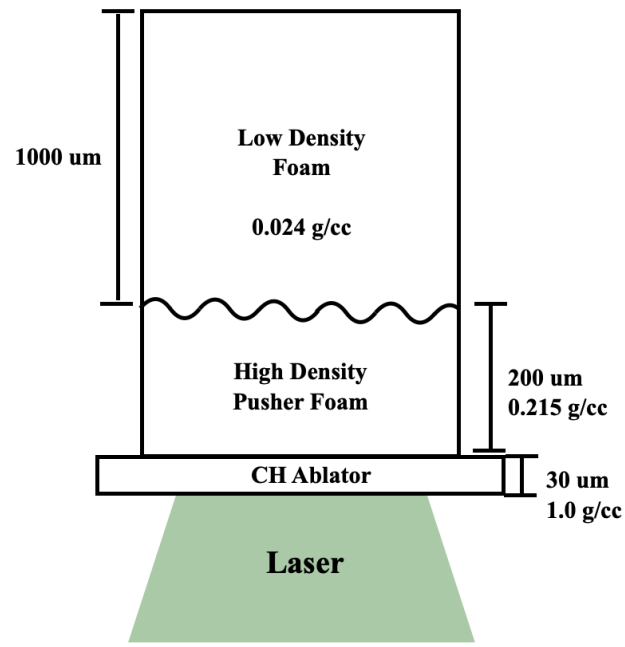

Figure 12: A schematic of the general configuration used for the directly driven planar targets on Omega. These targets consist of a high-density nickel doped foam with a sinusoidal perturbation with wavelength of λ= 80 µm and amplitude of 20 µm incident on a low-density CH foam.

ness of 3500 µm. The laser drive of this system is approximately 260 kJ. These simulations in HD, ideal-MHD, and resistive-MHD are performed until a time of 16 ns, with a sinusoidal perturbation with wavelength of $\lambda = 120$ µm and amplitude of 20 µm. The ideal-MHD and resistive-MHD cases are simulated with a seed background magnetic field of 30 T.

FLASH results for the planar NIF design at 12ns with a 30 T seed field are shown in Figure 15. The difference in RT morphology and spike growth is clearly distinguishable between the ideal-MHD case and the HD case. The resistive-MHD case also presents a difference in the RT spike growth and morphology when compared to the HD case and the ideal-MHD case. Additionally, the temperature around the RT spikes is on the order of 80 eV in HD, ideal-MHD, and resistive-MHD, and results in an estimated magnetic Reynolds number of 40 for HD and ideal-MHD verses an actual magnetic Reynolds number of 47 in resistive-MHD, seen in Figure 16. Such large magnetic Reynolds numbers indicate that the magnetic field amplification is substantial, and the plasma β suggests whether these conditions lend themselves to a regime where the RT spikes will be damped. The plasma β values achieved can be seen in Figure 17, where the plasma β in the RT spikes is high, but in front of the RT spikes the plasma beta on the order of a hundred. This suggests that for configurations that achieve similarly high temperatures and velocities, resistive-MHD should be used to best capture the impact a background magnetic field will have on the the RT spike growth and morphology.

The difference between each of the HD, ideal-MHD, and resistive-MHD models is noted in the peak-to-valley mea-

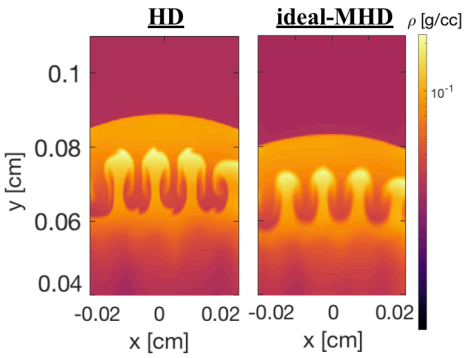

Figure 13: Density plots of the Omega-scale planar targets. The RT instability growth is shown at 7 ns during deceleration simulated in HD and ideal-MHD with a 12 T background magnetic field.

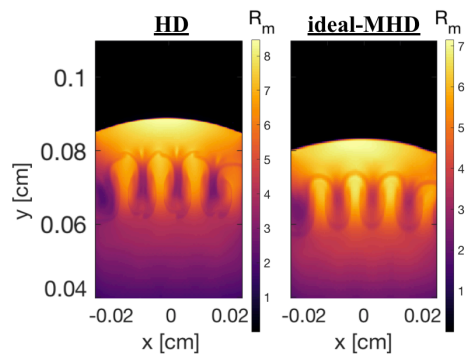

Figure 14: Magnetic Reynolds number of the Omega-scale planar target at 7 ns during deceleration in HD and 12 T ideal-MHD. Note magnetic Reynolds numbers in the 5-8 range using both models.

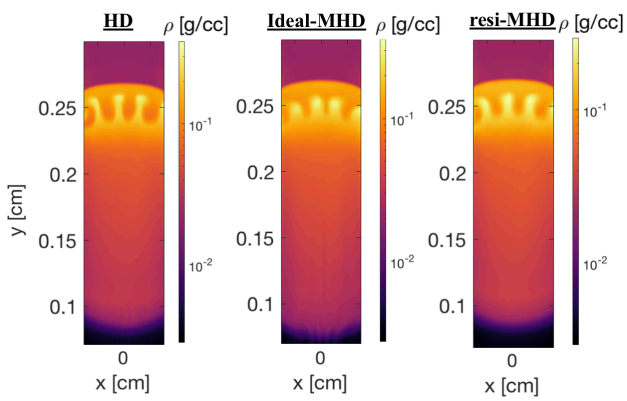

Figure 15: Density plots of RT instability growth during deceleration using planar NIF experimental parameters, modeled using HD, ideal-MHD and resistive MHD, the last two with 30 T background field, 12 ns into the implosion. The difference in RT spike height and morphology is distinguishable between the different models, with the ideal-MHD presenting a significantly damped RT spike growth.

surements of the RT spike growth in Figure 18. The resistive-MHD spike growth, in the blue dotted line, and the HD spike growth, in the solid black, show a 50 µm difference in RT spike size by 14 ns, which continues to increase given longer additional time to grow. Experiments validating such a measurable difference in RT instability growth are currently underway at NIF, in an effort to validate these simulation predictions.

5. Conclusions

The primary focus of this work is on the growth of the RT instability in the context of the deceleration stage of ICF relevant implosions, particularly the effect, or lack thereof, caused by a seed magnetic field on the RT instability's growth during deceleration. These RT instability configurations are studied using FLASH, solved first for the Euler equations and then extended to ideal-MHD in the presence of seed background magnetic fields of varying sizes. Finally, the addition of FLASH's Spitzer resistivity model is used to perform simulations using a more accurate resistive-MHD model. This introduces a diffusive effect into the domain providing a more realistic representation of what would be observed in an experiment. It is worth noting that Spitzer resistivity is used for the resistive-MHD simulations performed here, and studies of more accurate resistivity models for the materials and regimes considered here remain an open research area.

Following the comparison of FLASH's HD model to experimental data from the Omega laser, the Omega configurations in the cylindrical and Cartesian coordinate systems are simulated with a single mode. In both configurations the HD model presents notable RT spike growth on the interior interface during deceleration. The addition of seed background magnetic fields of 10 T, 25 T, and 50 T in the cylindrical system suggest a notable reduction in the RT spike size in the ideal-MHD cases. However, in the presence of resistivity there is little observable impact on the RT spikes in comparison to the HD case regardless of the strength of the initial magnetic field. This is also observed in the foam-foam planar Omega configuration where low temperatures and subsequent magnetic Reynolds numbers reached during deceleration indicate a resistive-MHD case would demonstrate no measurable difference in RT spike size compared to the HD model. Thus, similar configurations of the laser power and densities would benefit little from the added effort of modeling in resistive-MHD when the HD system provides the same results with less computational cost.

Shifting to a NIF configuration in which a higher laser power, larger targets, and high density pusher foam configurations are possible, an increase in temperature and magnetic Reynolds numbers is noted. These temperature and magnetic Reynolds number increases are not significant enough in the cylindrical foam-foam configuration to produce large enough magnetic Reynolds numbers. Thus, significant reduction in RT spike size is not seen in a

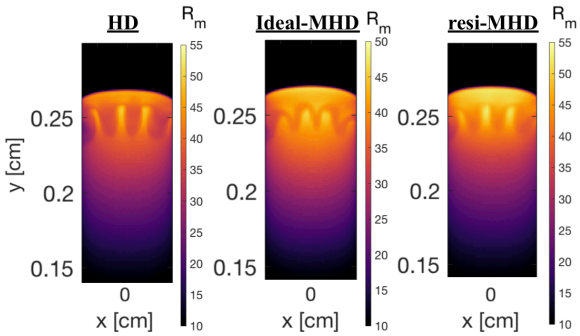

Figure 16: Plots using HD, ideal-MHD, and resistive-MHD showing the magnetic Reynolds number of the plasma in and around the RT spike growth at 12 ns using planar NIF experimental parameters. The magnetic Reynolds numbers differs slightly between HD, ideal-MHD, and resistive-MHD, but ultimately lies close to 40 in each case.

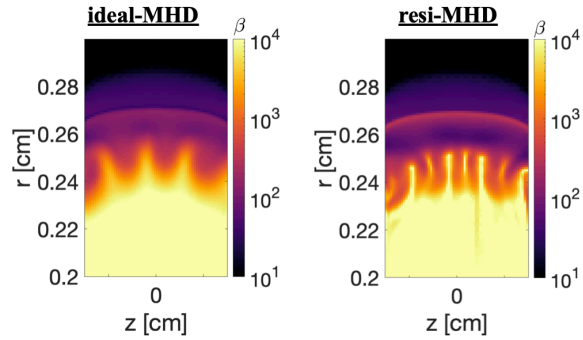

Figure 17: Plots using HD, ideal-MHD, and resistive-MHD showing the plasma β of the plasma in and around the RT spike growth at 12 ns using planar NIF experimental parameters. Note that the plasma β is on the order of 100 in front of the RT spikes and significantly higher inside the RT spikes.

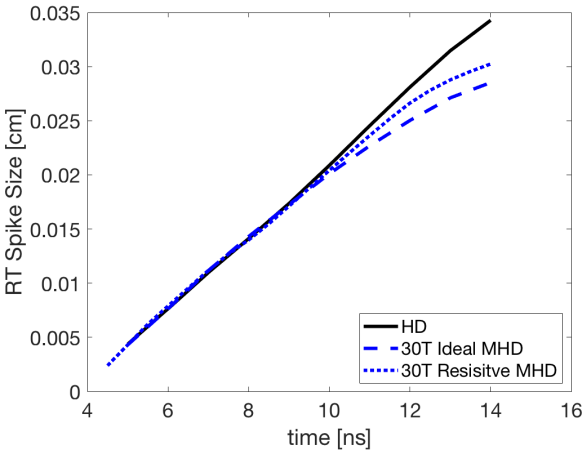

Figure 18: Measured growth of the RT instability in HD, ideal-MHD, and resistive-MHD for the planar NIF based experimental configurations. The HD RT growth is seen in black, while the 30 T ideal-MHD growth is the blue dashed line, and the 30 T resistive-MHD growth can be seen in the blue dotted line. A measurable difference in RT instability growth is notable after 10 ns.

resistive-MHD simulation when compared to a HD simulation, only small features in the RT morphology of this cylindrical foam-foam case are damped. The damping of these small secondary features may be experimentally measurable with axial radiographs, though the larger RT spike is not estimated to show much of a size difference. Due to limited space for growth before peak convergence in the cylindrical configuration, the RT instability does not grow sufficiently for the damping of the larger RT spikes to be measurable.

In the planar NIF configurations the damping effect of a 30 T magnetic field is observable within the RT spikes for both the ideal-MHD case and the resistive-MHD case. Temperatures on the order of 80-90 eV are observed and magnetic Reynolds numbers on the scale of 40-50 are seen in and around the RT spikes. These results culminate in Figure 18, which presents a measurable approximately 50 µm difference as noted in the RT spikes. For configurations driven with sufficiently increased laser power reaching temperatures on the order of 80 eV and magnetic Reynolds numbers of $\lessapprox$40, the use of resistive-MHD is imperative in accurately simulating the effect a magnetic field may have on the RT spike growth. Measuring the impact of background magnetic fields on the growth of the RT instability is still being pursued in an experimental context. Should these effects be replicated experimentally, the magnetic fields used in Z-pinches and concepts such as MagLIF (Magnetized Liner Inertial Fusion) [35] as well as the addition of magnetic fields in ICF experiments could contribute to mitigating the growth of the RT instability in these concepts.

Acknowledgement

This work was supported by the Office of Science of the U.S. Department of Energy under Award Nos. DE-SC0018993, DE-SC0016515, and DE-SC0022319 by the High Energy Density Laboratory Plasmas subprogram of the Fusion Energy Sciences program and under Award No. DE-SC0020055 by the Financial Assistance Program. This work was also supported through a Los Alamos National Laboratory subcontract to Virginia Tech under contract number 463281. The authors would like to acknowledge Advanced Research Computing at Virginia Tech for providing computational resources and technical support, and the FLASH Center for Computational Science for their constant feedback and access to the FLASH code developed by the DOE NNSA-ASC OASCR Flash Center at the University of Chicago.

References

[1] L. Perkins, D.-M. Ho, B. Logan, G. Zimmerman, M. Rhodes, D. Strozzi, D. Blackfield, S. Hawkins, The potential of imposed magnetic fields for enhancing ignition probability and fusion energy yield in indirect-drive inertial confinement fusion, Physics of Plasmas 24 (2017) 062708.

[2] J. P. Knauer, O. V. Gotchev, P. Y. Chang, D. D. Meyerhofer, O. Polomarov, R. Betti, J. A. Frenje, C. K. Li, M. J.-E. Manuel, R. D. Petrasso, J. R. Rygg, F. H. Seguin, Compressing magnetic fields with high-energy lasers, Physics of Plasmas 17 (2010) 056318. doi:10.1063/1.3416557.

[3] R. S. Craxton, K. S. Anderson, T. R. Boehly, V. N. Goncharov, D. R. Harding, J. P. Knauer, R. L. McCrory, P. W. McKenty, D. D. Meyerhofer, J. F. Myatt, A. J. Schmitt, J. D. Sethian, R. W. Short, S. Skupsky, W. Theobald, W. L. Kruer, K. Tanaka, R. Betti, T. J. B. Collins, J. A. Delettrez, S. X. Hu, J. A. Marozas, A. V. Maximov, D. T. Michel, P. B. Radha, S. P. Regan, T. C. Sangster, W. Seka, A. A. Solodov, J. M. Soures, C. Stoeckl, J. D. Zuegel, Direct-drive inertial confinement fusion: A review, Physics of Plasmas 22 (2015) 110501. doi:10.1063/1.4934714.

[4] R. McCrory, R. Bahr, R. Betti, T. Boehly, T. Collins, R. Craxton, J. Delettrez, W. Donaldson, R. Epstein, J. Frenje, V. Glebov, V. Goncharov, O. Gotchev, R. Gram, D. Harding, D. Hicks, P. Jaanimagi, R. Keck, J. Kelly, J. Knauer, C. Li, S. Loucks, L. Lund, F. Marshall, P. McKenty, D. Meyerhofer, S. Morse, R. Petrasso, P. Radha, S. Regan, S. Roberts, F. Séguin, W. Seka, S. Skupsky, V. Smalyuk, C. Sorce, J. Soures, C. Stoeckl, R. Town, M. Wittman, B. Yaakobi, J. Zuegel, OMEGA ICF experiments and preparation for direct drive ignition on NIF, Nuclear Fusion 41 (2001) 1413–1422. doi:10.1088/0029-5515/41/10/309.

[5] G. I. Taylor, The instability of liquid surfaces when accelerated in a direction perpendicular to their planes, Proceedings of the Royal Society of London. Series A. Mathematical and Physical Sciences 201 (1950) 192–196.

[6] T. Rayleigh, Investigation of the Character of the Equilibrium of an Incompressible Heavy Fluid of Variable Density, Proceedings of the London Mathematical Society s1-14 (1882) 170–177.

[7] M.-E. Manuel, C. Li, F. Séguin, J. Frenje, D. Casey, R. Petrasso, S. Hu, R. Betti, J. Hager, D. Meyerhofer, et al., First measurements of Rayleigh-Taylor-induced magnetic fields in laser-produced plasmas, Physical review letters 108 (2012) 255006.

[8] B. Srinivasan, G. Dimonte, X.-Z. Tang, Magnetic field generation in Rayleigh-Taylor unstable inertial confinement fusion plasmas, Physical review letters 108 (2012) 165002.

[9] B. Srinivasan, X.-Z. Tang, Mechanism for magnetic field generation and growth in rayleigh-taylor unstable inertial confinement fusion plasmas, Physics of Plasmas 19 (2012) 082703.

[10] B. Srinivasan, X.-Z. Tang, The mitigating effect of magnetic fields on Rayleigh-Taylor unstable inertial confinement fusion plasmas, Physics of Plasmas 20 (2013) 056307.

[11] B. Srinivasan, X.-Z. Tang, On the study of hydrodynamic instabilities in the presence of background magnetic fields in high-energy-density plasmas, EPL (Europhysics Letters) 107 (2014) 65001.

[12] M. J.-E. Manuel, B. Khiar, G. Rigon, B. Albertazzi, S. R. Klein, F. Kroll, F. E. Brack, T. Michel, P. Mabey, S. Pikuz, J. C. Williams, M. Koenig, A. Casner, C. C. Kuranz, On the study of hydrodynamic instabilities in the presence of background magnetic fields in high-energy-density plasmas, Matter and Radiation at Extremes 6 (2021) 026904. doi:10.1063/5.0025374.

[13] D. Clark, C. Weber, A. Kritcher, J. Milovich, P. Patel, S. Haan, B. Hammel, J. Koning, M. Marinak, M. Patel, C. Schroeder, S. Sepke, M. Edwards, Modeling and projecting implosion performance for the National Ignition Facility, Nuclear Fusion 59 (2018) 032008. URL: https://doi.org/10.1088/1741-4326/aabcf7. doi:10.1088/1741-4326/aabcf7.

[14] D. S. Clark, C. R. Weber, J. L. Milovich, A. E. Pak, D. T. Casey, B. A. Hammel, D. D. Ho, O. S. Jones, J. M. Koning, A. L. Kritcher, M. M. Marinak, L. P. Masse, D. H. Munro, M. V. Patel, P. K. Patel, H. F. Robey, C. R. Schroeder, S. M. Sepke, M. J. Edwards, Three-dimensional modeling and hydrodynamic scaling of National Ignition Facility implosions, Physics of Plasmas 26 (2019) 050601. doi:10.1063/1.5091449.

[15] B. M. Haines, C. H. Aldrich, J. M. Campbell, R. M. Rauenzahn, C. A. Wingate, High-resolution modeling of indirectly driven high-convergence layered inertial confinement fusion capsule implosions, Physics of Plasmas 24 (2017) 052701. doi:10.1063/1.4981222.

[16] J. P. Sauppe, B. M. Haines, S. Palaniyappan, P. A. Bradley, S. H. Batha, E. N. Loomis, J. L. Kline, Modeling of direct-drive cylindrical implosion experiments with an Eulerian radiation-hydrodynamics code, Physics of Plasmas 26 (2019) 042701. doi:10.1063/1.5083851.

[17] P. Chang, G. Fiksel, M. Hohenberger, J. Knauer, R. Betti, F. Marshall, D. Meyerhofer, F. Séguin, R. Petrasso, Fusion yield enhancement in magnetized laser-driven implosions, Physical review letters 107 (2011) 035006.

[18] R. Betti, K. Anderson, V. N. Goncharov, R. L. McCrory, D. D. Meyerhofer, S. Skupsky, R. P. J. Town, Deceleration phase of inertial confinement fusion implosions, Physics of Plasmas 9 (2002) 2277–2286. doi:10.1063/1.1459458.

[19] A. Bose, K. M. Woo, R. Nora, R. Betti, Hydrodynamic scaling of the deceleration-phase Rayleigh-Taylor instability, Physics of Plasmas 22 (2015) 072702. doi:10.1063/1.4923438.

[20] J. P. Sauppe, S. Palaniyappan, E. N. Loomis, J. L. Kline, K. A. Flippo, B. Srinivasan, Using cylindrical implosions to investigate hydrodynamic instabilities in convergent geometry, Matter and Radiation at Extremes 4 (2019) 065403.

[21] J. P. Sauppe, S. Palaniyappan, J. L. Kline, K. A. Flippo, O. Landen, D. Shvarts, S. H. Batha, P. A. Bradley, E. N. Loomis, B. J. Tobias, et al., Design of cylindrical implosion experiments to demonstrate scale-invariant Rayleigh-Taylor instability growth, High Energy Density Physics 36 (2020) 100831.

[22] J. P. Sauppe, S. Palaniyappan, B. J. Tobias, J. L. Kline, K. A. Flippo, O. Landen, D. Shvarts, S. H. Batha, P. A. Bradley, E. N. Loomis, et al., Demonstration of scale-invariant Rayleigh-Taylor instability growth in laser-driven cylindrical implosion Experiments, Physical Review Letters 124 (2020) 185003.

[23] S. Palaniyappan, J. Sauppe, B. Tobias, C. Kawaguchi, K. Flippo, A. Zylstra, O. Landen, D. Shvarts, E. Malka, S. Batha, et al., Hydro-scaling of direct-drive cylindrical implosions at the OMEGA and the National Ignition Facility, Physics of Plasmas 27 (2020) 042708.

[24] W. W. Hsing, C. W. Barnes, J. B. Beck, N. M. Hoffman, D. Galmiche, A. Richard, J. Edwards, P. Graham, S. Rothman, B. Thomas, Rayleigh-taylor instability evolution in ablatively driven cylindrical implosions, Physics of Plasmas 4 (1997) 1832–1840. doi:10.1063/1.872326.

[25] C. C. Kuranz, R. P. Drake, M. J. Grosskopf, B. Fryxell, A. Budde, J. F. Hansen, A. R. Miles, T. Plewa, N. Hearn, J. Knauer, Spike morphology in blast-wave-driven instability experiments, Physics of Plasmas 17 (2010) 052709. doi:10.1063/1.3389135.

[26] C. C. Kuranz, R. P. Drake, M. J. Grosskopf, A. Budde, C. Krauland, D. C. Marion, A. J. Visco, J. R. Ditmar, H. F. Robey, B. A. Remington, A. R. Miles, A. B. R. Cooper, C. Sorce, T. Plewa, N. C. Hearn, K. L. Killebrew, J. P. Knauer, D. Arnett, T. Donajkowski, Three-dimensional blast-wave-driven rayleighâtaylor instability and the effects of long-wavelength modes, Physics of Plasmas 16 (2009) 056310. doi:10.1063/1.3099320.

[27] B. A. Remington, S. V. Weber, M. M. Marinak, S. W. Haan, J. D. Kilkenny, R. J. Wallace, G. Dimonte, Single-mode and multimode rayleigh-taylor experiments on nova, Physics of Plasmas 2 (1995) 241–255. doi:10.1063/1.871096.

[28] B. A. Remington, H.-S. Park, D. T. Casey, R. M. Cavallo, D. S. Clark, C. M. Huntington, C. C. Kuranz, A. R. Miles, S. R. Nagel, K. S. Raman, V. A. Smalyuk, Rayleigh–taylor instabilities in high-energy density settings on the national ignition facility, Proceedings of the National Academy of Sciences 116

(2019) 18233–18238. doi:10.1073/pnas.1717236115.

[29] R. P. Drake, D. R. Leibrandt, E. C. Harding, C. C. Kuranz, M. A. Blackburn, H. F. Robey, B. A. Remington, M. J. Edwards, A. R. Miles, T. S. Perry, R. J. Wallace, H. Louis, J. P. Knauer, D. Arnett, Nonlinear mixing behavior of the three-dimensional rayleigh-taylor instability at a decelerating interface, Physics of Plasmas 11 (2004) 2829–2837. doi:10.1063/1.1651492.

[30] N. C. Swisher, C. C. Kuranz, D. Arnett, O. Hurricane, B. A. Remington, H. F. Robey, S. I. Abarzhi, Rayleigh-taylor mixing in supernova experiments, Physics of Plasmas 22 (2015) 102707. doi:10.1063/1.4931927.

[31] M. J.-E. Manuel, M. Flaig, T. Plewa, C. K. Li, F. H. SÃ©guin, J. A. Frenje, D. T. Casey, R. D. Petrasso, S. X. Hu, R. Betti, J. Hager, D. D. Meyerhofer, V. Smalyuk, Collisional effects on rayleigh-taylor-induced magnetic fields, Physics of Plasmas 22 (2015) 056305. doi:10.1063/1.4919392.

[32] M. Flaig, T. Plewa, Self-generated magnetic fields in blast-wave driven rayleigh-taylor experiments, High Energy Density Physics 17 (2015) 46–51. URL: https://www.sciencedirect.com/science/article/pii/S1574181815000075. doi:https://doi.org/10.1016/j.hedp.2015.01.005, 10th International Conference on High Energy Density Laboratory Astrophysics.

[33] M. Flaig, T. Plewa, P. A. Keiter, R. P. Drake, M. Grosskopf, C. Kuranz, H.-S. Park, Design of a supernova-relevant rayleigh-taylor experiment on the national ignition facility. i. planar target design and diagnostics, High Energy Density Physics 12 (2014) 35–45. URL: https://www.sciencedirect.com/science/article/pii/S1574181814000408. doi:https://doi.org/10.1016/j.hedp.2014.06.003.

[34] B. Fryxell, C. Kuranz, R. Drake, M. Grosskopf, A. Budde, T. Plewa, N. Hearn, J. Hansen, A. Miles, J. Knauer, The possible effects of magnetic fields on laser experiments of rayleigh-taylor instabilities, High Energy Density Physics 6 (2010) 162–165. doi:https://doi.org/10.1016/j.hedp.2010.01.008, iCHED 2009 - 2nd International Conference on High Energy Density Physics.

[35] S. A. Slutz, M. C. Herrmann, R. A. Vesey, A. B. Sefkow, D. B. Sinars, D. C. Rovang, K. J. Peterson, M. E. Cuneo, Pulsed-power-driven cylindrical liner implosions of laser preheated fuel magnetized with an axial field, Physics of Plasmas 17 (2010) 056303. doi:10.1063/1.3333505.

[36] E. Harris, Rayleigh-taylor instabilities of a collapsing cylindrical shell in a magnetic field, The Physics of Fluids 5 (1962) 1057–1062.

[37] D. Sinars, S. Slutz, M. Herrmann, R. McBride, M. Cuneo, K. Peterson, R. Vesey, C. Nakhleh, B. Blue, K. Killebrew, et al., Measurements of magneto-rayleigh-taylor instability growth during the implosion of initially solid al tubes driven by the 20-ma, 100-ns z facility, Physical review letters 105 (2010) 185001.

[38] D. Ryutov, T. Awe, S. Hansen, R. McBride, K. Peterson, D. Sinars, S. Slutz, Effect of axial magnetic flux compression on the magnetic rayleigh-taylor instability (theory), in: AIP Conference Proceedings, volume 1639, American Institute of Physics, 2014, pp. 63–66.

[39] T. Awe, R. McBride, C. Jennings, D. Lamppa, M. Martin, D. Rovang, S. Slutz, M. Cuneo, A. Owen, D. Sinars, et al., Observations of modified three-dimensional instability structure for imploding z-pinch liners that are premagnetized with an axial field, Physical review letters 111 (2013) 235005.

[40] B.-I. Jun, M. L. Norman, J. M. Stone, A numerical study of Rayleigh-Taylor instability in magnetic fluids, The Astrophysical Journal 453 (1995) 332.

[41] B. K. Shivamoggi, Rayleigh-taylor instability of a compressible plasma in a horizontal magnetic field, Zeitschrift für angewandte Mathematik und Physik ZAMP 33 (1982) 693–697.

[42] D. L. Tubbs, C. W. Barnes, J. B. Beck, N. M. Hoffman, J. A. Oertel, R. G. Watt, T. Boehly, D. Bradley, P. Jaanimagi, J. Knauer, Cylindrical implosion experiments using laser direct drive, Physics of Plasmas 6 (1999) 2095–2104. doi:10.1063/1.873462.

[43] J. R. Fincke, N. E. Lanier, S. H. Batha, R. M. Hueckstaedt, G. R. Magelssen, S. D. Rothman, K. W. Parker, C. J. Horsfield, Postponement of Saturation of the Richtmyer-Meshkov Instability in a Convergent Geometry, Phys. Rev. Lett. 93 (2004) 115003.

[44] N. E. Lanier, G. R. Magelssen, S. H. Batha, J. R. Fincke, C. J. Horsfield, K. W. Parker, S. D. Rothman, Validation of the radiation hydrocode RAGE against defect-driven mix experiments in a compressible, convergent, and miscible plasma system, Physics of Plasmas 13 (2006) 042703. doi:10.1063/1.2192502.

[45] T. Boehly, D. Brown, R. Craxton, R. Keck, J. Knauer, J. Kelly, T. Kessler, S. Kumpan, S. Loucks, S. Letzring, F. Marshall, R. McCrory, S. Morse, W. Seka, J. Soures, C. Verdon, Initial performance results of the OMEGA laser system, Optics Communications 133 (1997) 495–506. doi:https://doi.org/10.1016/S0030-4018(96)00325-2.

[46] E. I. Moses, Ignition on the National Ignition Facility: a path towards inertial fusion energy, Nuclear Fusion 49 (2009) 104022. doi:10.1088/0029-5515/49/10/104022.

[47] B. Fryxell, K. Olson, P. Ricker, F. Timmes, M. Zingale, D. Lamb, P. MacNeice, R. Rosner, J. Truran, H. Tufo, FLASH: An adaptive mesh hydrodynamics code for modeling astrophysical thermonuclear flashes, The Astrophysical Journal Supplement Series 131 (2000) 273.

[48] P. Tzeferacos, M. Fatenejad, N. Flocke, C. Graziani, G. Gregori, D. Lamb, D. Lee, J. Meinecke, A. Scopatz, K. Weide, FLASH MHD simulations of experiments that study shock-generated magnetic fields, High Energy Density Physics 17 (2015) 24–31. URL: https://www.sciencedirect.com/science/article/pii/S1574181814000779. doi:https://doi.org/10.1016/j.hedp.2014.11.003, 10th International Conference on High Energy Density Laboratory Astrophysics.

[49] FLASH User's Guide, ????

[50] L. Spitzer, Physics of fully ionized gases, Courier Corporation, 2006.

Chapter 3

A Magnetized Experimental and Computational Study of Thin-Layer Rayleigh-Taylor Instability Development During Deceleration

The process of designing a target for an experimental platform happens in many stages and includes multiple design iterations. In this section, the evolution of the experimental target design process, based on the initial thin-layer RTI target design presented in Samulski 2021 [1], is explored. The experimental results from this design process are presented in the two papers presented in Section 3.2 and 4. The computational basis of the experimental platform designed for the Omega-EP laser is described Chapter 2; however, the steps from transitioning a computationally designed target to a a fully realized experimental platform requires several rounds of design modifications based on target manufacturing constraints as well as initial experimental data.

3.1 Experimental Design Process

The experimental design for studying deceleration-stage RTI on Omega-EP with and without an externally applied magnetic field consists of a single-feature perturbation rather than a sinusoidal perturbation. The single-feature perturbation is chosen for being the seed mechanism from which thin-layer RTI can evolve in a rapidly nonlinear manner. Consequently, the potential for the externally applied magnetic field to impact the RTI evolution early-in-time allows for these effects to be observed experimentally. The first iteration of the target design is chosen to observe the difference in RTI evolution with changing divot perturbations. A schematic for this initial configuration can be seen in Figure 3.1.

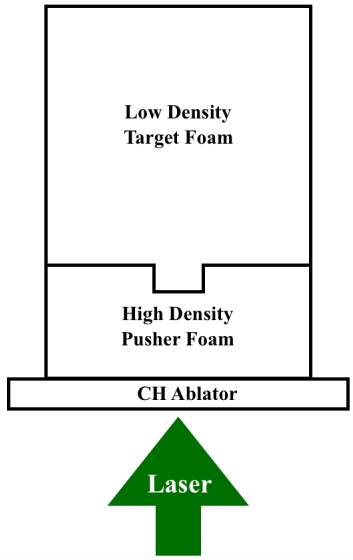

Figure 3.1: A schematic of the direct-drive shock-tube target designed for studying deceleration-stage thin-layer RTI on Omega-EP.

This initial target configuration consists of a 10 µm thick CH ablator at 1.0 g cm^{-3} on which

a shock-tube is attached. Within the shock-tube a high density foam of nickel-doped carbon (NiCRF), at a density of $0.215\,\mathrm{g\,cm^{-3}}$ and thickness of 300 µm, is adhered to the ablator. The remainder of the shock-tube is filled with a low density, $0.024\,\mathrm{g\,cm^{-3}}$, CH foam. There is either a 55 µm wide by 100 µm deep divot or a 55 µm wide by 200 µm deep divot set into the NiCRF surface that abuts the low density CH foam, which acts as the perturbation seeding the RTI. The change in divot depth is intended to capture two types of perturbations that seed thin-layer RTI, voids and a fill-tube-adjacent perturbation [2, 3, 4, 5, 6]. The target is driven by a 2 ns 2200 J laser pulse on a 400 µm spot on the ablator.

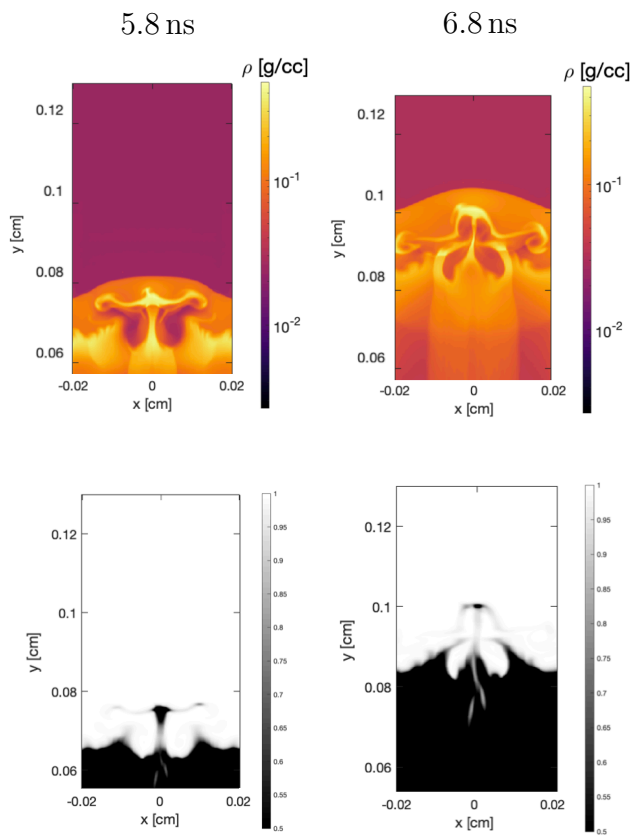

Figure 3.2: The top row consists of density plots of the RTI evolution seeded by the 55 μm wide by 100 μm deep divot at 5.8 ns and 6.8 ns. The second row is the corresponding synthetic x-ray radiographs of the density plots at the same timings.

Figure 3.2 shows density plots and their corresponding synthetic x-ray radiographs, Appendix A, of the 55 µm by 100 µm case simulated in 2D using FLASH. As can be seen in the density plots, the thin-layer RTI consists of a central spike with two arms extending horizontally from the sides of the spike. As the RTI evolves from 5.8 ns to 6.8 ns the RTI spike grows in size, and the arms appear to be falling back behind the spike cap towards the interface. Comparatively, Figure 3.3 shows the density plots and synthetic x-ray radiographs at the

same timings for the 55 µm by 200 µm divot case. As can be seen in both the density plots and the synthetic x-ray radiographs, the RTI evolution appear significantly more jet-like, with a low density central jet and globular regions with high-density material concentrations.

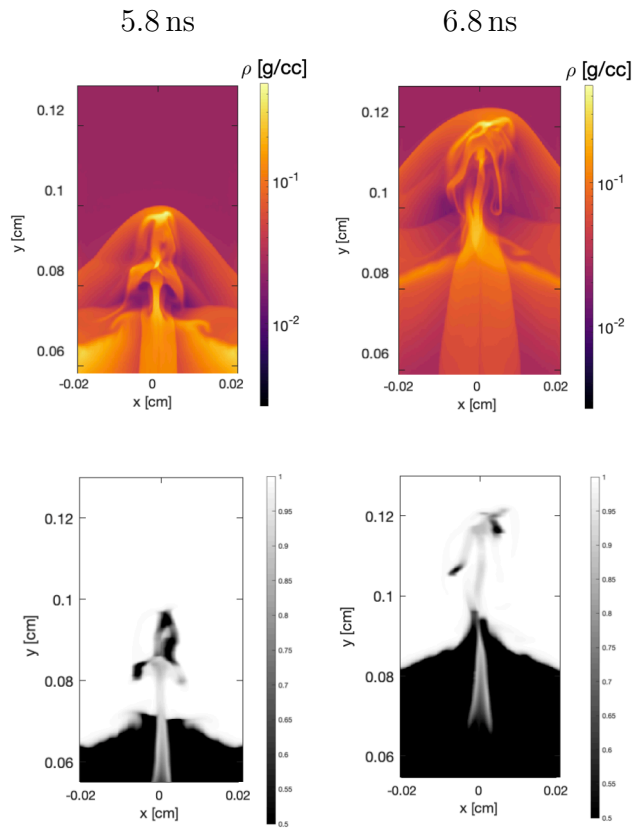

Figure 3.3: Density plots at 5.8 ns and 6.8 ns of the 55 μm wide by 200 μm deep divot seeded RTI evolution, with the corresponding synthetic x-ray radiographs in the second row.

Referring back to the thin-layer RTI evolution prediction by Ott [7] in Figure 1.6, the morphology of the 55 µm by 100 µm divot case more closely resembles the theoretical thin-layer RTI evolution. As a result of the similarity of the 55 µm by 100 µm divot case to the theory in Ott's 1972 paper [7], and in addition to manufacturing constraints on the realistically machinable depth of the divot with respect to the thickness of the NiCRF foam, only the 55 µm by 100 µm case is chosen for the first experimental day on Omega-EP. This first experimental day is intended to refine the target design and diagnostic setup for a second experimental day during which the externally applied magnetic field will be fielded.

Data from the first experimental day is seen in Figure 3.4, and shows that early in time, at 3 ns, the NiCRF has high enough density for the opacity to be significant enough for the interface to be visible, but at 8 ns the NiCRF has diffused to such a point that the material opacity is hardly distinguishable from the background noise. While a thin curved front with

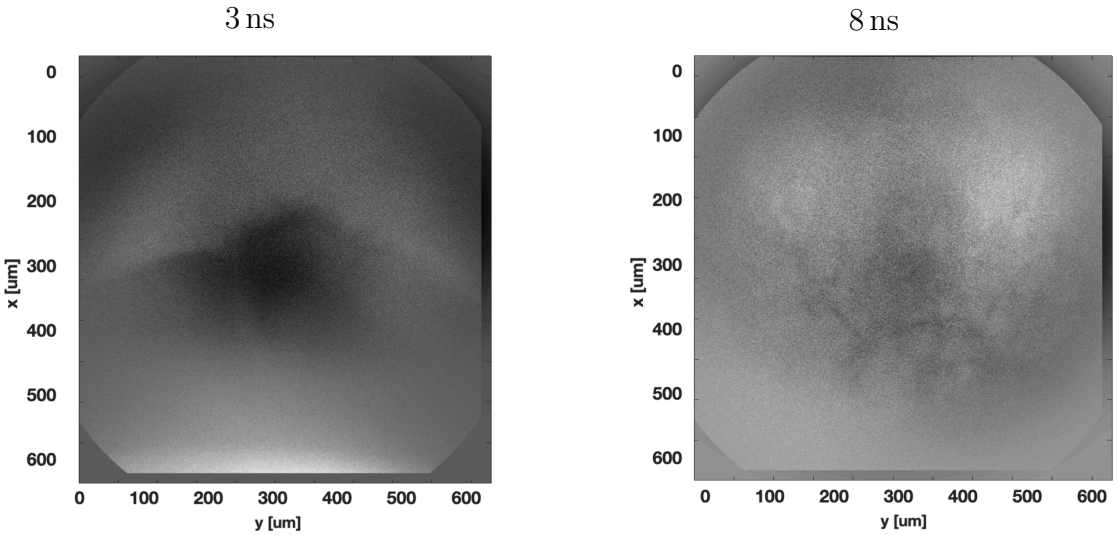

Figure 3.4: X-ray radiographs of experimental data using FZP as the focusing diagnostic at 3 ns and 8 ns

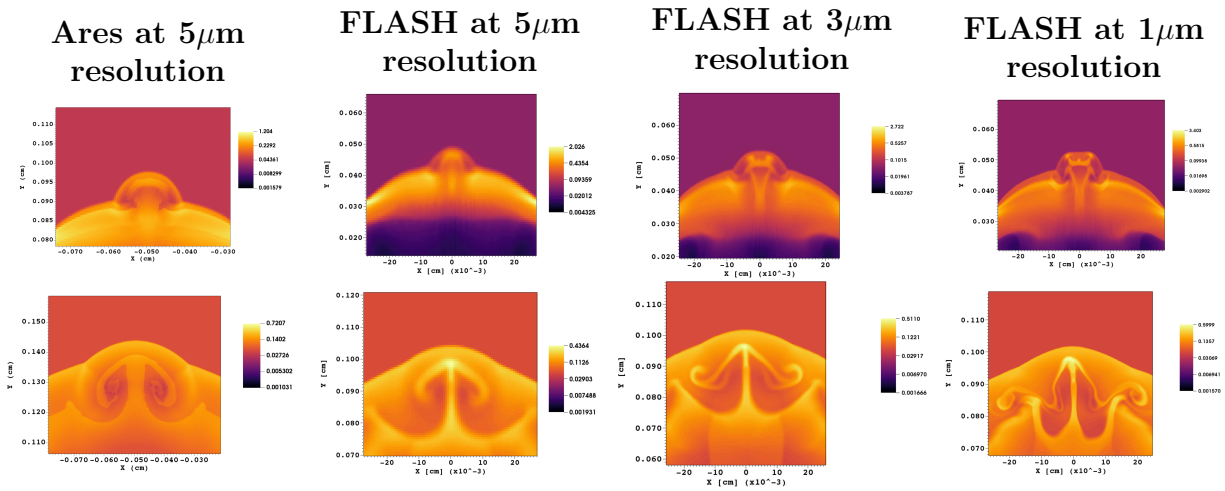

Figure 3.5: Density [g/cc] plots of the 55 µm wide by 100 µm deep divot where the first column corresponds to Ares simulations with 5 µm resolution, and the other columns are FLASH simulations at 5 µm, 3 µm, and 1 µm resolution. The top row corresponds a 3 ns timing and the second row has a timing of 8 ns.

a possible arm extending to the left may be present in the data, it cannot be confirmed in a meaningful way. Figure 3.5 shows a mesh resolution case study using FLASH and Ares to demonstrate the approximate Fresnel Zone Plate (FZP) resolution as compared to simulations at 5 µm, 3 µm, and 1 µm resolution. FZP is a focusing diagnostic using concentric rings to provides diffraction limited imaging resolutions, where the resolution limit is based on 1.22 times the width of the outermost zone [8, 9, 10, 11, 12, 13]. As a result of the mesh

resolution study, it can be determined that the FZP data resolution is at best 5 µm when comparing the mesh study in Figure 3.5 to the data at 3 ns in Figure 3.4. Interestingly, the low resolutions tests did not seed the same small scale features that develop the double RTI arm morphology seen in the thin-layer case and possibly as observed at 8 ns in the data. The target design used in the first experimental day is redesigned to improve on the late-in-time image contrast issues that arose during the first experimental day in order to achieve better late-in-time data.

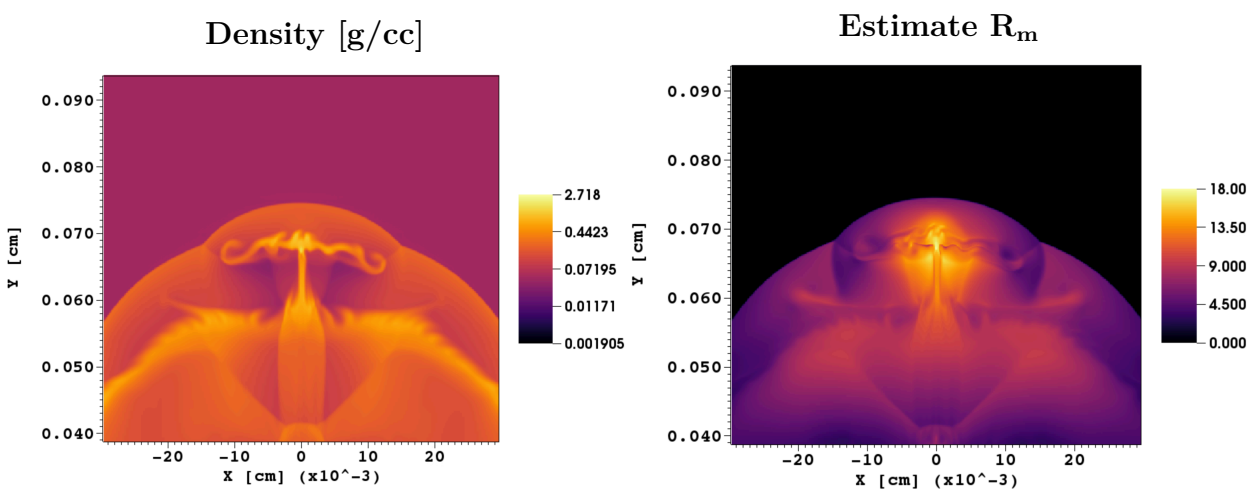

Figure 3.6: A density plot of thin-layer RTI development at 6 ns in a 0 T HD FLASH simulation using tantala as the high density pusher material. The estimated magnetic Reynolds number, (R_m), is shown using the divot depth of 100 μm as the scale length.

Using the setup from the first experimental day as a baseline for development, the target design is updated for the second magnetized experimental day. The primary change consists of switching to a tantalum pentoxide foam, tantala, from the NiCRF, intending to improve the contrast issues encountered in x-ray radiographs of the first experimental day. Figure 3.6 shows that the RTI evolution remains similar when the high density material is shifted to using a 0.245 g cm^{-3} dense tantala foam, but the estimated magnetic Reynolds numbers, (R_m) only reaches an estimated 18 at the center of the RTI spike. This is crucial given that R_m, the ratio of fluid advection to magnetic diffusion, must be significantly larger than 1 for a plasma to be within a regime where a magnetic field would have a measurable impact on the RTI growth.

Achieving higher temperatures and subsequently higher R_m are necessary considerations for the target design for the second experimental day. These changes could come in the form of adjusting the high density pusher foam thickness, changing the divot dimensions, or even changing the density of the tantala foam used as the high density pusher. Ultimately the thickness of the tantala foam is adjusted to be 150 µm thick, with a density of approximately 0.240 g cm^{-3} and the divot dimensions of 55 µm by 100 µm held consistent for the second experimental day. The results for this target design and the second experimental day are

discussed in detail in the peer-reviewed publications presented in Section 3.2 and Chapter 4.

3.2 An Experimental and Computational Study of Thin-Layer Rayleigh-Taylor Instability Development During Deceleration with and without an Externally Applied Magnetic Field

An Experimental and Computational Study of Thin-Layer Rayleigh-Taylor Instability Development During Deceleration with and without an Externally Applied Magnetic Field

C. Samulski[a,d], M. J.-E. Manuel[c], J. Kline[d], P. Nilson[e], B. Srinivasan[b]

[a] *Virginia Polytechnic Institute and State University, Blacksburg, VA 24060, USA*
[b] *University of Washington, Seattle, WA 98195, USA*
[c] *General Atomics, San Diego, CA 92121, USA*
[d] *Los Alamos National Laboratory, P.O. Box 1663, Los Alamos, New Mexico 87545, USA*
[e] *Laboratory for Laser Energetics, Rochester, New York 14623, USA*

Abstract

The importance of mitigating the Rayleigh-Taylor instability (RTI) in inertial confinement fusion (ICF) is critical to successfully achieve high gain fusion yield. Consequently, understanding the seed mechanisms of RTI and the potential evolution of RTI in ICF relevant conditions is crucial. Single feature perturbations consistently demonstrate non-linear RTI evolution, for which an experimental platform on OMEGA-EP is developed. Manufacturing defects introduced into the target design require exploration of unanticipated changes to RTI development and an identification of targets that will still render quantifiable physics results. Consequently, it is presented that the inherent 3D nature of experimental targets necessitates 3D modeling for accurate design work and predictive modeling of experimental targets, especially when high resolution imaging diagnostics, like Fresnel Zone Plates (FZP), are utilized. A study of the morphology of the RTI evolution due to changing initial conditions and the presence of an externally applied magnetic field are also explored. Experimental data shows thin-layer RTI morphology comparable to resistive magneto hydrodynamic (MHD) 3D results. A discussion on the impacts of an externally applied magnetic field makes the case for continued efforts to observe a magnetic field's impact on RTI morphology.

1. Introduction

Isolated features, such as fill tubes and voids, can negatively impact inertial confinement fusion implosions by seeding instability growth during the deceleration phase [1, 2, 3, 4]. Mitigating the instability growth seeded by these features is pivotal in improving capsule performance. Several studies [5, 6, 1] of surrogate perturbations in place of fill-tubes and high fidelity fill-tube model perturbations demonstrate mixing and convergence reduction in ICF capsules. Material mixing and convergence disruptions are observable in all fill-tube configurations that have been modeled, including the recent reduced-size fill tube [7, 8]. The surrogate fill tube causes a degradation in the hot-spot ion temperature of 67% and a yield degradation of 17% [9]. However, little work has been performed in using a background magnetic field to mitigate the Rayleigh-Taylor instability (RTI) as driven by isolated features.

RTI is theorized to rapidly develop to the nonlinear stage in thin-layer configurations [10]. The thin-layer approximation, wherein a perturbation's wavelength is longer than the density layer is thick, has been shown to produce nonlinear RTI growth and may well represent such isolated features in ICF capsules [11]. A single feature perturbation will seed RTI as the fluid layers collide. This subsequently forms a downward vertical layer, that falls under the influence of gravity, and an upward jet of fluid, which will splay outward before also falling back down under the gravitational influence. Knowing the impact of magnetic fields on single-mode RTI configurations during linear growth, treating an isolated perturbation using this thin-layer approximation allows for a potential experimental exploration of the idea that a background magnetic field may have a mitigating impact on the thin-layer RTI.

RTI has been studied extensively [12] in ablative acceleration cases, however study of RTI growth during the deceleration stage of ICF conditions is less explored [13, 14, 15]. Specifically, the study of planar blast-wave driven RTI has predominately been focused on astrophysical applications [16, 17, 18, 19, 20, 21], where magnetization of the RTI is sourced by self-generated fields. The presence of a seed magnetic field in an ICF capsule can relax the ignition criterion due to enhanced confinement time and can reduce thermal conduction away from the hot-spot [22, 23]. The first magnetized experiments, conducted at Omega [24], demonstrated an increase in the hot-spot ion temperature

*Camille Samulski
Email addresses: csamulski@vt.edu (C. Samulski), manuelm@fusion.gat.com (M. J.-E. Manuel), jkline@lanl.gov (J. Kline), philip.nilson1@gmail.com (P. Nilson), srinbhu@uw.edu (B. Srinivasan)

and neutron yield by 15% and 30%, respectively.

Magnetic fields are predicted to impact RTI morphology in nonlinear evolution. The study of magnetic field effects on RTI growth and Kelvin-Helmholtz instability (KHI) has been numerically investigated in 2D geometry [12]. The magnetic field suppresses short-wavelength modes and secondary KHI growth when perpendicular to the perturbation wave vector; however, there is little impact shown on instability growth in 2D simulations when the field is parallel to this plane. Additional numerical studies, like the ones found in Ref. [22], have studied the impact magnetic fields have on instabilities seeded by target imperfections, i.e., voids, divots, or surface roughness, on the interior of ICF capsules at deceleration. The study in Ref. [22] also predicts effective mitigation of short-wavelength RTI growth and the relaxation of ignition criteria for ICF. Experimental studies are only now beginning to validate these numerical predictions, all in the context of a wavelength that is short compared to the dense-layer thickness. Consequently, the examination of the effects of externally applied magnetic fields on thin-layer-RTI conditions remains to be understood.

The following work presents a novel experimental platform to study deceleration-stage thin-layer-RTI in a planar blast-wave driven configuration on Omega-EP. The experimental platform design is done in 2D utilizing Ares' [25] advanced magnetohydrodynamic (MHD) equations, laser deposition, radiation, diffusion, thermal conduction and equation of state (EOS) capabilities. The design presents an experimental platform where discernible differences between unmagnetized and magnetized RTI growth are observable using the high-resolution diagnostic discussed in section 2. However, defects in the target can impact the physics conclusions substantially, so quantifying the impact of target fabrication defects is necessary to understand the findings of the experimental study. Additionally, results from this study show that despite the 2D nature of the perturbation, the evolution is in fact 3D, and post-experiment 3D Ares simulations show different behavior than what is predicted by 2D design simulations.

The paper is structured with section 2 elaborating on the experimental setup and target design for Omega-EP and the anticipated observable RTI evolution. Sections 3.1 and 3.2 present computational studies of the impacts of manufacturing defects in the targets on the RTI evolution. Sections 4 and 5 present the experimental data and 3D Ares simulations validated by data and expected experimental results as originally designed in section 2. The key contributions of the paper are a demonstration of a viable experimental platform on Omega-EP for studying deceleration-stage thin-layer-RTI with and without an externally applied magnetic field. Additionally, validation of computational modeling in Ares for experimental data, as well as a commentary on the necessity for 3D modeling to best benchmark experimental data is presented.

2. Experimental Setup and Design

This experiment is designed with the intention to observe RTI morphology seeded by a single-feature perturbation with and without the presence of a background magnetic field. An unstable foam-foam interface in a shock-tube has previously been used to benchmark the laser drive on OMEGA-EP, however the detailed morphology of RTI is not observed [26] due to low image resolution and the chosen image timing being under-predicted by simulations during the platform design-stage. This timing issue is resolved by using a benchmarked laser drive for more accurate timing predications. The resolution issue is addressed by shifting from using pin-hole x-ray radiography to Fresnel Zone Plates (FZP) [27, 28, 29] as the primary imaging diagnostic, which have the capability to reach an image resolution of approximately 2 µm.

The designed experimental configuration consists of a shock-tube mounted on a 10 µm, 1.0 g cm^{-3}, 3% Silicon-doped CH ablator. Within the shock-tube and glued to the ablator is a 0.245 g cm^{-3} high density tantalum pentoxide foam, tantala. The tantala has a thickness of 150 µm with a central channel measuring 55 µm wide by 100 µm deep. The channel perturbation abuts a low density CH foam of 0.038 g cm^{-3} in the shock-tube. The physics package is driven by a 2 ns square pulse on a 400 µm spot using the 400 µm phase-plates at OMEGA-EP, giving an intensity of $\sim 1.7 \times 10^{15}$ W/cm^2. A detailed schematic of the physics package can be seen in figure 1.

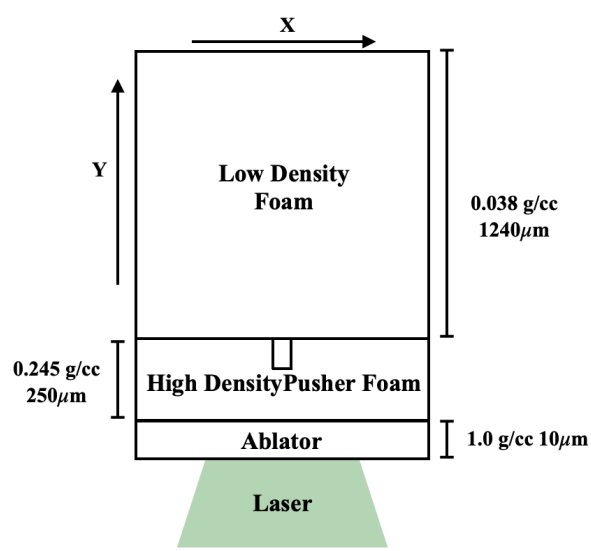

Figure 1: A schematic of the experimental design for studying single-feature perturbation RTI with and without background magnetic fields. The targets comprise of a shock-tube with a solid density ablator, a high density tantala foam with a 55 µm by 100 µm perturbation, and a low density foam. The targets are driven by a square 2 ns laser pulse of approximately 4200 J.

The experimental design also consists of an titanium foil for a He-α backlighter driven by two beams on OMEGA-EP for 100 ps at 100 J per beam using the 750 µm diameter

phase plates, I$\sim 4 \times 10^{14}$ W/cm^2. The FZP diagnostic is coupled to the X-ray CCD, and the imaging geometry places the FZP 84 mm from the physics package and 3.56 m from the x-ray CCD. This geometry has been shown to provide ~3 µm spatial resolution of deceleration-phase RTI [29]. The proposed work combines this diagnostic platform with the addition of Omega-EP's dual magneto-inertial fusion electrical discharge system (MIFEDS) to provide a 23 T magnetic field oriented parallel to the direction of the shock propagation.

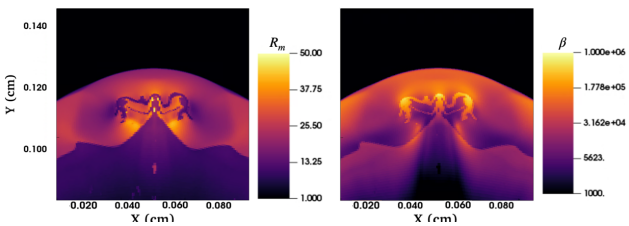

Figure 2: Plots at 5 ns of the magnetic Reynolds number, on the left, and β value, on the right, of the 23 T resistive MHD 2D Ares simulation.

2D Ares simulations are used to show the RTI evolution at varying times, in order to predict the expected differences in thin-layer RTI growth with and without a 23 T externally applied magnetic field, and the target design described prior is chosen because it provides plasma conditions in which the applied magnetic field is predicted to have an effect on the RTI morphology. Plasma regimes similar to those in Ref. [15] are used for determining the necessary plasma conditions for which an externally applied magnetic field will have an observable impact on RTI growth and morphology. Specifically, using the magnetic Reynolds number (R_m), the ratio of fluid advection to magnetic diffusion, and the plasma β, the ratio of the dynamic pressure to magnetic pressure, as metrics for which a magnetic field will have a measurable effect on the RTI, figure 2 predicts that the desired plasma regime is achievable. To illustrate, the magnetic Reynolds number needs to be sufficiently larger than one in order for an magnetic field to have observable effects on the RTI morphology, and as can be seen in figure 2 there are plasma regions around the RTI where the magnetic Reynolds number reaches 50. Furthermore, in figure 2 the plasma β is much larger than 1, thus extended MHD effects, such as the hall term, are unlikely to play an influential role on the RTI evolution. Comparing a 23 T magnetized resistive-MHD case with an unmagnetized case in figure 2 highlights the differing morphology in the RTI even at a 5 µm resolution.

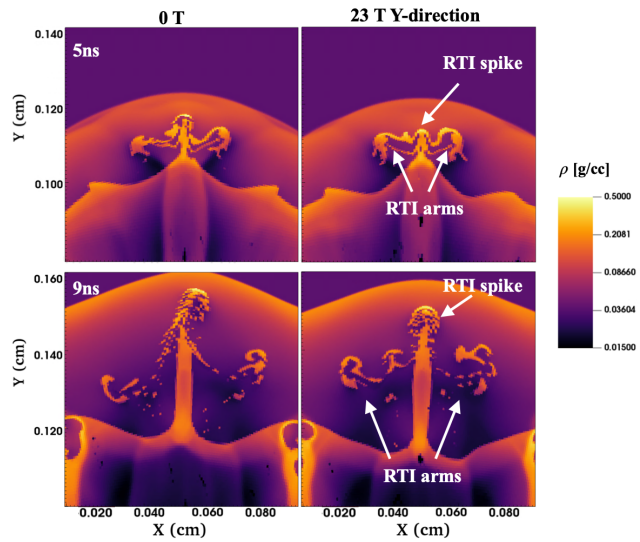

Figure 3: 2D Ares simulations of the target design at 5 ns in the top row and 9 ns in the bottom row. The first column corresponds to a magnetized case and the second column shows the same target with a 23 T externally applied magnetic field.

Figure 3 shows that the thin-layer RTI growth has markedly different morphology than that of RTI resulting from a single mode sinusoidal perturbation. Specifically, as seen in the labels on figure 3, there is a single central RTI spike with arms that extend to the side, in place of a traditional bubble and spike. The unmagnetized simulations show that the arms of the RTI extending to the sides of the central spike begin to disassemble and fall towards the interface, which can be seen in the 9 ns case of figure 3. When the 23 T field is aligned with the direction of the interface propagation, the RTI arms appear to be positioned closer to the top of the central spike at 5 ns, and, while the arms are disassembled by 9 ns, the remnants are further from the interface than in the unmagnetized case. While the difference in morphology appears subtle in the simulations with 5 µm resolution, the macro locations of the spike tips and arms are well within the 3 µm resolution capability of the FZP diagnostic and the small scale morphology is expected to be captured with high fidelity using the FZP.

During the manufacturing process of the physics packages, several defects in the fabrication process arose given the low density and fragility of the foam materials, thus the defects require further investigation to understand and quantify their impact on the RTI. Specifically, a substantial vacuum gap can occur between the high-density-pusher-foam and the low-density-foam, as well as the high-density-pusher-foam lifting from the ablator at an angle within the shock-tube. The potential for these defects to impact experimental results are explored through 2D simulations as follows.

3. Manufacturing Defects

3.1. The Effect of a Vacuum Gap

A vacuum gap is seen occurring at the perturbation interface in most of the post fabrication X-ray radiographs of the targets. A computational study of the impact on the RTI growth and morphology of such a vacuum gap between the high-density-pusher and the low-density-foam is required to predict which targets are still usable to study thin-layer RTI. The simulations are performed using the ARES MHD package. The original experimental design seen in figure 1 is altered to include a gap of varying size as seen in figure 4. The vacuum gap between the two foams is adjusted from 15 µm to 600 µm to account for a range of gaps that were measured in the manufactured targets. Figure 5 presents plots of density at 6 ns using different vacuum gaps, with the top row for unmagnetized cases and the bottom row for the corresponding magnetized cases. The externally applied magnetic field is 23 T and applied in the Y-direction. The cases in Figure 5 correspond to a 15 µm, 50 µm, 100 µm, 200 µm, and 600 µm vacuum gap.

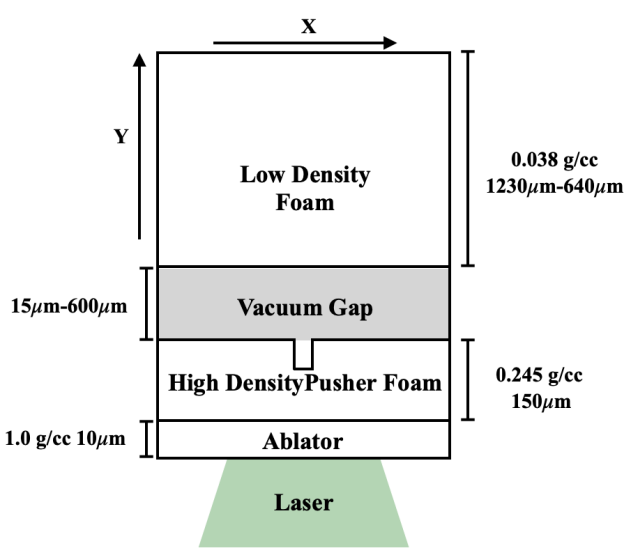

Figure 4: A schematic of the target design for the computational gap study. The vacuum gap between the high density pusher foam and the low density foam vary in size from 15 µm to 600 µm.

As can be seen in the first column of figure 5, a relatively small vacuum gap has little impact on RTI development; however, as the gap increases the RTI morphology is impacted, which is seen even in the RTI morphology of the 50 µm gap case. While the RTI develops and the arms grow in this 50 µm gap case, the spike morphology is significantly different than in the 15 µm case. The smaller gap shows a RTI morphology in which the arms of the RTI appear to be disassembling and there is less material concentrated in the center of the spike, whereas in the 50 µm case there appears to be more concentration of mass in the center of the spike and shorter arms extending to the sides of the central spike.

Notably, the addition of the externally applied magnetic field to both the 15 µm and the 50 µm gap cases preserve the expected RTI morphology more than in the unmagnetized cases. The central spike is present and there is less concentration of the arm's material around the spike with morphology similar to the arms in figure 3. In addition to the observable morphology differences, there is a slight reduction in the propagation distance of the interface in the presence of the magnetic field.

When the vacuum gap is increased to 100 µm the spike morphology from the single feature perturbation is not preserved. As can be seen in the third column of Figure 5, there is an RTI unstable surface, but the expected RTI growth is replaced with a less prominent central RTI spike, and, especially in the magnetized case, significant growth of the arms is observed. The changes in the RTI morphology are exacerbated so significantly in the magnetized case, that it almost appears to be three separate RTI spikes, with the central one being the smallest.

Finally, increasing the gap from 100 µm to 200 µm and 600 µm results in the loss of RTI development seeded by the single feature perturbation, as seen in the fourth and fifth columns of figure 5. The large vacuum gap cases demonstrate growth that is comparable to a flat interface propagating through the low-density-foam, resulting in small-scale features developing. There are no distinct arm or spike features, however the presence of a low density column structure in the wake of the interface is present. Notably, the only impact the externally applied magnetic field has on the larger vacuum gap cases is on the small scale secondary perturbations, which would not be observable in the narrow field of view present in the experiment.

3.2. The Effect of a Tilt

During the target fabrication process, it is identified that the tantala foam does separate from the ablator surface at an angle in at least two targets. The separation will produce a tilt, as shown in figure 6, introducing a vacuum gap above and below the tilted pusher foam. The potential for this deformation of the target setup requires a computational study to ascertain the potential impact such an issue can have on the RTI morphology and overall instability growth. As in the gap study, the simulations were performed using the ARES MHD package. The adjusted initial conditions accounting for the lifted tantala foam can be seen in figure 6. The tantala foam is held in contact with the ablator on the left side of the shock tube, and the right side of the foam is elevated to several varying heights. The size of the tilt of the tantala is chosen based on the measurements of 50 µm and 100 µm from two of the targets, and a range from 10 µm to 300 µm is included to account for best case and worst case conditions. The low density foam is held with a 100 µm gap for all tilts below 100 µm and then the gap between the tantala and low density foam is increased to match the size of the tilt,

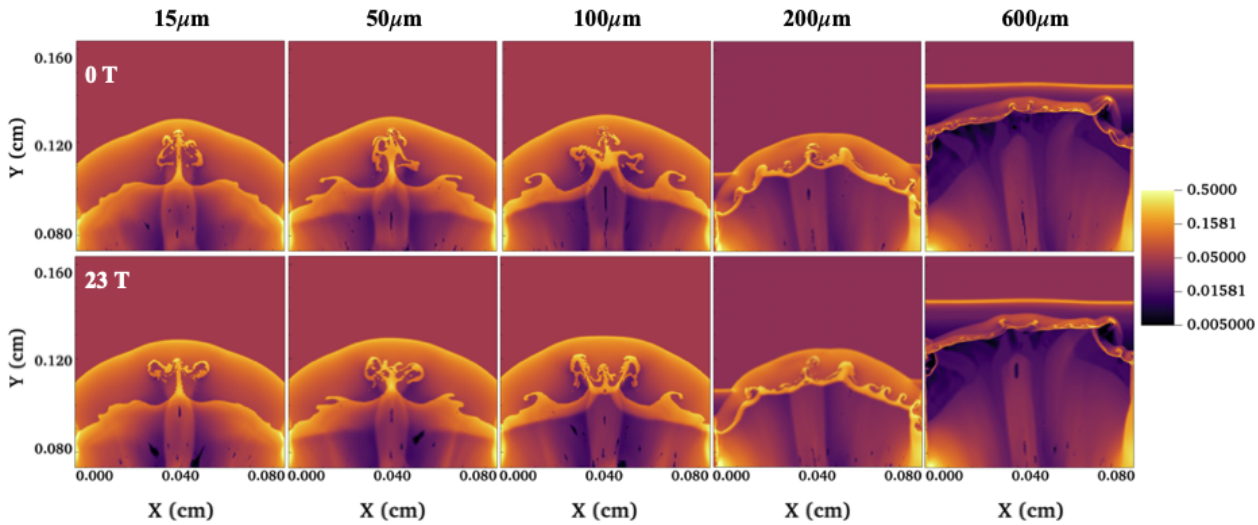

Figure 5: Density plots at 6 ns of simulations with a vacuum gap between the high density and low density foams. The vacuum gaps range ind size from 15 µm to 600 µm, with the top row being unmagnetized and the bottom row the corresponding magnetized cases with a 23 T Y-direction field.

i.e., a tilt of 300 µm had a 300 µm corresponding vacuum gap between the two foams.

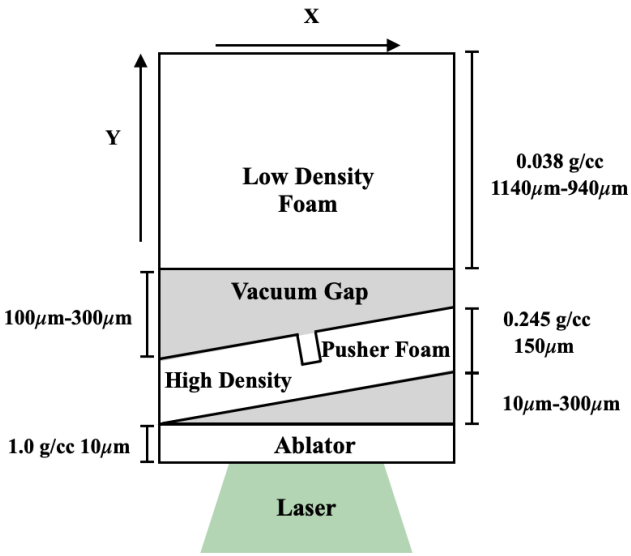

Figure 6: A schematic illustrating the changes from the base experimental target used in the tilted foam study. The position of the left side of the high density foam is held constant, and the gap between the pusher foam and low density foam is adjusted to accommodate the tilt of the high density foam.

Figure 7 illustrates the RTI development in the presence of varying tantala foam tilt heights of 10 µm, 70 µm, 100 µm, 200 µm, and 300 µm. The top row shows unmagnetized cases, and the bottom row implements a background magnetic field of 23 T oriented in the Y-direction. As can be seen in the first two columns of Figure 7, the small tilt in combination with a large vacuum gap results produce degraded RTI development. The central spike and arms are not notably distinct, and while the added magnetic field does distinguish the RTI spike from secondary features in the interface, the spike and arm morphology is not preserved. However, when the size of the tilt corresponds to the size of the vacuum gap, resulting in the tantala foam having a point of contact with the ablator on the left side and the low density foam on the right side of the shock tube, the RTI morphology is significantly less degraded.

Figure 7 shows three cases, 100 µm, 200 µm, and 300 µm where the vacuum gap and the tilt size are equal. In each of these cases the RTI morphology shows a distinct central spike. The RTI spike is at a slight angle owing to the tilt of the tantala which houses the perturbation. While the presence of a background magnetic field does not impact the tilted orientation of the RTI spike, it does change the morphology.

Notably in the 200 µm magnetized case the RTI spike is reduced in height, but the arms are significantly longer than in the unmagnetized case. The 300 µm case results in similar reduction in spike height, though the morphology difference between the magnetized and unmagnetized cases appears on a smaller scale. Lastly, the 100 µm case demonstrates that the presence of the magnetic field concentrates mass in the RTI spike, which appears to be on the cusp of detaching into a spike and bubble. Additionally, there is less horizontal spread of the RTI arms in the presence of a magnetic field. As a result of this study we can presume that the presence of a tilt even on the scale of 300 µm has less impact on RTI morphology and evolution than the size of the gap between the high density tantala foam and low density foam.

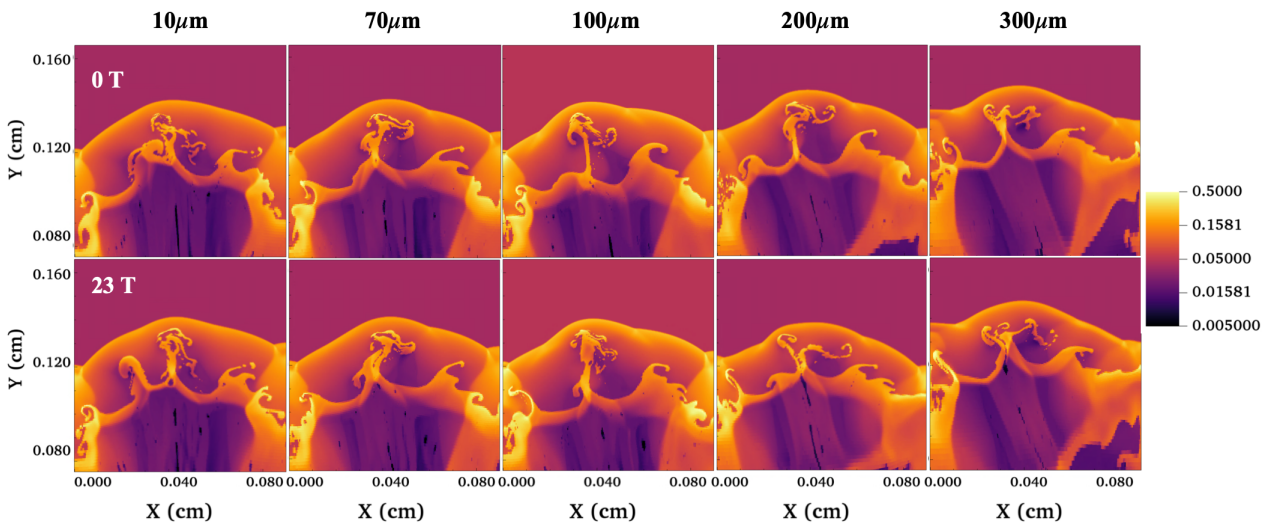

Figure 7: Density plots at 8 ns demonstrating the impact on RTI morphology and development when the high density pusher foam is placed at an angle in the shock tube. The tilts ranged from 10 µm to 300 µm. The cases in the top row are unmagnetized and the bottom row are the corresponding magnetized cases, with an externally applied 23 T field in the Y-direction.

4. Experimental Results

Given the 3D nature of the manufacturing defects in the experimental targets, 3D simulations in Ares are performed to better replicate the potential impact of the imperfections. Additionally, in order to better match the FZP images during the experiment, Hades [30, 31] is used to recreate x-ray radiographs from the 3D Ares simulations. This decision is also made to ensure that any other potential 3D effects, such as the small laser spot size, 400 µm, in comparison to the 900 µm diameter of the experimental target would also be accounted for in our computational validation. Notably, while tracer strips have been shown to eliminate 3D effects in the Z-direction [32], the fragility of the tantala foam and the overall thinness of the material proved to be prohibitive to the inclusion of tracer strips in the experimental design. The complexity of the perturbation interface as shown in figure 8, indicates that not only could the manufacturing defects contribute to issues in resolving the RTI morphology, the distribution of high opacity tantala material varying in both the Z and Y directions will affect the radiograph resolution. The presence of high opacity material spread across both the Z and Y directions indicates that the 3D effects will affect the effective optical depth of the perturbation growth.

Figure 10 shows the FZP image and it's corresponding Hades synthetic x-ray radiographs using a 3D Ares simulation of a target with initial condition on the scale of that seen in target x-ray radiographs prior to the experiment, figure 9. As we can see when compared to the 5 µm resolution in the unaltered synthetic x-ray radiograph in the center left plot, the experimental FZP image on the far left has a lower resolution. Additional simulated x-ray radiographs with Gaussian blurs of 15 µm and 25 µm and 10% artificial noise, are chosen to represent a range of possible resolutions the FZP data could have relative to visible but not fully resolved fiducial. The fiducial, intended to be used for propagation distance benchmarking, is mesh grid with spatial scales of 12 µm. Figure 10 demonstrates that poorer resolution synthetic x-ray radiographs present similar propagation and overall large-scale structure as seen in the FZP data. The low resolution of the data could be attributed to a number of factors, including larger motion blur than anticipated and unpredicted 3D features with the same optical depth as the image plane. Consequently, the FZP image in figure 10 can be used to benchmark the laser drive and glean the general RTI growth and morphology expected. However, the small-scale details which change in the presence of an externally applied magnetic field are not resolvable.

A second experimental image for a 23 T Y-direction magnetic field case can be seen in figure 11 in addition to corresponding simulated x-ray radiographs from Hades using a 3D Ares simulation for a large vacuum gap target setup as seen in the magnetized target radiograph in figure 9. The FZP data shows a domed interface with no observable RTI growth. There is also a possible jet feature propagating ahead of the solid interface, unfortunately the image quality precludes the ability to determine if it is a genuine feature of the target. Magnetized 3D Ares simulations consisting of a 600 µm dome shaped vacuum gap between the tantala and the low density foam account for the domed morphology observed in the FZP data, but not the potential jet feature. Given figure 11 presents the most successful magnetized data, it is unclear if the jet feature is a relevant physics feature or a byproduct of a target defect that has not been accounted for, such as an asymmetric crack in the tantala foam causing an asymmetric shock propagation. Finally, figure 8 shows the necessity of

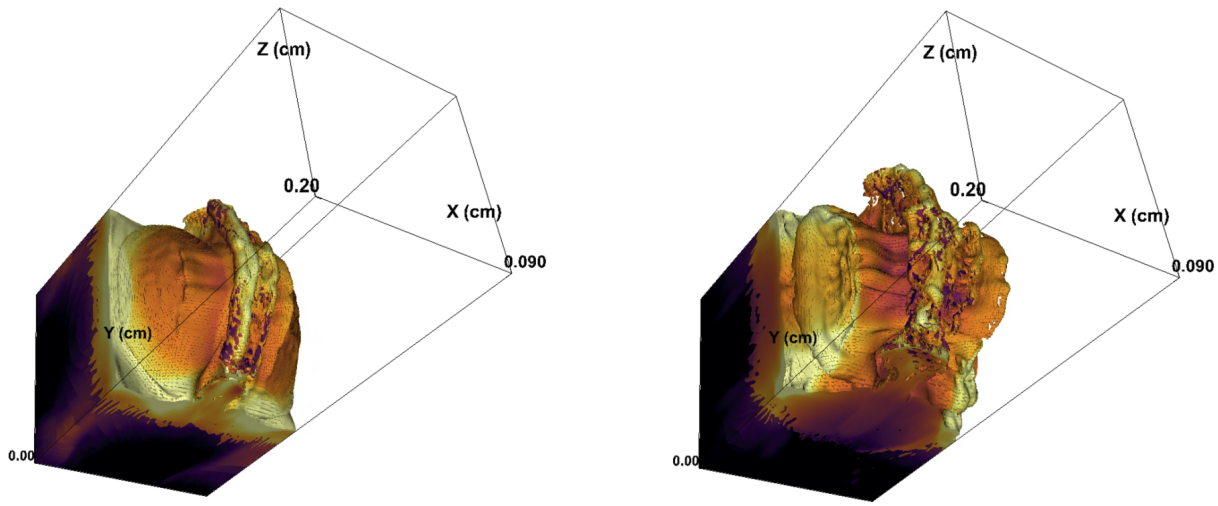

Figure 8: 3D ares simulations at 5 ns, on the right, and 8 ns, on the left, of a 10 µm tilt case run using Ares in 3D. As can be seen at both timings, the 400 µm spot size in relation to the 900 µm shock-tube created a domed propagating interface, causing the high opacity tantala material to be distributed non-uniformly in both the Z and Y direction.

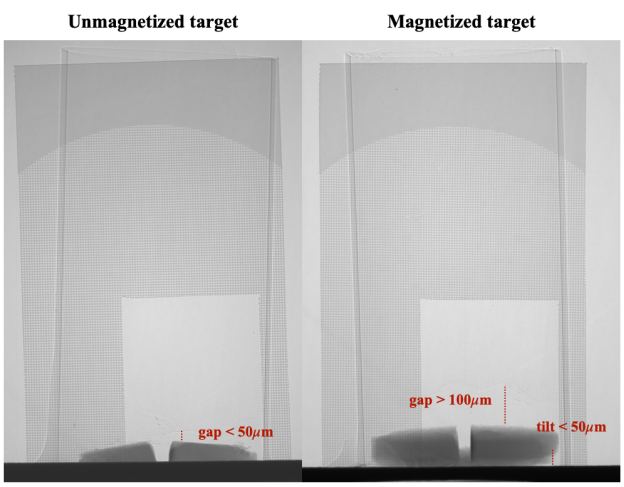

Figure 9: x-ray radiographs of the targets used in the unmagnetized shot, on the left, and the magnetized shot, on the right. The defects are labeled in red, along with their estimated sizes prior to the experiments.

3D simulations to have a clearer picture of what instability growth will look like with realistic 3D targets. These figures demonstrate the potential presence of 3D features and high opacity material spread in both the imaging plane and in the propagation direction causing interference during imaging. Future experiments comparable to these design parameters will benefit from 3D modeling to better predict experimental imaging data.

5. Predicted 3D Computational Results

3D simulations of the target as originally designed in figure 1 provide additional information on the deviation of the experimental results from the predictive 2D simulations seen in figure 3. The experimental data only presents the magnetized case with a 23 T Y-direction externally applied field, however a 23 T X-direction field is also a of potential interest. Figure 12 demonstrates synthetic x-ray radiographs of 3D simulations of the unmagnetized case, the 23 T Y-direction field case, and 23 T X-direction field case at 5 ns and 8 ns.

Simulations are performed at the same 5 µm resolution as used in the 2D simulations, and it is noted that the overall RTI evolution is similar but there are details in morphology that are not captured in 2D. The early time synthetic x-ray radiographs show that the unmagnetized case and the 23 T Y-direction field case are quite similar, but later in time the small scale features between the cases begin to diverge. Specifically, the tilt and width of the RTI spike in the unmagnetized case is larger than in the 23 T Y-direction field case. Additionally, the roll-up of the arm to the right of the central spike is more dense in the 23 T Y-direction field case.

The 23 T X-direction field case shows one of the RTI arms has more upward growth at both 5 ns and 8 ns, and a more diffuse arm roll-up on the right side in comparison to the 23 T Y-direction field case. Lastly, the thinning at the upper portion of the spike in the 23 T X-direction field case appears to more counter-clockwise rotation than in either the 23 T Y-direction field case or the unmagnetized case. Unfortunately, 3D modeling of these target designs reveals that the ability to resolve these differences would be incredibly difficult, even with FZP development and fine-tuning. Consequently, future experimental designs will need to be refined to circumvent these issues, and utilizing 3D modeling, a better target design will be developed to produce observable RTI morphology changes with and without a magnetic field.

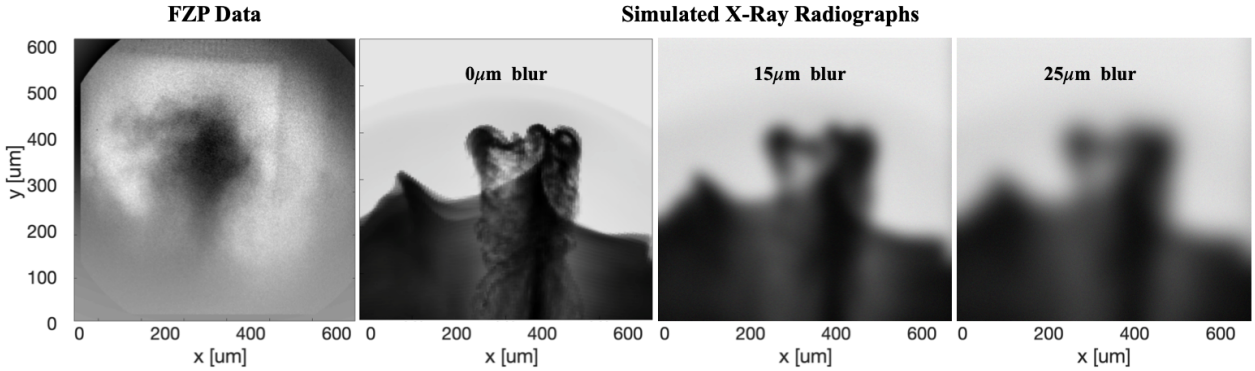

Figure 10: A FZP image at 5 ns of the unmagnetized experimental case, left, showing a central RTI spike. The additional images are synthetic x-ray radiographs of a 3D Ares simulation of the same initial conditions showing comparable RTI growth and morphology at 5 ns. Due to the low resolution in the data, externally applied Gaussian blurs, 15 µm and 25 µm, and a 10% artificial noise applied were used on the 3D Ares simulation to benchmark the laser drive and the general RTI development and morphology, but not the significant small-scale morphology.

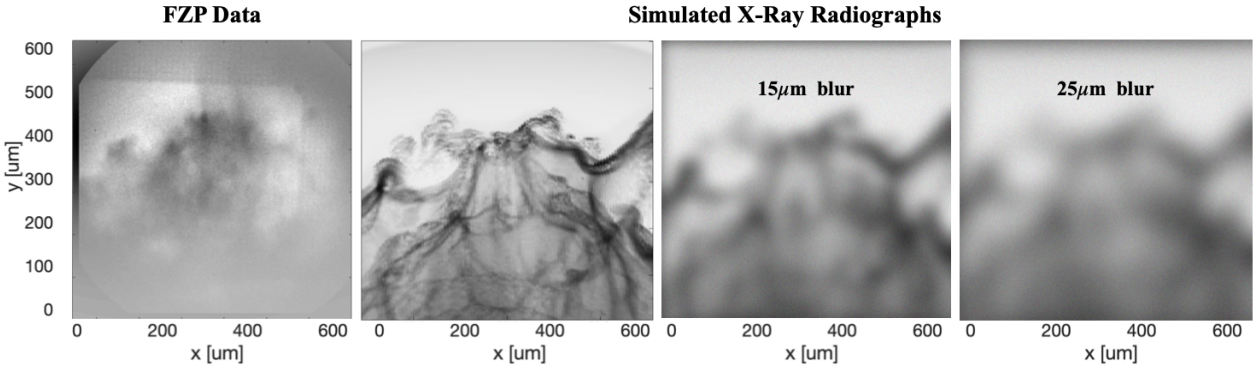

Figure 11: A FZP image at 5 ns of the magnetized experimental case, left, showing a domed interface, and a possible jet ahead of the interface. The comparative images are synthetic x-ray radiograph of a 3D Ares simulation with an included gap and internal doming of the low density foam to replicate capillary effects seen in the target assembly. Additional simulated x-ray radiographs with Gaussian blurs of 15 µm and 25 µm with a 10% artificial noise applied are shown for comparison with the low resolution FZP data.

6. Conclusions

The work presented here focuses on a demonstration of a viable experimental platform on Omega-EP to study thin-layer RTI in a planar blast-wave driven configuration. The primary goal is to observe and understand RTI morphology seeded by single-features during deceleration with and without an externally applied magnetic field. The experimental design illustrates the unique nature of the materials and construction of the targets prompting two studies on the effect assembly flaws in the targets, gaps between materials and a tilt in the pusher-foam, have on RTI morphology. The computational studies in Ares demonstrate that a slight tilt in the pusher material with a small gap has less of an observable effect on the RTI morphology than a significant vacuum gap does. Additionally, the application of an externally applied magnetic field in the Y-direction does result in some change in the RTI morphology in the tilt study, but significantly more change in the gap study. These studies are used to better understand the experimental thin-layer RTI FZP image data collected at Omega-EP.

Using the studies of the impacts on RTI morphology, the experimental data is then benchmarked in Ares. Simulated x-ray radiographs of 3D Ares simulations obtained using HADES highlight that the overall propagation and general morphology of the RTI is validated in the unmagnetized case, especially with artificial Gaussian blurs. The 23 T experimental case did not show distinct RTI growth, just a domed interface and a possible jet feature. 3D Ares simulations were able to identify the initial conditions of a gap between the foam materials, including a possible domed gap in the low density foam due to the capillary effect during construction resulting in the domed interface observed in figure 11. However, the possible jet feature is not replicated in Ares, implying it's presence in the FZP data could be due to an asymmetry in the target, an artifact of the imaging data, or Ares not utilizing the correct physics to replicate the feature. The use of 3D simulations for validation is instrumental in accounting for the inherent 3D nature of the experimental design and future designs.

Given the impact that target defects have on the exper-

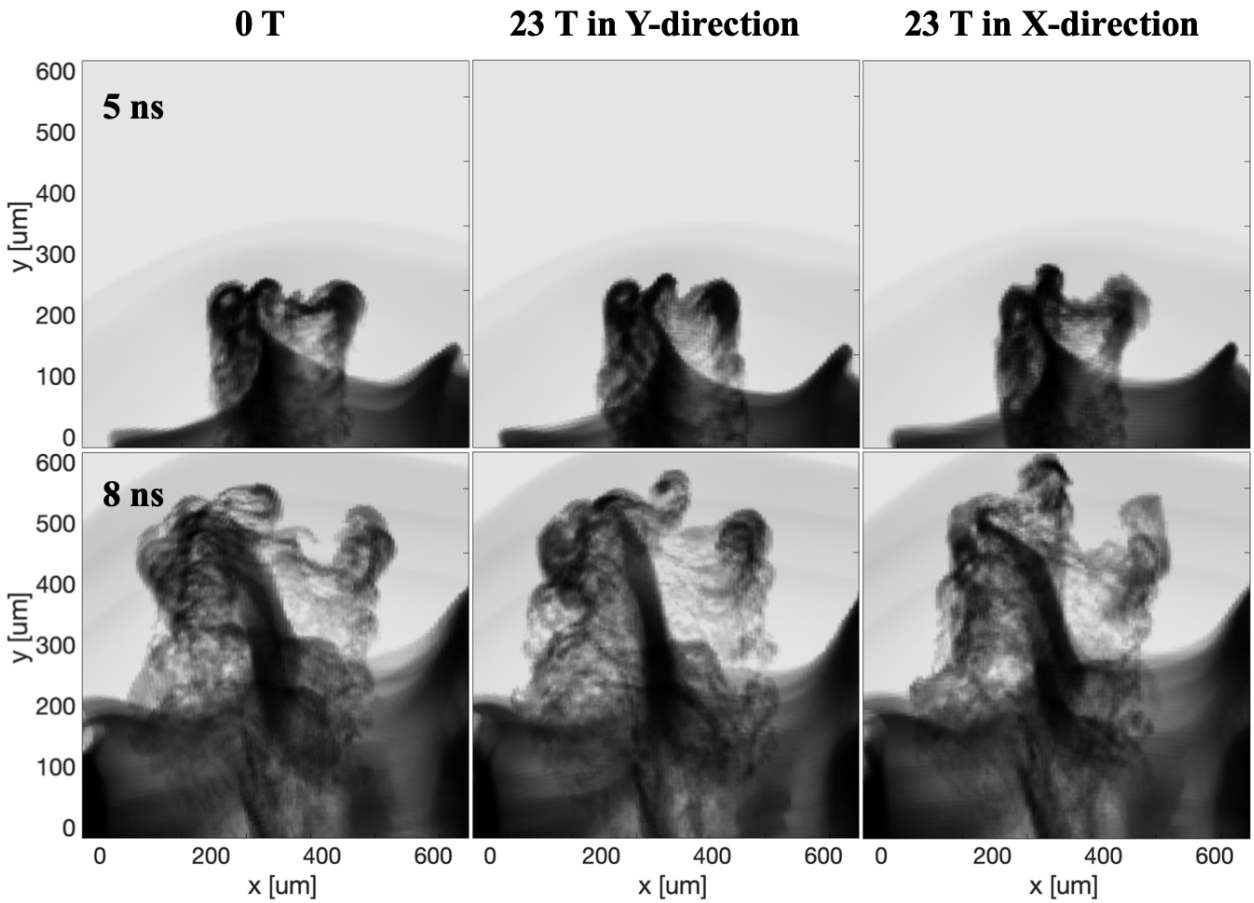

Figure 12: Simulated x-ray radiographs of 3D Ares simulations showing RTI morphology at 5 ns, top row, and 8 ns, bottom row. These simulated x-ray radiographs demonstrate the idealized expected FZP results of the experimental setup with no manufacturing defects, no gaps, and no tilts in the physics package. Additionally, a unmagnetized case is shown in the first column, a 23 T Y-direction field in the second column, and 23 T X-direction field in the third column. The overall RTI propagation is comparable between cases, but with even better resolution, up to 1 µm, using additional FZP development, the morphology between cases could possibly be visible.

imental data, a set of 3D Ares simulations of targets as originally designed in figure 1 are presented. Relying on on a higher fidelity image resolution of 5 µm, these morphology differences could feasibly be observed in future iterations of the experiment. The 3D simulations of an unmagnetized configuration, a configuration with a 23 T magnetic field in horizontal direction, and a 23 T magnetic field in vertical direction configuration provide insight into the anticipated experimental results from the targets as designed in figure 1. At resolutions of 5 µm the diverging morphology between the three RTI cases may be resolved experimentally, but redesigning the targets using 3D simulations could provide a target design with a more observable difference between the RTI evolution with and without a magnetic field. Future iterations of these experiments will further validate the computational models, and with improved resolution, have the potential to validate the conductivity models used for these and similar materials. Such validation is crucial going forward in ICF and MagLIF (magnetized Liner Inertial Fusion) experiments in order to reduce ignition criteria and understand mitigation of the RTI growth in these platforms.

Acknowledgement

This work was supported by the Office of Science of the U.S. Department of Energy under Award No. DE-SC0020055 and US Department of Energy DE-SC0022319 by the Financial Assistance Program.

References

[1] D. Clark, C. Weber, A. Kritcher, J. Milovich, P. Patel, S. Haan, B. Hammel, J. Koning, M. Marinak, M. Patel, C. Schroeder, S. Sepke, M. Edwards, Modeling and projecting implosion performance for the National Ignition Facility, Nuclear Fusion 59 (2018) 032008. URL: https://doi.org/10.1088/1741-4326/aabcf7. doi:10.1088/1741-4326/aabcf7.

[2] D. S. Clark, C. R. Weber, J. L. Milovich, A. E. Pak, D. T. Casey, B. A. Hammel, D. D. Ho, O. S. Jones, J. M. Koning, A. L. Kritcher, M. M. Marinak, L. P. Masse, D. H. Munro, M. V. Patel, P. K. Patel, H. F. Robey, C. R. Schroeder, S. M. Sepke,

M. J. Edwards, Three-dimensional modeling and hydrodynamic scaling of National Ignition Facility implosions, Physics of Plasmas 26 (2019) 050601. doi:10.1063/1.5091449.

[3] B. M. Haines, C. H. Aldrich, J. M. Campbell, R. M. Rauenzahn, C. A. Wingate, High-resolution modeling of indirectly driven high-convergence layered inertial confinement fusion capsule implosions, Physics of Plasmas 24 (2017) 052701. doi:10.1063/1.4981222.

[4] J. P. Sauppe, B. M. Haines, S. Palaniyappan, P. A. Bradley, S. H. Batha, E. N. Loomis, J. L. Kline, Modeling of direct-drive cylindrical implosion experiments with an Eulerian radiation-hydrodynamics code, Physics of Plasmas 26 (2019) 042701. doi:10.1063/1.5083851.

[5] B. Hammel, et al., High-mode Rayleigh-Taylor growth in NIF ignition capsules, High Energy Density Physics 6 (2010) 171–178.

[6] C. Weber, et al., Mixing in ICF implosions on the Nation Ignition Facility caused by the fill-tube, Physics of Plasmas 27 (2020) 032703.

[7] A. Pak, L. Divol, C. R. Weber, L. F. B. Hopkins, D. S. Clark, E. L. Dewald, D. N. Fittinghoff, V. Geppert-Kleinrath, M. Hohenberger, S. Le Pape, T. Ma, A. G. MacPhee, D. A. Mariscal, E. Marley, A. S. Moore, L. A. Pickworth, P. L. Volegov, C. Wilde, O. A. Hurricane, P. K. Patel, Impact of localized radiative loss on inertial confinement fusion implosions, Phys. Rev. Lett. 124 (2020) 145001. URL: https://link.aps.org/doi/10.1103/PhysRevLett.124.145001. doi:10.1103/PhysRevLett.124.145001.

[8] J. J. Kuczek, B. M. Haines, Simulated impact of fill tube geometry on recent high-yield implosions at the National Ignition Facility, Physics of Plasmas 30 (2023) 092706. URL: https://doi.org/10.1063/5.0156346. doi:10.1063/5.0156346.

[9] D. Clark, et al., Radiation hydrodynamics modeling of the highest compression inertial confinement fusion ignition experiment from the Nation Ignition Campaign, Physics of Plasmas 22 (2015) 022703.

[10] E. Ott, Nonlinear Evolution of the Rayleigh-Taylor Instability of a Thin Layer, Physical Review Letters 29 (1972) 1429–1432.

[11] C. Zulick, Y. Aglitskiy, M. Karasik, A. Schmitt, A. Velikovich, S. Obenschain, Multimode hydrodynamic instability growth of preimposed isolated defects in ablatively driven foils, Physical Review Letters 125 (2020) 055001.

[12] B. Srinivasan, X.-Z. Tang, The mitigating effect of magnetic fields on Rayleigh-Taylor unstable inertial confinement fusion plasmas, Physics of Plasmas 20 (2013) 056307.

[13] B. Srinivasan, X.-Z. Tang, On the study of hydrodynamic instabilities in the presence of background magnetic fields in high-energy-density plasmas, EPL (Europhysics Letters) 107 (2014) 65001.

[14] M. J.-E. Manuel, B. Khiar, G. Rigon, B. Albertazzi, S. R. Klein, F. Kroll, F. E. Brack, T. Michel, P. Mabey, S. Pikuz, J. C. Williams, M. Koenig, A. Casner, C. C. Kuranz, On the study of hydrodynamic instabilities in the presence of background magnetic fields in high-energy-density plasmas, Matter and Radiation at Extremes 6 (2021) 026904. doi:10.1063/5.0025374.

[15] C. Samulski, B. Srinivasan, M. J.-E. Manuel, R. Masti, J. P. Sauppe, J. Kline, Deceleration-stage Rayleigh-Taylor growth in a background magnetic field studied in cylindrical and cartesian geometries, Matter and Radiation at Extremes 7 (2022) 026902. doi:10.1063/5.0062168.

[16] C. C. Kuranz, R. P. Drake, M. J. Grosskopf, B. Fryxell, A. Budde, J. F. Hansen, A. R. Miles, T. Plewa, N. Hearn, J. Knauer, Spike morphology in blast-wave-driven instability experiments, Physics of Plasmas 17 (2010) 052709. doi:10.1063/1.3389135.

[17] C. C. Kuranz, R. P. Drake, M. J. Grosskopf, A. Budde, C. Krauland, D. C. Marion, A. J. Visco, J. R. Ditmar, H. F. Robey, B. A. Remington, A. R. Miles, A. B. R. Cooper, C. Sorce, T. Plewa, N. C. Hearn, K. L. Killebrew, J. P. Knauer, D. Arnett, T. Donajkowski, Three-dimensional blast-wave-driven Rayleigh-Taylor instability and the effects of long-wavelength modes, Physics of Plasmas 16 (2009) 056310. doi:10.1063/1.3099320.

[18] B. A. Remington, S. V. Weber, M. M. Marinak, S. W. Haan, J. D. Kilkenny, R. J. Wallace, G. Dimonte, Single-mode and multimode Rayleigh-Taylor experiments on Nova, Physics of Plasmas 2 (1995) 241–255. doi:10.1063/1.871096.

[19] B. A. Remington, H.-S. Park, D. T. Casey, R. M. Cavallo, D. S. Clark, C. M. Huntington, C. C. Kuranz, A. R. Miles, S. R. Nagel, K. S. Raman, V. A. Smalyuk, Rayleigh-Taylor instabilities in high-energy density settings on the National Ignition Facility, Proceedings of the National Academy of Sciences 116 (2019) 18233–18238. doi:10.1073/pnas.1717236115.

[20] R. P. Drake, D. R. Leibrandt, E. C. Harding, C. C. Kuranz, M. A. Blackburn, H. F. Robey, B. A. Remington, M. J. Edwards, A. R. Miles, T. S. Perry, R. J. Wallace, H. Louis, J. P. Knauer, D. Arnett, Nonlinear mixing behavior of the three-dimensional Rayleigh-Taylor instability at a decelerating interface, Physics of Plasmas 11 (2004) 2829–2837. doi:10.1063/1.1651492.

[21] N. C. Swisher, C. C. Kuranz, D. Arnett, O. Hurricane, B. A. Remington, H. F. Robey, S. I. Abarzhi, Rayleigh-Taylor mixing in supernova experiments, Physics of Plasmas 22 (2015) 102707. doi:10.1063/1.4931927.

[22] L. Perkins, D.-M. Ho, B. Logan, G. Zimmerman, M. Rhodes, D. Strozzi, D. Blackfield, S. Hawkins, The potential of imposed magnetic fields for enhancing ignition probability and fusion energy yield in indirect-drive inertial confinement fusion, Physics of Plasmas 24 (2017) 062708.

[23] J. P. Knauer, O. V. Gotchev, P. Y. Chang, D. D. Meyerhofer, O. Polomarov, R. Betti, J. A. Frenje, C. K. Li, M. J.-E. Manuel, R. D. Petrasso, J. R. Rygg, F. H. Seguin, Compressing magnetic fields with high-energy lasers, Physics of Plasmas 17 (2010) 056318. doi:10.1063/1.3416557.

[24] P. Chang, G. Fiksel, M. Hohenberger, J. Knauer, R. Betti, F. Marshall, D. Meyerhofer, F. Séguin, R. Petrasso, Fusion yield enhancement in magnetized laser-driven implosions, Physical review letters 107 (2011) 035006.

[25] B. E. Morgan, J. A. Greenough, Large-eddy and unsteady rans simulations of a shock-accelerated heavy gas cylinder, Shock Waves 26 (2016) 355–383. URL: https://doi.org/10.1007/s00193-015-0566-3. doi:10.1007/s00193-015-0566-3.

[26] C. Samulski, Deceleration Stage Rayleigh-Taylor Instability Growth in Inertial Confinement Fusion Relevant Configurations, Master's thesis, 2021.

[27] A. Do, M. Briat, S. Baton, M. Krumrey, L. Lecherbourg, B. Loupias, F. Pérez, P. Renaudin, C. Rubbelynck, P. Troussel, Two-channel high-resolution quasi-monochromatic X-ray imager for Al and Ti plasma, Review of Scientific Instruments 89 (2018) 113702.

[28] M. F.J., et al., High-resolution X-ray radiography with Fresnel zone plates on the University of Rochester's OMEGA Laser Systems, Review of Scientific Instruments 92 (2021) 033701.

[29] P. Nilson, F. Marshall, J. Ruby, J. Kendrick, D. Guy, S. Ivancic, C. Stoeckl, T. Collins, R. Epstein, Imaging of Hydrodynamic Perturbation Evolution in a Laser-Driven Foil with a Rippled Rear Surface Using a Fresnel Phase Zone Plate, in: APS Division of Plasma Physics Meeting Abstracts, volume 2020 of *APS Meeting Abstracts*, 2020, p. NO05.003.

[30] M. Aufderheide, D. Slone, A. Wittenau, HADES, a radiographic simulation code, AIP Conference Proceedings 557 (2001) 507–513. doi:10.1063/1.1373801.

[31] M. B. Aufderheide, G. Henderson, A. E. S. von Wittenau, D. M. Slone, H. E. Martz, HADES, a code for simulating a variety of radiographic techniques, IEEE Symposium Conference Record Nuclear Science 2004. 4 (2004) 2579–2583 Vol. 4. URL: https://api.semanticscholar.org/CorpusID:43667040.

[32] C. Huntington, K. Raman, S. Nagel, S. MacLaren, T. Baumann, J. Bender, S. Prisbrey, L. Simmons, P. Wang, Y. Zhou, Split radiographic tracer technique to measure the full width of a high energy density mixing layer, High Energy Density Physics 35 (2020) 100733. URL: https://www.sciencedirect.

com/science/article/pii/S1574181818300892. doi:https://doi.org/10.1016/j.hedp.2019.100733.

Bibliography

[1] C. Samulski, Deceleration Stage Rayleigh-Taylor Instability Growth in Inertial Confinement Fusion Relevant Configurations, Master's thesis, 2021.

[2] C. Weber, et al., Mixing in ICF implosions on the Nation Ignition Facility caused by the fill-tube, Physics of Plasmas 27 (2020) 032703.

[3] D. Clark, et al., Radiation hydrodynamics modeling of the highest compression inertial confinement fusion ignition experiment from the Nation Ignition Campaign., Physics of Plasmas 22 (2015) 022703.

[4] D. Clark, C. Weber, A. Kritcher, J. Milovich, P. Patel, S. Haan, B. Hammel, J. Koning, M. Marinak, M. Patel, C. Schroeder, S. Sepke, M. Edwards, Modeling and projecting implosion performance for the National Ignition Facility, Nuclear Fusion 59 (2018) 032008. URL: https://doi.org/10.1088/1741-4326/aabcf7. doi:10.1088/1741-4326/aabcf7.

[5] D. S. Clark, C. R. Weber, J. L. Milovich, A. E. Pak, D. T. Casey, B. A. Hammel, D. D. Ho, O. S. Jones, J. M. Koning, A. L. Kritcher, M. M. Marinak, L. P. Masse, D. H. Munro, M. V. Patel, P. K. Patel, H. F. Robey, C. R. Schroeder, S. M. Sepke, M. J. Edwards, Three-dimensional modeling and hydrodynamic scaling of National Ignition Facility implosions, Physics of Plasmas 26 (2019) 050601. doi:10.1063/1.5091449.

[6] B. Hammel, et al., High-mode Rayleigh-Taylor growth in NIF ignition capsules, High Energy Density Physics 6 (2010) 171–178.

[7] E. Ott, Nonlinear Evolution of the Rayleigh-Taylor Instability of a Thin Layer., Physical Review Letters 29 (1972) 1429–1432.

[8] M. F.J., et al., High-resolution x-ray radiography with Fresnel zone plates on the University of Rochester's OMEGA Laser Systems, Review of Scientific Instruments 92 (2021) 033701.

[9] P. Nilson, F. Marshall, J. Ruby, J. Kendrick, D. Guy, S. Ivancic, C. Stoeckl, T. Collins, R. Epstein, Imaging of Hydrodynamic Perturbation Evolution in a Laser-Driven Foil with a Rippled Rear Surface Using a Fresnel Phase Zone Plate, in: APS Division of Plasma Physics Meeting Abstracts, volume 2020 of *APS Meeting Abstracts*, 2020, p. NO05.003.

[10] A. V. Baez, Fresnel Zone Plate for Optical Image Formation Using Extreme Ultraviolet and Soft X Radiation, J. Opt. Soc. Am. 51 (1961) 405–412. URL: https://opg.optica.org/abstract.cfm?URI=josa-51-4-405. doi:10.1364/JOSA.51.000405.

[11] N. M. Ceglio, D. T. Attwood, E. V. George, Zone-plate coded imaging of laser-produced plasmas, Journal of Applied Physics 48 (1977) 1566–1569. URL: https://doi.org/10.1063/1.323834. doi:10.1063/1.323834. arXiv:https://pubs.aip.org/aip/jap/article-pdf/48/4/1566/18375922/1566_1_online.pdf.

[12] N. M. Ceglio, H. I. Smith, Micro-Fresnel zone plates for coded imaging applications, Review of Scientific Instruments 49 (1978) 15–20. URL: https://doi.org/10.1063/1.1135243. doi:10.1063/1.1135243.

[13] W. Chao, P. Fischer, T. Tyliszczak, S. Rekawa, E. Anderson, P. Naulleau, Real space soft x-ray imaging at 10 nm spatial resolution, Opt. Express 20 (2012) 9777–9783. URL: https://opg.optica.org/oe/abstract.cfm?URI=oe-20-9-9777. doi:10.1364/OE.20.009777.

Chapter 4

Preheat effects in laser-driven shock-tube experiments at intensities greater than $10^{15}\,\mathrm{W/cm^2}$ at Omega-EP and the NIF

Preheat effects in laser-driven shock-tube experiments at intensities greater than 10^{15} W/cm^2 at Omega-EP and the NIF

C. Samulski[a,d], M. J.-E. Manuel[c], J. Kline[d], B. Srinivasan[b,a]

[a] *Virginia Polytechnic Institute and State University, Blacksburg, VA 24060, USA*
[b] *University of Washington, Seattle, WA 98195, USA*
[c] *General Atomics, San Diego, CA , 92121, USA*
[d] *Los Alamos National Laboratory, Los Alamos, NM, 87545, USA*

Abstract

Material preheat caused by laser induced x-ray emissions and hot-electrons is a long standing issue in laser-driven inertial confinement fusion (ICF) and high-energy density (HED) experimental science. The propagation of high energy x-rays or hot-electrons has the potential to alter the initial conditions in experimental target designs, especially at material interfaces. In designing highly sensitive experimental targets to study deceleration-stage Rayleigh-Taylor instability (RTI) growth with and without a magnetic field, it is necessary to understand the potential alteration of the initial conditions from hot-electron-induced preheat. Ares hydrodynamic (HD) capabilities are used to study the effects varying levels of preheat can have on RTI evolution in experimental configurations. These experimental and computational studies demonstrate that the changing initial conditions due to hot-electron-induced preheat can impact the morphology of RTI evolution and even inhibit the intended RTI growth in such a manner that it is not observable experimentally. The necessity of better quantifying hot-electron induced preheat and mitigating it's impact on such high intensity direct-drive laser experiments in the future is discussed.

1. Introduction

The Rayleigh-Taylor instability (RTI) is a hydrodynamic instability believed to be one of the primary causes of degradation in inertial confinement fusion (ICF). Utilizing magnetic fields in ICF, which has been shown to lower ignition criteria [1, 2, 3], it is crucial to understand the impact an externally applied magnetic field has on RTI growth. In addition to ICF, RTI-like growth has been observed in astrophysical phenomena like the Crab Nebula, however instead of the spikes breaking up and becoming turbulent, they maintain their elongated shape [4, 5]. Consequently, the potential for a magnetic field to be present in such a decelerating system as the Crab Nebula further highlights the need to understand the effect of an externally applied magnetic fields on RTI evolution. The presence of a magnetic field has been shown computationally to damp RTI growth [6, 7, 8, 9], but studying this phenomena during deceleration experimentally has not yet been successful. A novel platform design for the National Ignition Facility (NIF) [9], including a first-of-its-kind user-designed magnetic field coil, is developed specifically for the purpose of studying deceleration-stage RTI in a High-Energy-Density (HED) system. The platform is designed with a blast-wave driven shock-tube platform, from which deceleration-stage RTI is seeded by a perturbation. The platform is driven with a laser intensity greater than 10^{15} W/cm^2 to reach plasma conditions at which the externally applied magnetic field is predicted to impact the RTI evolution. However, at such high laser intensities there is a risk for potentially preheating the experimental target.

Laser induced preheating of experimental targets caused by a number of processes generating x-ray emissions and hot-electrons has long been known to occur and poses a complication in laser-driven HED experimental platforms [10, 11, 12, 13, 14]. The generation of x-rays and hot-electrons moving faster than the generated shock results in the materials in front of the shock being preheated and the initial conditions of the experimental target are consequently altered [15]. Studies of these altered initial conditions have been focused on low-Z materials or the inclusion of a high-Z doped ablator to reduce the propagation of the hot-electrons beyond the ablator surface [16, 17, 18, 19, 20]. The mitigation of preheating caused by x-ray emission and hot-electrons is necessary in spherical ICF platforms where preheating of the fusion fuel reduces the compressibility of the fuel and thus limits the likelihood of achieving ignition[10]. Understanding the effects of hot-electron induced preheating is crucial in not just spherical laser direct-drive ICF, but also in planer HED experiments like the deceleration-stage RTI platform de-

*Bhuvana Srinivasan
Email addresses: csamulski@vt.edu (C. Samulski), manuelm@fusion.gat.com (M. J.-E. Manuel), jkline@lanl.gov (J. Kline), srinbhu@uw.edu (B. Srinivasan)

signed for NIF. Previous planar experiments using a direct-drive laser configuration have benchmarked a 1% conversion of laser energy to hot-electron energy, called conversion efficiency, at a laser intensity of $6.5 \times 10^{14}\,\mathrm{W/cm^3}$ [21]. Consequently, when experimental platforms are designed at high-intensities to study highly sensitive instabilities like deceleration-stage RTI, hot-electron induced preheat has a chance of changing the experimental results.

The work presented here is focused on two experimental platforms on NIF and Omega-EP designed to study changes in RTI evolution with and without an externally applied magnetic field. Specifically, the NIF target configuration consists of a divot single-feature perturbation, intended to seed thin-layer RTI [22, 23] evolution, as well as a separate sinusoidal perturbation. On Omega-EP the RTI is seeded by a similar single-feature perturbation, with the setup of both of these experimental platforms described in sections 2.1 and 3.1. Both configurations utilize foam materials and high laser intensities, larger than $10^{15}\,\mathrm{W/cm^3}$. The results of these experiments are shown in sections 2.2 and 3.2, in which the NIF data illustrates the sensitivity of the initial conditions to seed the desired RTI evolution and the Omega-EP experiment successfully presents data showing the presence of hot-electrons. The potential effects hot-electrons have on the experimental configurations is explored computationally in sections 4.1 and 4.2 using hydrodynamic (HD), laser, radiation, thermal diffusion and Equation of State (EOS) capabilities in Ares [24]. Finally, a discussion on the importance of understanding the preheat effects on experimental designs is presented in section 5. This work presents a novel experimental platform on NIF intended to study RTI evolution with and without a background magnetic field, as well as a computational exploration of hot-electron induced preheating effects on target evolution utilizing data from a novel Omega-EP platform also designed to study RTI with and without a magnetic field.

2. Experimental Design and Results on NIF

2.1. Experimental Design

An experimental platform built for NIF is presented, and is designed based on the findings in Ref. [9]. Relevant design work is presented in Ref. [9] and Ref. [23], with the exploration of relevant plasma conditions, including the magnetic Reynolds number (R_m) and plasma β required for the experimental platform to reach a regime in which an externally applied magnetic field will have a measurable damping effect on RTI growth. Specifically, the target fielded at NIF, seen in figure 1, consists of a double-sided square target with a sinusoidal perturbation on one side and a divot on the opposite side. The target is expected to reach conditions where R_m is 55 and is significantly larger than 1. These conditions indicate that the resistve-MHD model's predicted 50 µm difference in RTI spike size [9] with and without an externally applied magnetic feild will be observable experimentally.

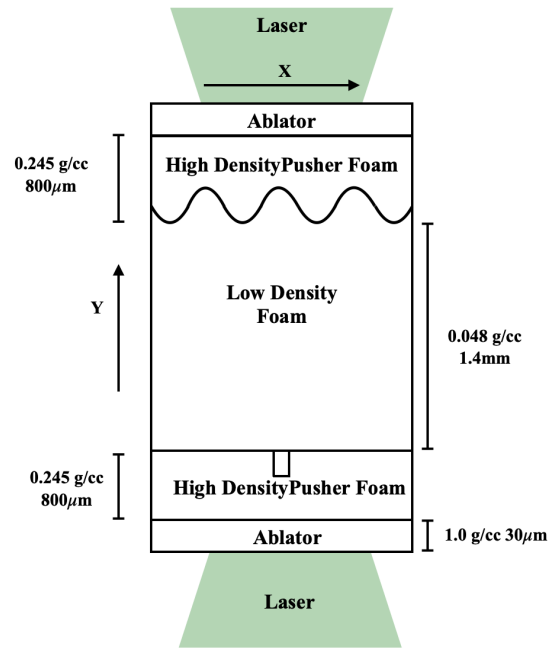

Figure 1: A schematic of the physics package used on NIF, where the materiel used for the high density foam is a nickel-doped carbon foam. The package is driven on both sides by 3 ns square laser pulses at 96 000 J each.

The NIF target illustrated in figure 1 consists of two $1\,\mathrm{g\,cm^{-3}}$ ablators, and uses 800 µm of nickel-doped-carbon foam as the $0.245\,\mathrm{g\,cm^{-3}}$ high-density-foam-pusher material. The low density foam is a $0.048\,\mathrm{g\,cm^{-3}}$ CH foam. The perturbations used as the seeding mechanism for RTI are a 120 µm wavelength sinusoid with a peak-to-valley amplitude of 40 µm, and a divot with a width of 82 µm and a depth of 136 µm. Both sides of the target are driven by a 3 ns laser pulse of 192 kJ with an intensity of $2.8 \times 10^{15}\,\mathrm{W/cm^2}$. X-ray radiography is used as the primary diagnostic, along with the addition of a first of it's kind user-defined coil. **Mario's Coil Section?**

2.2. Results

The data from NIF consists of three experiments, one magnetized and two unmagnetized. The x-ray radiograph of the 23 T magnetized data can be seen in the left most image of figure 2, with the target oriented with the sinusoidal perturbation at the bottom and the divot at the top. The x-ray radiograph of the magnetized data shows a relatively smooth surface on the side where RTI seeded by the sinusoidal perturbation is expected. Additionally, the divot side interface has not propagated far enough into the field of view to be resolved with any measure of accuracy due to slower interface speeds than pre-experiment simulations predict.

Data from the two unmagnetized experiments are shown in the center and right x-ray radiographs in figure 2. The center x-ray radiographs correspond to a target setup with the sinusoidal perturbation on the bottom and the divot

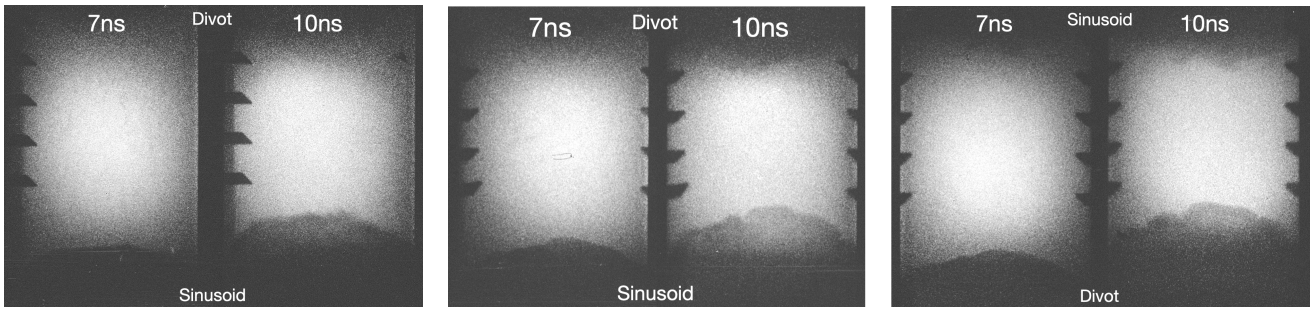

Figure 2: X-ray radiographs of experimental NIF data for a magnetized shot in the left plot, unmagnetized shots in the center plot and in the right plot. In all three cases there is no distinguishable RTI evolution from either perturbation.

at the top, same as in the magnetized data. As seen in the magnetized data on the left of figure 2, the sinusoidal interface does not show any measurable RTI growth at both 7 ns or 10 ns. The divot interface does appear to be visible at the top of the center x-ray radiograph, though no visible RTI growth is observable. Similarly, the right most x-ray radiograph corresponds to the final experimental shot where the divot interface is at the bottom of the image and the sinusoidal perturbation at the top, as seen in the schematic in figure 1. Similar to both the magnetized and unmagnetized x-ray radiographs with the sinusoidal perturbation at the bottom, there is no measurable RTI growth occurring at either image timings. Consequently, all three experiments show a significant discrepancy from predictions of RTI growth regardless of the presence of the magnetic field

3. Experimental Design and results at Omega-EP

3.1. Experimental Design

The experimental design built for Omega-EP consists of a blast-wave-driven thin-layer RTI platform in a shock-tube similar to the NIF target design. The configuration consists of a $1\,\mathrm{g\,cm^{-3}}$, $10\,\mu\mathrm{m}$ thick ablator, on which a high-density-pusher-foam made of $0.245\,\mathrm{g\,cm^{-3}}$ tantalum pentoxide, tantala, is glued. The tantala foam is $150\,\mu\mathrm{m}$ thick and has a $55\,\mu\mathrm{m}$ wide by $100\,\mu\mathrm{m}$ deep divot set into the material. The divot acts as a single-feature perturbation from which thin-layer RTI will evolve. The perturbation side of the tantala abuts a low density, $0.038\,\mathrm{g\,m^{-3}}$, CH foam filling the remainder of the shock-tube. A laser drive of approximately 4300 J using $400\,\mu\mathrm{m}$ phase plates is incident on a $400\,\mu\mathrm{m}$ spot on the ablator surface, providing an intensity of $1.7 \times 10^{15}\,\mathrm{W/cm^2}$.

The primary diagnostic to measure the hot electrons generated at the high laser intensity is the Osaka University electron spectrometer (OUESM) [25]. The OUESM diagnostic consists of five channels at a range of angles, $0° \pm 10°$, from which hot electron measurements are collected. The image plate data from the OUESM is processed for each channel, where the depth into the channel and intensity of signal correlates to the measured hot electron population.

3.2. Results

The equations in Habara 2019 [25] are used to convert the raw data from the OUESM to determine the spectrum of the hot electrons generated. Figure 3 presents the energy of the electrons in units of MeV versus the spectrum of electrons in units of 1/MeV for a single experimental shot. As can be seen in figure 3, there is some variation of the measured hot electron populations, owing to the channels being at different angles and channel 1 and 5 housing shorter magnets. However, when comparing the electron energy versus spectrum across all unmagnetized shots, as seen in figure 4, there is consistency in the measured hot electron populations for a single channel. Consequently, the differences seen in figure 3 when compared to the consistency in figure 4, confirms that the varying angle of the channel is the source of the slightly differing measurements.

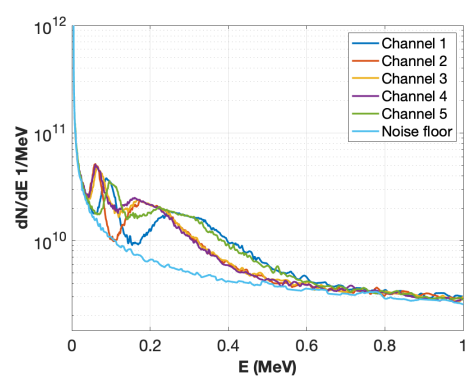

Figure 3: The accelerated hot electrons per energy per solid angle from a single shot, 38818, across all five channels of the OUESM detector. Owing to the smaller magnetic length in channel 1 and 5, there is some variation, but the center three channels correspond well to each other.

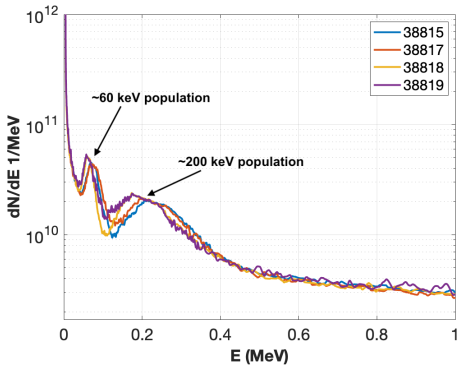

Figure 4: A comparison of the accelerated hot electrons per energy per solid angle collected on Channel 2 across all the shots that were not magnetized. There are two distinct peaks that overlap well across all shots, corresponding to hot electron generated by the back-lighter and the laser drive.

Figures 3 and 4 show two distinct energies where the spectrum diverges from the noise floor measurement. These two populations occur at approximately 60 keV and 200 keV, indicated by the arrows in figure 4. The 60 keV population is attributed to hot electrons generated by the backlighter used with the imaging diagnostic, because it is present in all shots, including test shots that only included a backlighter laser drive. Therefore, the hot electron population at 200 keV can be attributed to the high intensity laser drive used on the targets. The temperature, T_{hot}, of hot electron population being 200 keV justifies the assumption that this population of hot electrons could be preheating the target materials before the shock-wave propagates through the materials. Consequently it is crucial to understand how the possible preheating of the target could affect the thin-layer RTI evolution.

4. Estimated Preheat Effects on Targets at Omega-EP and NIF

4.1. Preheat effects on Omega-EP

Utilizing the hot-electron data collected during the Omega-EP experiments, a range of potential preheat temperatures are estimated. Previous planar experiments [21] on Omega-EP show a 1% conversion efficiency at a laser intensity of approximately $6.5 \times 10^{14}\,\mathrm{W/cm^2}$. The experimental laser intensity is $1.7 \times 10^{15}\,\mathrm{W/cm^2}$ so a range of conversion efficiencies is considered, starting with the 1% found in the Yaakobi [21] study and extrapolating that predicted trend out to 20%.

Table 1 presents these conversion efficiencies and the corresponding hot electron population energy, E_{hot}, in Joules, and preheat temperature estimates for the ablator, high-density tantala foam, and low-density CH foam in electron Volts. The conditions under which the the material temperatures are estimated uses the T_{hot} of 200 keV, the total mass of each material, its heat capacity, and its ESTAR estimated stopping power. The electron energy deposited in a material layer is calculated by multiplying the E_{hot} by a normalized spectrum of energies, $\frac{dN}{dE}$, between 10 keV and $4 \times T_{hot}$, and multiplying by E_{lost}, which is the energy of the electrons that make it through the respective materials, $E_{dep} = E_{hot} \times \frac{dN}{dE} \times E_{lost}$. The energy deposited is divided by the heat capacity and mass of the materials to estimate the preheat temperature. The estimates for preheat temperature use known heat capacities of the materials at solid density and use the worst case assumption that the hot-electron population is directed solely through all of the target mass with little directional divergence.

As can be seen in table 1 the unlikely estimate of a 1% conversion efficiency results in preheat temperatures that are comparatively small, on the order of 1 eV or less. However, as can be expected, increased conversion efficiencies result in relatively large preheat estimates, particularly in the cases of 10% causing a 11.5 eV preheat in the tantala. Additionally,the 20% case produces a 23.1 eV preheat in the tantala, a 11.3 eV preheat in the low-density foam, and an ablator preheat of 6.9 eV. It is vital to understand the possible effects the preheat may have on the target conditions at theses varying conversion efficiencies.

Using the estimated preheat tempertures as part of the initial conditions in Ares simulations, a study of the effects of preheat on the target and RTI evolution is performed, seen in figure 5. The top row correlates to density plots at 5 ns with no preheat in the column on the far left and increasing to a 20% conversion efficiency case on the far right. The same preheat conditions are presented in the second row at 8 ns. Thin-layer RTI evolution differs from the classical spike and bubble formation when the seed perturbation is a single mode or multi-mode sinusoidal perturbation. Thin-layer RTI presents morphology in which there is a central RTI spike and arms extending to the sides, horizontally, of the spike which fall back towards the interface as the RTI evolves and the interface propagates [22]. As can be seen in both rows of figure 5 and in all columns, there is clear thin-layer RTI growth with a central spike and arms developing.

In the 1% and 5% conversion efficiency cases, seen in figure 5, the RTI morphology does not differ much at both 5 ns and 8 ns when compared to the zero preheat case. In all three of these cases there is a visible central spike at both 5 ns and 8 ns, with the arms extending to the sides from the center of the spike at 5 ns and beginning to fall towards the interface at 8 ns. When the conversion efficiency is increased to 10% and 20% the RTI morphology differs from the zero preheat case, however, there is still substantial RTI evolution. The 10% case has a much smaller central spike at 5 ns and the arms spread from the top of the RTI spike at both times. The 20% case shows a heart-shaped growth at 5 ns without a central spike and at 8 ns, the spike does not extend above the arms as in the other cases. Consequently, it can be estimated that the preheating effects of the hot electrons generated by the laser drive did not have a substantially negative impact

Conversion Efficiency	E_{hot} (J)	SiCH ablator (eV)	high-density tantala foam (eV)	low-density CH foam (eV)
1%	43	0.34	1.2	0.53
5%	215	1.7	5.8	2.7
10%	430	3.4	11.5	5.6
20%	860	6.9	23.1	11.3

Table 1: A calculation of the preheat temperatures from the hot electrons generated by the laser drive. Each material layer in the physics package is effected differently owing to material properties and the thickness of the layers. A range of conversion efficiencies was used to account for the unknown magnitude of conversion efficiencies on Omega-EP at the $1.67 \times 10^{15}\,\mathrm{W/cm^2}$ intensity range.

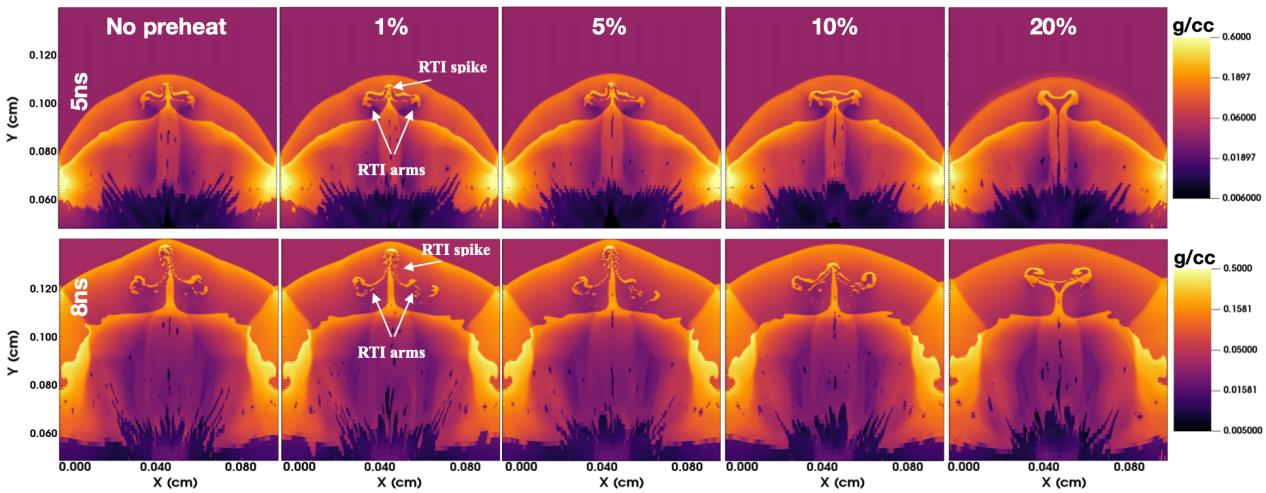

Figure 5: Density plots of Ares simulations at 5 ns in the top row and 8 ns in the bottom row. The columns correspond to the preheat estimates based on the conversion efficiencies in Table 1, starting with no preheat on the left and increasing to 20% on the right. Thin-layer RTI growth is seen in all cases, though the morphology does change as the conversion efficiency increases.

on the targets and on the experimental objective of observing RTI growth. Given the data's resolution [23] cannot distinguish between the subtle morphology differences that are a consequence of the varying preheat temperatures, a definitive estimate of the conversion efficiency and subsequent preheat temperature are not possible to determine accurately. However, given the experimental data does show RTI growth [23], it can be concluded that the simulations may be a good representation of the varying preheat temperatures on the target and the resulting RTI evolution.

4.2. Estimated preheat effects on NIF

Given the loss of observable RTI growth in the NIF data, and the higher intensity laser drive, $2.8 \times 10^{15}\,\mathrm{W/cm^2}$, there is potential for hot-electron-generated preheat to alter the target conditions. Utilizing the observed hot-electron generation during the Omega-EP experiments, it can be extrapolated that there was likely similarly hot-electron generation during the NIF experiment. Specifically, given the Omega-EP configuration utilized a laser intensity of $1.7 \times 10^{15}\,\mathrm{W/cm^2}$, which is within a factor of two of the NIF laser intensity, $2.8 \times 10^{15}\,\mathrm{W/cm^2}$, the Omega-EP hot-electron data is used as an baseline for estimating the preheat temperatures at NIF. Table 2 presents preheat temperature estimates for the materials in the NIF target using the same estimated conversion efficiencies of 1%, 5%, 10% and 20%, applied to the 192 kJ total laser drives, and uses the hot-electron temperature estimate, T_{hot}, of 200 keV estimated from the Omega-EP data.

The primary differences between the Omega-EP configuration and NIF configuration, apart from the laser intensities, is the size and materials used in the targets. For example, the high density pusher material in the NIF configuration consists of NiCRF with a thickness of 800 µm, which is more than 5x the thickness of the tantala pusher used on Omega-EP. Additionally, as can be seen in figure 1, the target used on NIF is double sided, with both the top and bottom being driven by the lasers. Consequently, the estimated preheat temperatures of both the ablator material and the low density CH material are substantially higher in table 2 when compared to table 1. Specifically, in the 20% conversion efficiency case, the ablator preheat is estimated as 15.6 eV on NIF and is 6.9 eV on Omega-EP, and the low density foam on NIF is 25 eV verses 11.3 eV at Omega-EP. Therefore, it is not surprising that the addition of the estimated preheat temperatures changes the RTI evolution in the NIF configuration.

The changes to the RTI evolution can be seen at the different times presented in figure 6. Specifically, looking at the 4 ns time across all preheat temperature estimates, both the no preheat and 1% cases show that the

Conversion Efficiency	E_{hot} (J)	CH ablator (eV)	high-density NiCRF foam (eV)	low-density CH foam (eV)
1%	1920	0.78	1.1	1.3
5%	9600	3.9	5.5	6.3
10%	19200	7.8	11.0	12.5
20%	38400	15.6	21.9	25.0

Table 2: Using the 200 keV T_{hot} calculated from the Omega-EP data, pre-heat estimates are made for the NIF configuration. A dual-sided NIF drive is considered to determine the effects of hot electrons on the NIF physics package. These estimates are made using an intensity of 2.8×10^{15} W/cm^2.

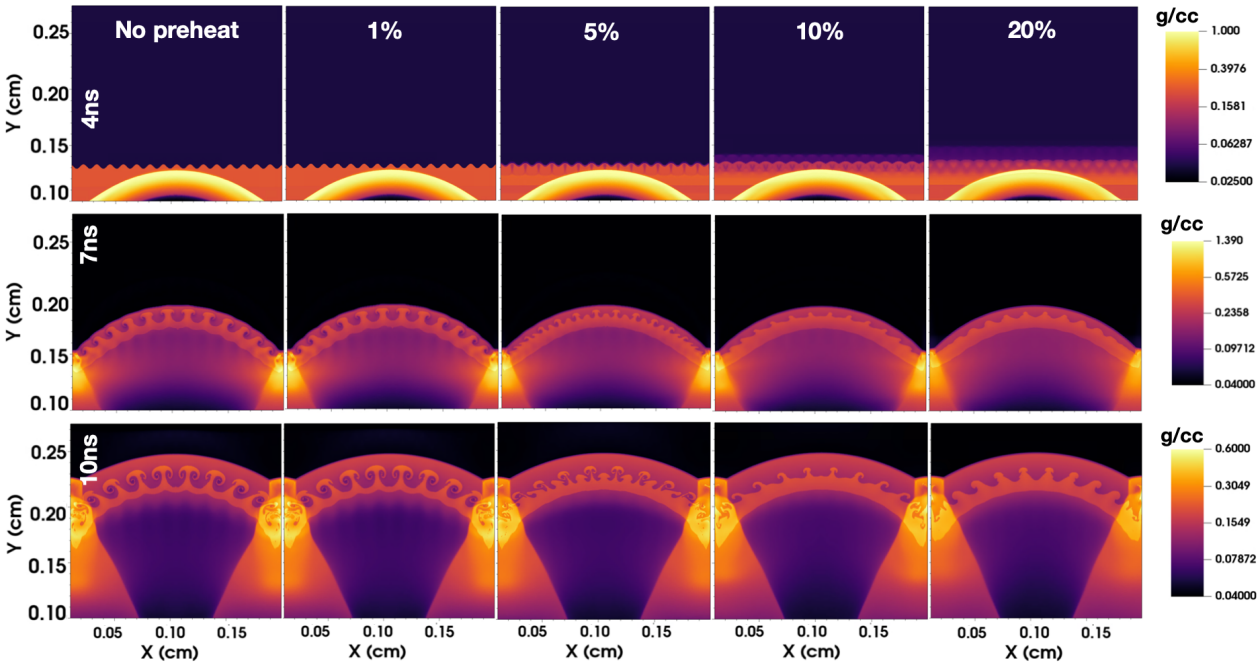

Figure 6: Density plots at 4 ns in the top row, 7 ns in the middle row, and 10 ns in the bottom row. The columns correspond to changing preheat temperature estimates of the high density pusher foam, with no added preheat on the left and increasing to the highest, 21.9 eV, on the right.

sinusoidal perturbation remains intact with a sharp density change between the high-density foam and low-density foam. Shifting to the 5% case, there appear to be an additional mode growing between each wavelength of the sinusoidal perturbation. In the hotter 10% case additional mode growth is out growing the initial sinusoidal perturbation and the presence of some density diffusion across the perturbation interface has begun. Lastly, the 20% case shows the sinusoidal perturbation is diffused to such an extent that the original seed perturbation and amplitude is hard to distinguish.

As a result of the changing interface condition seen at 4 ns in figure 6, fast Fourier transformations (FFT) are taken of the perturbation interface to determine possible changing mode growths resulting from the preheat. These FFTs can be seen in figure 7, with no preheat on the left and the preheat value increasing to 20% on the right. In all cases the seed perturbation is visible in the lower left of the plots, however the continuity of the presence of that seed perturbation up to 3 ns only occurs in the no preheat and 1% cases. In the 5% case there appears to be diffusion of the perturbation interface where by 3 ns, before the shock breaks out of the perturbation interface, there appears to be one or two additional modes present. Additionally, in the high preheat cases on the right, the original perturbation diffuses even earlier, between 1 ns and 2 ns, with the original seeded mode still present, but at a much smaller intensity and amplitude. Interestingly, in the 10% case the original seed mode does not have the highest spectral intensity at 3 ns as in all the other cases. Consequently, the diffusion of the interface seen at 4 ns in figure 6 corresponds to the shift from the seed perturbation to multiple modes and phase-shifts seen in figure 7, and the result of this change in the perturbation interface explains the differing RTI evolution at later times as seen in figure 6.

Looking back at the center row of density plots in figure 6, it can be seen at 7 ns that the RTI growth across the preheat cases differs greatly. As seen at 4 ns, the no preheat and 1% cases demonstrate similar early stage RTI growth, with RTI spikes and bubbles growing as anticipated. How-

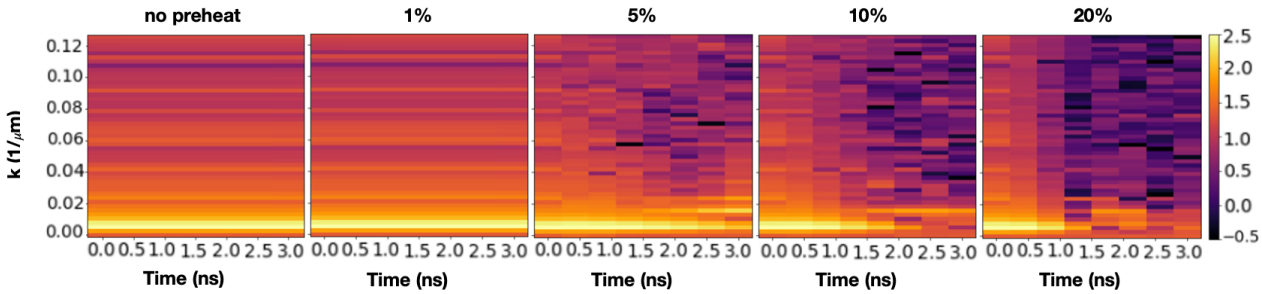

Figure 7: Fast Fourier transforms of the Y-averaged density values at the perturbation interface of the high density pusher foam and low density CH foam, over a 400 µm range in the X-direction. The data is presented across 3 ns before the shock wave crosses the perturbation interface. The Y-axis represents the wave number, the X-axis provides the time, and the color bar corresponds to spectral energy.

ever, uniquely in the 5% case there are two modes of RTI growth, with one appearing thinner and smaller in scale compared to the no preheat case, and a secondary short mode between the originally seeded perturbation growth. This dual mode growth can be attributed to the two high spectral intensity modes seen in the FFT of the 5% case in figure 7. Lastly, the high preheat temperature estimate cases show little measurable RTI growth, with only the beginnings of RTI spikes appearing at the propagation interface.

Finally, the bottom row of figure 6 shows RTI growth at 10 ns. The no preheat and lower preheat temperature cases show RTI morphology of spikes and bubbles, along with mushroom caps with Kelvin-Helmholtz instability (KHI) beginning to form. In addition to this classic RTI morphology, the 5% case maintains growth of the secondary mode, though the morphology of this RTI is shorter in comparison to the RTI growth seeded by the original perturbation. The 10% case presents with very small RTI growth, tens of microns in size, with a hook-like morphology, and is significantly smaller in scale to the low preheat cases. Interestingly, the 20% case shows larger RTI spike growth in comparison to the 10% case. Consequently, there is a possibility that a hot-electron population with a conversion efficiency between 10% and 20% could produce preheat conditions in the NIF target where the RTI evolution would be so altered and diminished it would not be observable in an x-ray radiograph.

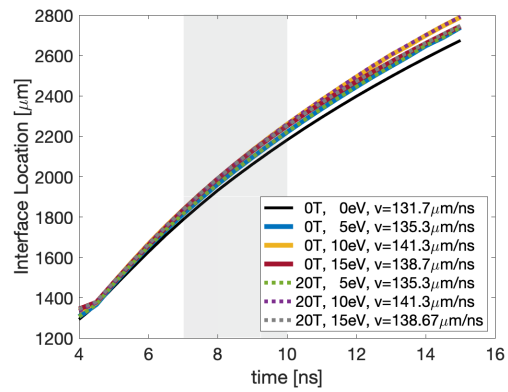

Figure 8: The interface location tracked over time for the simulated NIF configuration, without preheat or a magnetic field, as well as the 20 T magnetized and unmagnetized cases with preheat temperatures of 5 eV, 10 eV, and 15 eV. The plot also gives the relevant velocity of the interface between 7 ns and 10 ns.

Additionally, the estimated interface velocities of the unmagnetized experiments, 135±8 µm and 152±20 µm respectively, is larger than the 78±9 µm interface velocity estimated from the magnetized data. Magnetized and unmagnetized simulations with the laser drive scaled to match the experimental data shows anticipated interface velocities of approximately 137 µm in figure 8, which falls within the estimated experimental velocities of 135±8 µm and 152±20 µm for the unmagnetized experiments, but is almost twice the 78±9 µm estimated from the magnetized data. Thus, future work remains to understand this discrepancy in interface velocities between simulations and experimental data for magnetized targets in the presence of preheat while using high laser intensities.

5. Conclusions

This work presents two experimental configurations on Omega-EP and NIF designed to study RTI growth, driven with high intensity lasers. The experimental design for Omega-EP shows observable RTI growth, seeded by a divot perturbation, in x-ray radiography [23], as well as

hot-electron data from the OUESM diagnostic. The hot-electron data shows two populations, seen in figure 3 and 4, one from the backlighter at approximately 60 keV and a second larger population from the 1.7×10^{15} W/cm^2 laser drive at approximately 200 keV. The data is used to estimate an electron temperature, T_{hot}, of 200 keV. Therefore, there is sufficient justification that the hot electrons produced by the laser can preheat the targets.

Given that previous planar Omega-EP experiments found a conversion efficiency of 1% at laser intensities of 6.5×10^{14} W/cm^2, a range of possible conversion efficiencies, from 1% to 20% are considered. Table 1 presents the estimated preheat temperatures for each material in the target at the varying conversion efficiencies. Notably, the high density pusher material reaches the highest preheat estimate of 23.9 eV. Applying these preheat estimates to the simulations of the Omega-EP target shows, in figure 5, that while the RTI morphology differs, like in the 23.9 eV case, the presence of preheat does not suppress RTI evolution.

Shifting to the NIF configuration, experimentally it is observed that no visible RTI growth occurred in the x-ray radiographs with and without the magnetic field, seen in figure 2. Consequently, the potential for preheat, which is present regardless of the presence of a magnetic field, could explain why the RTI growth was lost in all the experimental cases. Using the hot electron data from the Omega-EP as a baseline, similar preheat temperature estimates are made for the NIF configuration, seen in table 2. Interestingly, in the NIF configuration the ablator and low-density-foam reach preheat temperatures more than twice as high as in the Omega-EP estimates.

Applying these preheat temperature estimates to the NIF configuration results in significantly differing RTI growth, as seen in figure 6. The perturbation interface in the no preheat and low 1.1 eV preheat cases remains intact, and causes RTI growth to evolve as expected with spikes and bubbles forming and late-in-time KH development. The 5.5 eV case shows secondary mode growth, supported by the presence of multiple wavelengths at 3 ns in the FFT seen in figure 7. While the RTI growth in this case is not as large as in the lower preheat cases, it still evolves as expected. Interestingly, extending to the 10.9 eV and 21.9 eV cases, the RTI evolves differently.

In the 21.9 eV preheat case the RTI growth is diminished in size until the 10 ns plot in figure 6, likely due to the diffusion at the perturbation interface as seen in the 4 ns plot. The 10.9 eV preheat case also has diffusion at the interface at 4 ns, but the 10 ns density plot shows the smallest RTI growth and little RTI bubble development. The FFT of the 10.9 eV preheat case also shows the initial seed perturbation as one of the lesser modes present at the perturbation interface by 3 ns. Therefore, it can be presumed that a hot electron population causing a preheat of the NiCRF between 11.0 eV and 21.9 eV could result in RTI growth that is severely damped and not observable in an x-ray radiograph. These hot-electron-generated preheat effects on RTI provide guidance for future experimental designs intended to observe RTI using high-intensity lasers.

Acknowledgement

This work was supported by the Office of Science of the U.S. Department of Energy under Award No. DE-SC0020055 and US Department of Energy DE-SC0022319 by the Financial Assistance Program.

References

[1] L. Perkins, D.-M. Ho, B. Logan, G. Zimmerman, M. Rhodes, D. Strozzi, D. Blackfield, S. Hawkins, The potential of imposed magnetic fields for enhancing ignition probability and fusion energy yield in indirect-drive inertial confinement fusion, Physics of Plasmas 24 (2017) 062708.

[2] J. P. Knauer, O. V. Gotchev, P. Y. Chang, D. D. Meyerhofer, O. Polomarov, R. Betti, J. A. Frenje, C. K. Li, M. J.-E. Manuel, R. D. Petrasso, J. R. Rygg, F. H. Seguin, Compressing magnetic fields with high-energy lasers, Physics of Plasmas 17 (2010) 056318. doi:10.1063/1.3416557.

[3] P. Chang, G. Fiksel, M. Hohenberger, J. Knauer, R. Betti, F. Marshall, D. Meyerhofer, F. Séguin, R. Petrasso, Fusion yield enhancement in magnetized laser-driven implosions, Physical review letters 107 (2011) 035006.

[4] J. J. Hester, J. M. Stone, P. A. Scowen, B.-I. Jun, I. Gallagher, John S., M. L. Norman, G. E. Ballester, C. J. Burrows, S. Casertano, J. T. Clarke, D. Crisp, R. E. Griffiths, J. G. Hoessel, J. A. Holtzman, J. Krist, J. R. Mould, R. Sankrit, K. R. Stapelfeldt, J. T. Trauger, A. Watson, J. A. Westphal, WFPC2 Studies of the Crab Nebula. III. Magnetic Rayleigh-Taylor Instabilities and the Origin of the Filaments, 456 (1996) 225. doi:10.1086/176643.

[5] J. J. Hester, The Crab Nebula : an astrophysical chimera., 46 (2008) 127–155. doi:10.1146/annurev.astro.45.051806.110608.

[6] B. Srinivasan, X.-Z. Tang, The mitigating effect of magnetic fields on Rayleigh-Taylor unstable inertial confinement fusion plasmas, Physics of Plasmas 20 (2013) 056307.

[7] B. Srinivasan, X.-Z. Tang, On the study of hydrodynamic instabilities in the presence of background magnetic fields in high-energy-density plasmas, EPL (Europhysics Letters) 107 (2014) 65001.

[8] M. J.-E. Manuel, B. Khiar, G. Rigon, B. Albertazzi, S. R. Klein, F. Kroll, F. E. Brack, T. Michel, P. Mabey, S. Pikuz, J. C. Williams, M. Koenig, A. Casner, C. C. Kuranz, On the study of hydrodynamic instabilities in the presence of background magnetic fields in high-energy-density plasmas, Matter and Radiation at Extremes 6 (2021) 026904. doi:10.1063/5.0025374.

[9] C. Samulski, B. Srinivasan, M. J.-E. Manuel, R. Masti, J. P. Sauppe, J. Kline, Deceleration-stage Rayleigh-Taylor growth in a background magnetic field studied in cylindrical and cartesian geometries, Matter and Radiation at Extremes 7 (2022) 026902. doi:10.1063/5.0062168.

[10] T. Desjardins, C. Di Stefano, E. Merritt, K. Flippo, F. Doss, Reducing direct drive preheat with dopants, High Energy Density Physics 39 (2021) 100937. URL: https://www.sciencedirect.com/science/article/pii/S1574181821000148. doi:https://doi.org/10.1016/j.hedp.2021.100937.

[11] B. Yaakobi, I. Pelah, J. Hoose, Preheat by fast electrons in laser-fusion experiments, Phys. Rev. Lett. 37 (1976) 836–839. URL: https://link.aps.org/doi/10.1103/PhysRevLett.37.836. doi:10.1103/PhysRevLett.37.836.

[12] H. Shu, S. Fu, X. Huang, J. Wu, Z. Xie, F. Zhang, J. Ye, G. Jia, H. Zhou, Measuring preheat in laser-drive aluminum using velocity interferometer system for any reflector: Experiment, Physics of Plasmas 21 (2014) 082708. URL: https://doi.org/10.1063/1.4891429. doi:10.1063/1.4891429.

[13] C. Rousseaux, F. Amiranoff, C. Labaune, G. Matthieussent, Suprathermal and relativistic electrons produced in laser–plasma interaction at 0.26, 0.53, and 1.05 m laser wavelength, Physics of Fluids B: Plasma Physics 4 (1992) 2589–2595. URL: https://doi.org/10.1063/1.860174. doi:10.1063/1.860174.

[14] W. Priedhorsky, D. Lier, R. Day, D. Gerke, Hard-x-ray measurements of 10.6-μm laser-irradiated targets, Phys. Rev. Lett. 47 (1981) 1661–1664. URL: https://link.aps.org/doi/10.1103/PhysRevLett.47.1661. doi:10.1103/PhysRevLett.47.1661.

[15] C. A. Di Stefano, E. C. Merritt, F. W. Doss, K. A. Flippo, A. M. Rasmus, D. W. Schmidt, Evolution of surface structure in laser-preheated perturbed materials, Phys. Rev. E 95 (2017) 023202. URL: https://link.aps.org/doi/10.1103/PhysRevE.95.023202. doi:10.1103/PhysRevE.95.023202.

[16] A. R. Miles, D. G. Braun, M. J. Edwards, H. F. Robey, R. P. Drake, D. R. Leibrandt, Numerical simulation of supernova-relevant laser-driven hydro experiments on OMEGA, Physics of Plasmas 11 (2004) 3631–3645. URL: https://doi.org/10.1063/1.1753274. doi:10.1063/1.1753274.

[17] Y. Zhang, R. Paul Drake, J. Glimm, J. W. Grove, D. H. Sharp, Radiation-coupled front-tracking simulations for laser-driven shock experiments, Nonlinear Analysis: Theory, Methods Applications 63 (2005) e1635–e1644. URL: https://www.sciencedirect.com/science/article/pii/S0362546X05000726. doi:https://doi.org/10.1016/j.na.2005.01.056, invited Talks from the Fourth World Congress of Nonlinear Analysts (WCNA 2004).

[18] Y. Zhang, R. P. Drake, J. Glimm, Numerical evaluation of the impact of laser preheat on interface structure and instability, Physics of Plasmas 14 (2007) 062703. URL: https://doi.org/10.1063/1.2739453. doi:10.1063/1.2739453.

[19] R. E. Turner, K. Estabrook, R. L. Kauffman, D. R. Bach, R. P. Drake, D. W. Phillion, B. F. Lasinski, E. M. Campbell, W. L. Kruer, E. A. Williams, Evidence for collisional damping in high-energy raman-scattering experiments at 0.26 μm, Phys. Rev. Lett. 54 (1985) 189–192. URL: https://link.aps.org/doi/10.1103/PhysRevLett.54.189. doi:10.1103/PhysRevLett.54.189.

[20] J. R. Fein, J. P. Holloway, M. R. Trantham, P. A. Keiter, D. H. Edgell, D. H. Froula, D. Haberberger, Y. Frank, M. Fraenkel, E. Raicher, D. Shvarts, R. P. Drake, Mitigation of hot electrons from laser-plasma instabilities in high-Z, highly ionized plasmas, Physics of Plasmas 24 (2017) 032707. URL: https://doi.org/10.1063/1.4978625. doi:10.1063/1.4978625.

[21] B. Yaakobi, P.-Y. Chang, A. Solodov, C. Stoeckl, D. H. Edgell, R. S. Craxton, S. X. Hu, J. F. Myatt, F. J. Marshall, W. Seka, D. H. Froula, Fast-electron generation in long-scale-length plasmas, Physics of Plasmas 19 (2012) 012704. URL: https://doi.org/10.1063/1.3676153. doi:10.1063/1.3676153.

[22] E. Ott, Nonlinear evolution of the rayleigh-taylor instability of a thin layer, Phys. Rev. Lett. 29 (1972) 1429–1432. URL: https://link.aps.org/doi/10.1103/PhysRevLett.29.1429. doi:10.1103/PhysRevLett.29.1429.

[23] C. Samulski, B. Srinivasan, M. J.-E. Manuel, P. Nilson, J. Kline, An Experimental and Computational Study of Thin-Layer Rayleigh-Taylor Instability Development During Deceleration with and without an Externally Applied Magnetic Field, In preparation.

[24] B. E. Morgan, J. A. Greenough, Large-eddy and unsteady rans simulations of a shock-accelerated heavy gas cylinder, Shock Waves 26 (2016) 355–383. URL: https://doi.org/10.1007/s00193-015-0566-3. doi:10.1007/s00193-015-0566-3.

[25] H. Habara, T. Iwawaki, T. Gong, M. S. Wei, S. T. Ivancic, W. Theobald, C. M. Krauland, S. Zhang, G. Fiksel, K. A. Tanaka, A ten-inch manipulator (TIM) based fast-electron spectrometer with multiple viewing angles (OU-ESM), Review of Scientific Instruments 90 (2019) 063501. URL: https://doi.org/10.1063/1.5088529. doi:10.1063/1.5088529.

Chapter 5

Conclusions and Future Work

The disruptive nature of RTI in direct-drive ICF during deceleration results in a lower chance of reaching ignition and lower yield from fusion reactions. Understanding the seed mechanisms of RTI [1, 2, 3] and the use of an externally applied magnetic field to damp RTI growth [4, 5] during deceleration is the primary focus of this work. Beginning with a design study of various experimental platforms, such as Omega, Omega-EP and NIF, in Chapter 2, the viability of experimentally studying deceleration stage RTI with and without an externally applied magnetic field was explored. From this initial design study two experimental platforms are conceived, one built for NIF and the other for Omega-EP. The extensive and iterative design process of novel platform development and the experimental results are presented in Chapter 3. The novel development of a thin-layer RTI platform for Omega-EP and initial results show a need to shift from 2D modeling in design work to high-fidelity 3D modeling. Additionally, the experimental results for the NIF platform, as well as an exploration of unexpected preheating of targets from high-intensity-laser generated hot-electrons is discussed in Chapter 4.

Magnetic fields have been shown to damp RTI growth [5, 6], so the application of an externally applied magnetic field to an RTI unstable surface during deceleration could potentially damp the disruptive RTI evolution. The pursuit of a viable deceleration-stage RTI experimental platform is the motivation for the design scan shown in Chapter 2. Beginning with an exploration of cylindrical platforms [7] on Omega and a planar configuration on Omega-EP, the presented work shows that the plasma condition in which a magnetic field would have a measurable damping impact on the RTI are not reached. Shifting to NIF for a high laser drive, cylindrical targets are found to converge too quickly, but a planar target with a sinusoidal perturbation does reach necessary plasma conditions, R_m of approximately 50, for a measurable difference in RTI spike size with and without a magnetic field [8, 9]. A comparable experimental platform on NIF is fielded and the results are presented in Chapter 4. The NIF experiments yielded image results that shows no visible RTI growth regardless of the presence of an externally applied magnetic field, thus some physics effect must not have been accounted for in the planning and design stage. A notable area of future research interest is the differing interface velocities in the NIF experimental results, where the magnetized experiment's interface is moving at a significantly slower velocity when compared to the unmagnetized experimental results and the simulation data shown in Chapter 4. The NIF experimental platform is reevaluated to determine the potential cause of the RTI loss, and high-intensity-laser generated hot-electron induced preheat [10] is identified as the primary possible source.

An experimental platform for Omega-EP is designed in Chapter 3 to be comparable to the NIF configuration, though using only a divot as the seed perturbation of the RTI. The Omega-EP experiment successfully captured the presence of two hot-electron populations, one from the backlighter drive at 60 keV and a second larger population at 200 keV from the laser drive. The presence of these hot-electron populations requires the exploration of potential target preheating, and it is found that on the Omega-EP platform, while the level of preheating impacts the RTI morphology, there is still measurable RTI growth. However,

when using the Omega-EP hot-electron population to estimate the preheating of the NIF targets, the RTI growth and morphology is impacted. In low preheat cases additional mode growth is present, and at high preheat temperatures RTI growth is significantly damped to such a degree that the preheating during the experiment could have caused RTI growth to be undetectable by the NIF imaging diagnostics which has a 50 µm resolution.

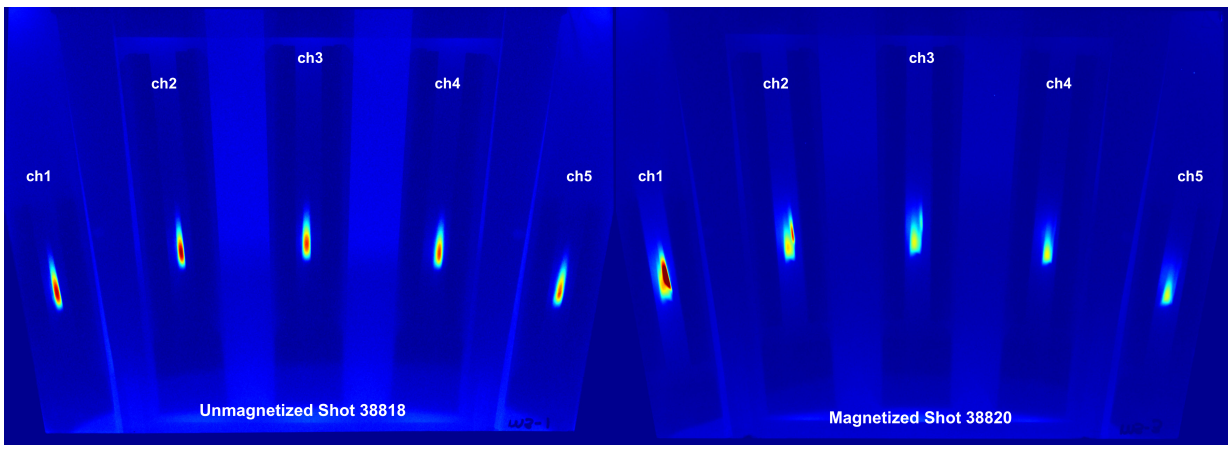

Figure 5.1: Raw OUESM data from an unmagnetized shot, 38818, on the left and the magnetized shot, 38820, on the right. Channels 1 and 2 in the mangetized data show a larger saturated signal than in the unmagnetized shot's respective channels.

An additional finding from the hot-electron data is observation of impact of the presence of a background magnetic field on the hot-electron populations. Specifically, as can be seen in figure 5.1 the raw data from the OUESM diagnostic shows an oversaturation in the first two channels whereas in the unmagnetized case where the hot-electron distribution is symmetric across the channels. When this magnetized data is analyzed, the skew of hot-electrons detected in channels 1 and 2 is further noticeable, as seen in figure 5.2. The OUESM diagnostic was not calibrated for use with an applied magnetic field, thus determining the source of the skewing phenomena is difficult but does open an additional area of future research interest.

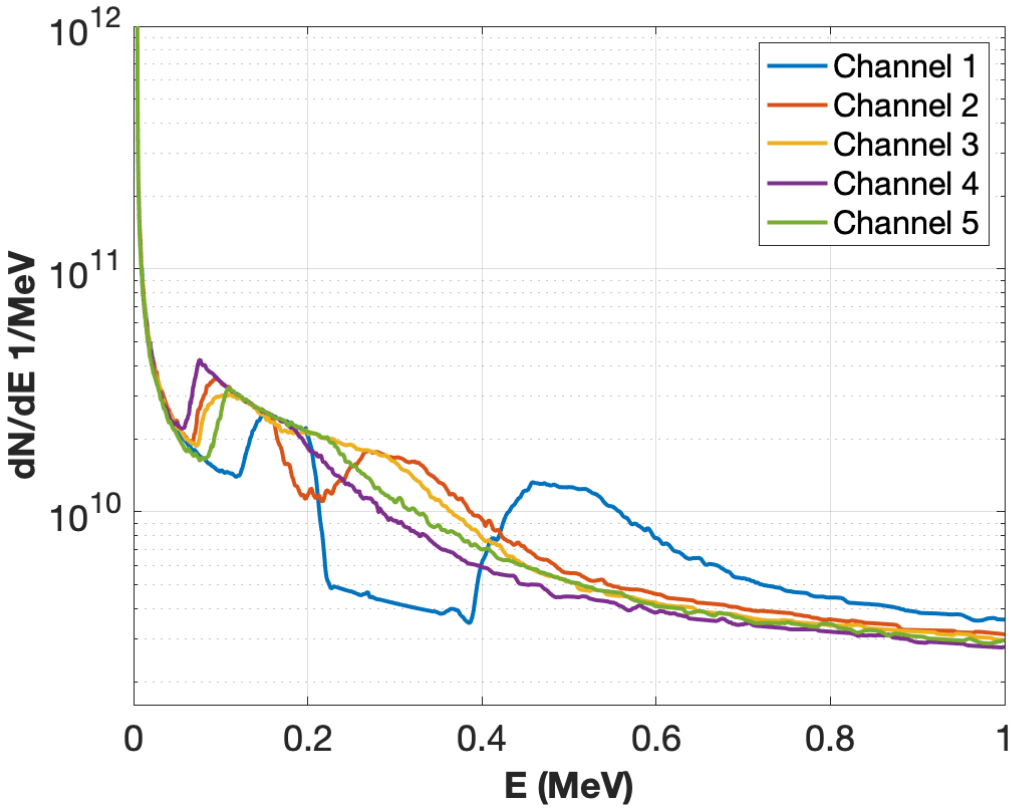

Figure 5.2: The accelerated hot-electrons spectrum energy for the single magnetized shot, 38820, across all five channels of the OUESM detector. As can be seen when compared to the hot-electron spectrum plots in Chapter 4, there is a skew towards higher energies, greater than 200 keV, in the hot-electron populations detected in channels 1 and 2.

In addition to hot-electron data, the iterative process of target design and redesign after initial experimental results is shown in detail in Section 3.1. The results of the final experimental day are detailed in the manuscript presented in Section 3.2, showing the impact of manufacturing defects on the RTI morphology and the required defect tolerances for the target design. Given the target is initially designed using 2D modeling, an exploration of 3D modeling is needed to benchmark the data and better capture the complexity of the target design [11]. Ultimately, the need for 3D modeling in the target design stage is demonstrated for high-fidelity predictive modeling and more accurate target design for future experimental iterations.

The overarching conclusion from this work is one of continued improvement, improving computational modeling, improving experimental platforms, and the ever iterative nature of science. The foundation of both the presented novel experimental platforms allows future iterations of similar experimental targets to be developed and possibly fielded. Continued improvement of the target designs, particularly utilizing 3D modeling, will allow for future

experiments to gather more imaging data to validate the resistivity models provided in EOS tables. Additionally the potential impact of hot-electron induced preheating can be further explored with kinetic simulations that focus on electron preheat physics, a series of experiments designed specially to study the preheat effects on materials, and further experimental studies on the potential material choices used to mitigate preheat [12, 13].

Bibliography

[1] E. Ott, Nonlinear Evolution of the Rayleigh-Taylor Instability of a Thin Layer., Physical Review Letters 29 (1972) 1429–1432.

[2] C. Weber, et al., Mixing in ICF implosions on the Nation Ignition Facility caused by the fill-tube, Physics of Plasmas 27 (2020) 032703.

[3] D. Clark, et al., Radiation hydrodynamics modeling of the highest compression inertial confinement fusion ignition experiment from the Nation Ignition Campaign., Physics of Plasmas 22 (2015) 022703.

[4] L. Perkins, D.-M. Ho, B. Logan, G. Zimmerman, M. Rhodes, D. Strozzi, D. Blackfield, S. Hawkins, The potential of imposed magnetic fields for enhancing ignition probability and fusion energy yield in indirect-drive inertial confinement fusion, Physics of Plasmas 24 (2017) 062708.

[5] B. Srinivasan, X.-Z. Tang, The mitigating effect of magnetic fields on Rayleigh-Taylor unstable inertial confinement fusion plasmas, Physics of Plasmas 20 (2013) 056307.

[6] B. Srinivasan, X.-Z. Tang, On the study of hydrodynamic instabilities in the presence of background magnetic fields in high-energy-density plasmas, EPL (Europhysics Letters) 107 (2014) 65001.

[7] J. P. Sauppe, S. Palaniyappan, E. N. Loomis, J. L. Kline, K. A. Flippo, B. Srinivasan, Using cylindrical implosions to investigate hydrodynamic instabilities in convergent geometry, Matter and Radiation at Extremes 4 (2019) 065403. URL: https://doi.org/10.1063/1.5090999. doi:10.1063/1.5090999. arXiv:https://doi.org/10.1063/1.5090999.

[8] C. Samulski, B. Srinivasan, M. J.-E. Manuel, R. Masti, J. P. Sauppe, J. Kline, Deceleration-stage Rayleigh-Taylor growth in a background magnetic field studied in cylindrical and Cartesian geometries, Matter and Radiation at Extremes 7 (2022) 026902. doi:10.1063/5.0062168.

[9] C. Samulski, Deceleration Stage Rayleigh-Taylor Instability Growth in Inertial Confinement Fusion Relevant Configurations, Master's thesis, 2021.

[10] C. Samulski, M. J.-E. Manuel, B. Srinivasan, K. Raman, J. Kline, Preheat effects in laser-driven shock-tube experiments at intensities greater than $10 \times 10^{15}\,\mathrm{W/cm^2}$ at Omega-EP and the NIF, In preparation.

[11] C. Samulski, B. Srinivasan, M. J.-E. Manuel, P. Nilson, J. Kline, An Experimental and Computational Study of Thin-Layer Rayleigh-Taylor Instability Development During Deceleration with and without an Externally Applied Magnetic Field, In preparation.

[12] T. Desjardins, C. Di Stefano, E. Merritt, K. Flippo, F. Doss, Reducing direct drive preheat with dopants, High Energy Density Physics 39 (2021) 100937. URL: https://www.sciencedirect.com/science/article/pii/S1574181821000148. doi:https://doi.org/10.1016/j.hedp.2021.100937.

[13] J. R. Fein, J. P. Holloway, M. R. Trantham, P. A. Keiter, D. H. Edgell, D. H. Froula, D. Haberberger, Y. Frank, M. Fraenkel, E. Raicher, D. Shvarts, R. P. Drake, Mitigation of hot electrons from laser-plasma instabilities in high-Z, highly ionized plasmas, Physics of Plasmas 24 (2017) 032707. URL: https://doi.org/10.1063/1.4978625. doi:10.1063/1.4978625.

Appendices

Appendix A

Synthetic x-ray radiograph generator for FLASH

Synthetic x-ray radiographs are used to predict what experimental x-ray radiograph results will look like from simulation data. The process of generating a synthetic radiograph consist of pulling the material density from simulation data at a desired time. The density data is then used in the alternate form of the Beer-Lambert law to find the intensity transmitted through the experimental target,

$$I = I_0 e^{-(\mu/\rho_m)\lambda}. \tag{A.1}$$

Where I is intensity, I_0 is the intensity at the backlighter origin, μ is the linear attenuation coefficient, ρ_m is the mass, and λ is the areal density , $\lambda = \rho_m l$, with l being the optical depth. A MATLAB code for the generation of a synthetic x-ray radiograph from a FLASH hdf5 file can be found below.

```
%%%
```

```
    for i = 1: 4
        x(4*(j-1)+i) = coord(1,j) - blksize(1,j)/2 + i*blksize(1,
           j)/4 - blksize(1,j)/8;
        y(4*(j-1)+i) = coord(2,j) - blksize(2,j)/2 + i*blksize(2,
           j)/4 - blksize(2,j)/8;
    end
end

%% convert vector x and y to matrixes X and Y
X= zeros(4);
Y= zeros(4);
for j = 1:size(blksize,2)
    for i = 1:4
        X(i,4*(j-1)+1:4*j) = x(4*(j-1)+i);
        Y(:,4*(j-1)+i) = y(4*(j-1)+i);
    end
end

%% generate interpolation grid and generate xmin xmax ymin ymax
   for plot

xresolution=min(min(abs(-X(1:end-1,:)+X(2:end,:))));
% finest mash size in simulation x

yresolution=min(min(abs(-Y(:,1:end-1)+Y(:,2:end))));
% finest mash size in simulation y

xmin = min(coord(1,:) - blksize(1,:)/2);
xmax = max(coord(1,:) + blksize(1,:)/2);
ymin = min(coord(2,:) - blksize(2,:)/2);
ymax = max(coord(2,:) + blksize(2,:)/2);
% Boundary position, not the center

xq = (xmin+xresolution/2:xresolution:xmax-xresolution/2);
yq = (ymin+yresolution/2:yresolution:ymax-yresolution/2);
yq = yq';

%% assign density map

A=zeros(4,4*size(blksize,2));
% size(blksize,2) is the total block number

```

```
varname1 = 'foam';
varname2 = 'ablt';
varname3 = 'vacu';
varname4 = 'pert';
varname5 = 'push';
% material names from FLASH

foam = hdf5read(filename1,varname1);
foam = double(foam);
ablt = hdf5read(filename1,varname2);
ablt = double(ablt);
vacu = hdf5read(filename1,varname3);
vacu = double(vacu);
pert = hdf5read(filename1,varname4);
pert = double(pert);
push = hdf5read(filename1,varname5);
push = double(push);

for j = 1:size(blksize,2)
    for i = 1:4
        A1(:,4*(j-1)+1:4*j) = foam(:,:,1,j);
    end
end

for j = 1:size(blksize,2)
    for i = 1:4
        A2(:,4*(j-1)+1:4*j) = ablt(:,:,1,j);
    end
end

for j = 1:size(blksize,2)
    for i = 1:4
        A3(:,4*(j-1)+1:4*j) = vacu(:,:,1,j);
    end
end

for j = 1:size(blksize,2)
    for i = 1:4
        A4(:,4*(j-1)+1:4*j) = pert(:,:,1,j);
    end
end

```

```
for j = 1:size(blksize,2)
    for i = 1:4
        A5(:,4*(j-1)+1:4*j) = push(:,:,1,j);
    end
end

FOAM = griddata(X,Y,A1,xq,yq,'nearest');
ABLT = griddata(X,Y,A2,xq,yq,'nearest');
VACU = griddata(X,Y,A3,xq,yq,'nearest');
PERT = griddata(X,Y,A4,xq,yq,'nearest');
PUSH = griddata(X,Y,A5,xq,yq,'nearest');

%% Beer-Lambert law calculation for transmission

muvacu = 0.0000038734;
% linear attenuation coefficient for vacu material at backlight energy

muablt = 3.143191;
% linear attenuation coefficient for ablt material at backlight energy

mufoam = 1.508732;
% linear attenuation coefficient for foam material at backlight energy

mupert = 107.7236;
% linear attenuation coefficient for pert material at backlight energy

mupush = 107.7236;
% linear attenuation coefficient for push material at backlight energy

depth = 0.02;
% optical depth in cm

ima  = (VACU./muvacu)+(ABLT./muablt)+(FOAM./mufoam)+(PERT./mupert)+(PUSH./mupush);
% inverse mass attenuation coefficient

ma = 1./ima;
```

```
% mass attenuation coefficient mu/rho

lambda = (VACU.*depth)+(ABLT.*depth)+(FOAM.*depth)+(PERT.*depth)
   +(PUSH.*depth);
% areal density rho*optical depth

Trans = exp(-(ma).*lambda);
% Beer-Lambert law

%% artifical blurring

Gauss1 = imgaussfilt(Trans, 1, 'FilterSize', [3 3]);
Gauss2 = imgaussfilt(Gauss1, 7, 'FilterSize', [1 9]);

%% plot radiograph

figure;
imagesc([min(xq) max(xq)],[min(yq) max(yq)],Gauss2);
set(gca,'Ydir','normal')
colormap(gray);
colorbar;
xlabel('x [cm]');
ylabel('y [cm]');
axis image
```